Design and Construction of a Radiation Source of Extreme Flux

Author:
Francisco Valle Brozas

Directors:
Luis Roso Franco
Álvaro Peralta Conde

Contents

List of Figures

List of Tables

Agradecimientos

Podría poner una ristra enorme de nombres mencionando a todas aquellas personas que hicieron posible que esta tesis saliera adelante. Pero creo que cualquiera que me haya ayudado a hacer este trabajo, sabe que cuenta con mi gratitud.

No obstante, sí hay algunos nombres que me gustaría destacar. Quiero mencionar especialmente a aquellos que no sólo trabajaron junto a mí, si no que además confiaron en mí para que les dirigiera. Gracias a Aurora, por ese talento artístico que nos permitió hacernos con unas pinturas. A Carlos, por aguantarnos y aún así decidir quedarse aquí. A Jose, por no romperme nada en el laboratorio. A Adrián, que aguantó estoicamente las horas en el museo. Y a Jesús y Martín, por ese viaje a Madrid en el que hicimos algo bueno.

Gracias Alicia, por enseñarme algo más que física.

Y gracias a mis directores de tesis, que han hecho que este trabajo sea el que es.

Introduction

The present thesis consists of the design and construction of an X-ray source through the interaction of an ultra-intense laser with a solid and/or liquid target. Specifically, the laser technology suitable for this purpose has been investigated, the characteristics of the laser-matter interaction have been studied and possible applications of the generated X-radiation (and accelerated electrons) have been explored.

Nowadays, the development of sources of ionizing radiation through laser-matter interaction has allowed access to pulsed X-ray beams with ultra-short duration -the radiation produced "inherits" the characteristics of the laser that generates it- and extreme instantaneous fluxes. This implies the possibility of studying the interaction of X-rays with matter in regimes impossible to reach by conventional sources. While a laser-generated X-ray pulse lasts for hundreds of femtoseconds or a few picoseconds, a conventional X-ray tube produces pulses at the microsecond regime. Likewise, the instantaneous fluxes reached maximize the possible non-linear effects, that is, a series of effects that happen when a great concentration of photons results in two or more photons interacting simultaneously with the matter.

If we focus on the production of X-rays by laser, we can now find relatively simple assemblies capable of producing X-ray pulses using moderate laser intensities (in the range of $10^{16} - 10^{17}\mathrm{W/cm^2}$). In this approach, typically a femtosecond laser is focused on a solid target producing in the first instants the ionization of the sample. When the main part of the pulse arrives, the laser interacts with an expanding plasma rather than with the solid target itself. In this interaction, the electrons are extracted from the plasma by the electric field of the laser, accelerated and reinjected into it. In this process, it is produced both Bremsstrahlung radiation, by the sudden loss of energy of the reinjected electrons, as well as characteristic X-rays of the material of the target, by the creation of vacancies in the inner layers of the atoms of the material that are quickly occupied by electrons from upper layers. The X-rays thus produced inherently have the temporal characteristics of the laser pulse. The theory behind the production of laser X-rays, as well as the acceleration of particles with this technology, is presented in Chapter 1.

Although the setup for obtaining a source of laser driven ultrashort X-rays pulses is relatively simple, it is not without drawbacks. If a solid target is used, it is necessary to

move the target so that the next laser pulse finds a clean area of the material and the radiation production can be efficient. This limits the reproducibility of X-ray production because the same conditions must be ensured in the movement of the target. Likewise, the area of unused material is limited, and eventually the target must be replaced. Thus, one of the requirements for future developments from the point of view of laser technology is to have sources of ionizing radiation with greater control of radiation characteristics, more user-friendly sources and sufficiently robust to allow systematic measurements [1, 2].

One of the fields with promising applications is in radiotherapy. At the moment, the scientific community tries to answer questions such as "Can we in fact trigger non-linear phenomena with these instantaneous flows? Is there any advantage in depositing the entire dose in an ultra short period of time? Can we deepen our knowledge of the tissue irradiation dynamics and thus design more efficient radiotherapy treatments? (See for example, references [3–5]). In this regard, at this time only a few preliminary studies can be found using ultrashort ionizing radiation generated by laser in different cell lines (mostly in vitro). Unfortunately, the results are inconclusive, and further research is needed [6–14].

Thus, and taking into account the context presented, this thesis aims, on the one hand, to develop a laser driven X-ray source of extreme flux that allows future studies on non-linear damage. And on the other hand, to explore possible improvements to this type of source that allow greater stability, make them more profitable and easier handling than currently available. In this sense, the use of a liquid jet for the production of X-rays has been analysed in order to solve the drawbacks of solid targets. This type of targets allows to maintain a profile of stable density shot to shot and consequently a reproducible X-ray production. The results of these experiments will be presented in Chapter 2. Also, in order to characterize the source, the chapter 3 presents a time-of-flight detector for ions that may be used in the future to study the temporal duration of the X-ray pulse.

After the development of the X-ray source, its possible applications have been studied. In particular, it has been analysed how it can be used to perform X-ray fluorescence experiments. These results, as well as other possible applications, will be presented in Chapter 4.

Finally, in order to obtain a source of radiation that is not only robust and stable, but also economically profitable, the Chapter 5 will analyse possible changes to the laser itself that will reduce the production of the source.

Chapter 1

Theoretical Introduction

1.1 Ultraintense Lasers

The fast development of laser technology from its birth, –the first laser was fired by T. H. Maiman Malibu, California laboratories in 1960 - providing systems with a growing energy per pulse, shorter pulses, and extremely robust with respect to the experimental parameters, has paved the way to new and unexpected applications in several scientific disciplines.

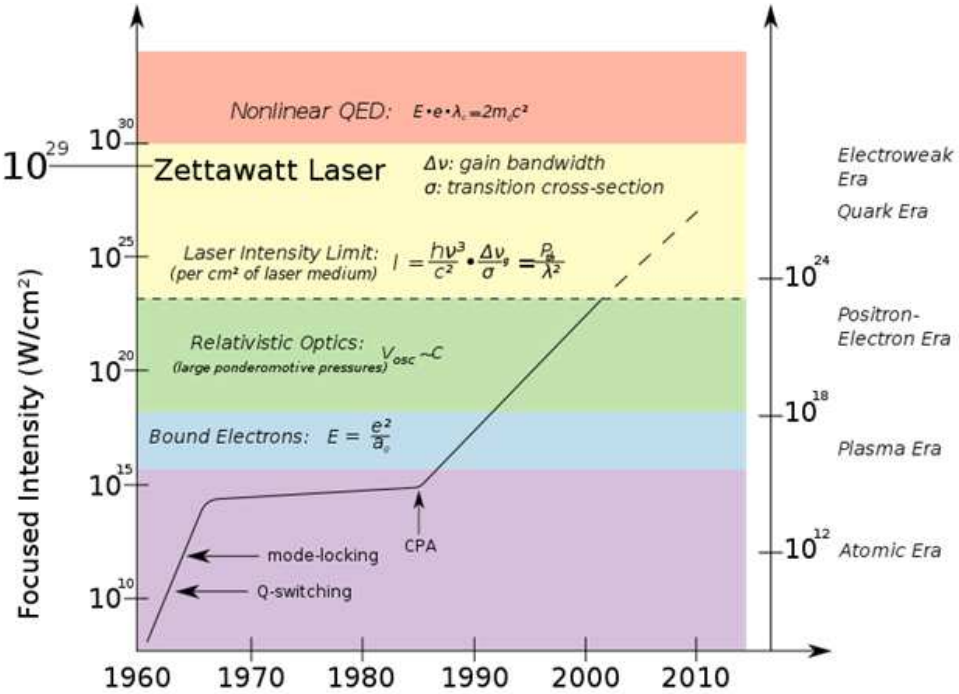

Figure 1.1: Graph showing the history of maximum laser pulse intensity throughout the past 50 years. The highest intensity achieved so far is 10^{22} W/cm^2 produced by the petawatt laser HERCULES at the University of Michigan, USA, in 2007.

One of the fields of Science that has been clearly reinforced by this progress is laser-based particle acceleration, specially from the invention in the mid 1980s of the chirped pulse amplification (CPA) technique by Gérard Mourou and Donna Strickland at the University of Rochester (USA) [15]. Before the development of CPA technique, although theoretically it was possible to produce ultraintense ultrashort laser pulses, in practice the maximum intensity achievable was limited to hundreds of gigawatts per square centimetre due to the damage threshold of the gain medium and optical elements (see Fig. 1.1). Using CPA, however, there is no such limitation because the laser pulse is temporally stretched -reducing hence its peak power- prior the amplification. Once it is fully amplified, the laser is temporally compressed back recovering the original ultrashort pulse duration, and achieving peak powers in the terawatt and pettawat level [1, 2, 16]. With such tremendous powers, nowadays it is possible to implement compact particle accelerators and hence sources of ionizing radiation for biological and medical research based on laser-matter interaction.

In simple terms, the acceleration of particles is accomplished by focusing an ultraintense laser pulse with duration of the order of the central wavelength λ, i.e., pulses that contain a limited number of optical cycles, in a spot of the order of λ^2. In such conditions, the laser energy is concentrated in a spatial cube of the order of λ^3 being possible to get intensities up to $10^{17}\,\mathrm{W/cm^2}$ with moderate laser powers (GW). For intensities of the order of $10^{16}\,\mathrm{W/cm^2}$, the electric field of the laser is higher than the electric field that the electrons feel from the nucleus, producing the ionization of the atom. The expelled electrons are further accelerated by the laser and re-injected into the bulk material once the electric field reverses its direction. In this process, deep ultraviolet (VUV), extreme ultraviolet (XUV), and X-ray radiation are generated (see for example [16–20] and references therein). For intensities of $10^{18}\,\mathrm{W/cm^2}$, not only electrons are accelerated but also protons. Besides, this accelerated ions can be used to produce high energetic neutrons [1, 2, 16].

In the following sections we will deepen in the CPA mechanism, the ionization by ultraintense laser and the acceleration of particles by laser.

1.2 Chirped Pulsed Amplification (CPA)

As it was mentioned above, using CPA is possible to amplify laser pulses without damaging the optical components, specially the active mediums. CPA is composed of three main elements:

- A **stretcher** that increases the pulse duration.
- One or several **amplifiers** that increase the pulse energy.
- A **compressor** that reduces the pulse duration.

In the following sections we will review these elements in detail.

1.2.1 Stretching

The role of the stretcher is to increase the pulse duration reducing accordingly the peak power. After passing through the stretcher, the pulse acquires a spectral phase $\phi(\omega)$ defined by:

$$E(t) = \frac{1}{2\pi}\int_{-\infty}^{\infty} E(\omega)e^{\phi(\omega)}e^{(-i\omega t)}d\omega \tag{1.1}$$

The spectral phase can be written as:

$$\phi(\omega) = \phi(\omega_0) + \frac{\partial\phi(\omega_0)}{\partial\omega}(\omega-\omega_0) + \frac{1}{2}\frac{\partial^2\phi(\omega_0)}{\partial\omega^2}(\omega-\omega_0)^2 + \frac{1}{6}\frac{\partial^3\phi}{\partial\omega^3}(\omega-\omega_0)^3 + ... \tag{1.2}$$

The first term $\frac{\partial\phi(\omega_0)}{\partial\omega}(\omega-\omega_0)$ implies a temporal shift of the pulse, which corresponds to the time that the pulse spends going across the stretcher. The second order term is defined as the Group Delay Dispersion (GDD):

$$\text{GDD} = \frac{\partial^2\phi(\omega_0)}{\partial\omega^2} \tag{1.3}$$

This term, which is quadratic with the frequency, induces a broadening in the temporal duration of the pulse, which is what is desired in a stretcher. If we consider an originally unchirped Gaussian pulse with duration τ_0

$$E(t) = E_0\exp\left(-2\ln 2\frac{t^2}{\tau_0^2}\right) \tag{1.4}$$

and we add a GDD, we have in the frequency domain:

$$E(\omega) = E_0\exp\left(\tau_0\frac{(\omega-\omega_0)^2}{8\ln 2}\right)\exp\left(-i\frac{1}{2}GDD(\omega-\omega_0)^2\right) \tag{1.5}$$

Back in the time domain we have:

$$E(t) = E_0\exp\left(-2\ln 2\frac{\tau_0^2t^2}{16\ln^2\text{GDD}^2+\tau_0^4}\right)\exp\left(i\left(\omega_0t+\frac{2\text{GDDt}^2}{4\text{GDD}^2+\left(\frac{\tau_0^4}{4\ln^2 2}\right)}\right)\right) \tag{1.6}$$

The duration is increased as [21]:

$$\tau = \tau_0\sqrt{1+\left(4\ln(2)\left(\frac{\text{GDD}}{\tau_0^2}\right)\right)^2} \tag{1.7}$$

while the instant frequency is:

$$\omega(t) = \omega_0 + \frac{2\text{GDD}}{4\text{GDD}^2 + \left(\frac{\tau_0^4}{4\ln^2 2}\right)}t \tag{1.8}$$

This means that for a positive GDD the highest frequencies are at the end of the pulse, while for a negative GDD the highest frequencies are in the front of the pulse.

The third order dispersion (TOD), defined as

$$\text{TOD} = \frac{\partial^3\phi(\omega_0)}{\partial\omega^3} \tag{1.9}$$

introduces ripples preceding or following the main pulse. Successive delay dispersion orders induce also other deformations in the pulse that must be avoided.

The GDD introduced by the stretcher must be compensated by the compressor. The stretcher can introduce a positive or a negative GDD, since according to Eq. 1.7 the effect in the pulse duration is the same. Usually a positive dispersion is chosen. The reason is because the amplifiers introduce also positive GDD when the pulse goes through the material of the active mediums and the rest of optical elements. Thus, the risk of reducing the GDD in the amplifier, which would increase the peak power of the pulse and damage the amplifier medidum, is avoided. Finally, the compressor compensates all the accumulated GDD both in the stretcher and the amplifiers.

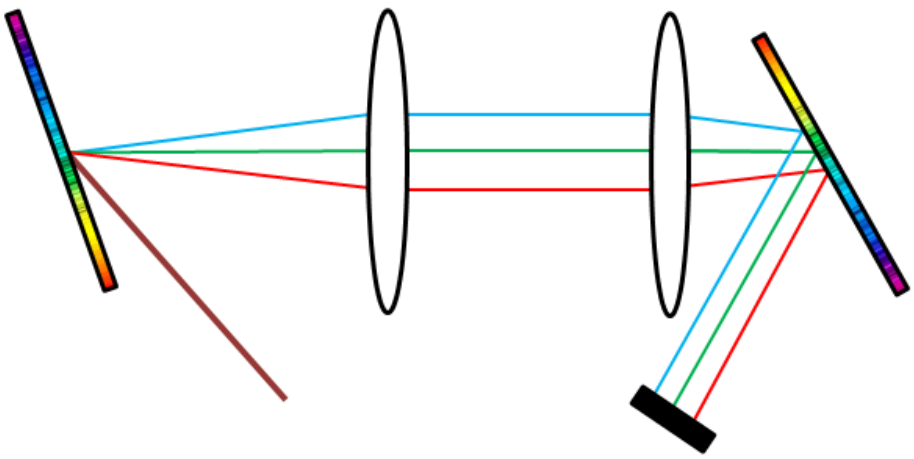

Figure 1.2: Laser stretcher composed of two diffraction gratings, two lenses and a reflector.

Typically the stretcher consists in two diffraction grating in a configuration like the one shown in figure 1.2. The path travelled here by the higher frequencies is longer than the path travelled by the lower ones. Thus, a positive GDD, where the lower frequencies are in the front of the pulse, is introduced by this stretcher. There are many other configurations or setups that can be used to stretch the pulse.

1.2.2 Amplification

After stretching, the peak power of the pulse is reduced and the laser can be safely amplified without damaging the optical elements, i.e., the laser power is below the damage threshold of the materials. In the amplifier, the laser goes through an active medium that has been previously pumped to achieve population inversion so the pulse is amplified by stimulated emission of radiation. The repetition rate of the pulse in the amplifiers is limited by the repetition rate of the pump system and the cooling of the gain medium. Heat dissipation is the main problem when designing amplifiers.

After some passes through the active medium, the pulse drains all the available energy. This is the so called *gain saturation regime*. It is desirable to work with amplifiers near the gain saturation regime because it gives stability to the output. Two kind of amplifiers are used: regenerative amplifiers and multipass amplifiers.

Regenerative amplifier

A regenerative amplifier acts like a laser cavity where the pulse is locked, being amplified in each pass through the active medium. These amplifiers are typically used in the first steps of amplification. As the laser has low energy in these steps, several passes through the medium are required to drain all the available energy stored in the active medium, so a resonator configuration is the appropriated option. Once the pulse has saturated the medium, it is coupled out. The high losses of the common switches that coupled out the pulse limits the maximum energy that a pulse can gain in a regenerative amplifier. For example, Pockels cells are commonly used to control the exit of the pulse (see Fig. 1.3). The cell changes the polarization of the beam and the pulse is reflected in a Brewster angle. These elements have big losses, so if the medium is working near saturation, more passes in the resonator will decrease the pulse energy instead of being amplified. On the other hand, Pockels cells can induce high order dispersion, which is hard to compensate. Despite of these limitations, laser pulses can be amplified even more with multipass amplifiers.

Multipass amplifier

After draining all the energy that the pulse can gain in a regenerative amplifier, the laser can be further amplified by passing through several active mediums. Since the pulse has been pre-amplified, the gain of each pass is higher and saturation of the active medium occurs within few passes. The typical configuration is a bow-tie path (see Fig. 1.4).

- Frantz-Nodvik model

Laser amplification process is typically described by the Frantz-Nodvik model [22]. This model works under the approximation that the pulse is sufficiently short in time so any upper

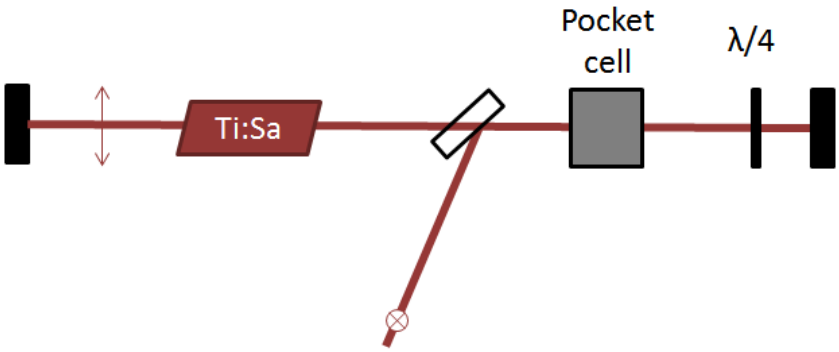

Figure 1.3: Typical regenerative amplifier for a Ti:Sapphire laser. A Pockels cell controls the exit of the pulse. When the pulse has extracted all the available energy from the active medium, the Pockels cell changes the polarization of the laser and the pulse is reflected out of the cavity.

relaxation mechanism can be neglected during the transit. For a steady state situation, we can describe the population dynamics using rate equations.

The intensity of the laser pulse $I(z,t)$ can be written as a plane wave with a source term that depends on the stimulated emission:

$$\frac{\partial I}{\partial z} + \frac{1}{c}\frac{\partial I}{\partial t} = \sigma N I \tag{1.10}$$

where $N = N_2 - N_1$ is the population difference between the two level of the laser transition and σ is the differential section of the atoms of the active medium. The model assumes population inversion, so $N > 0$.

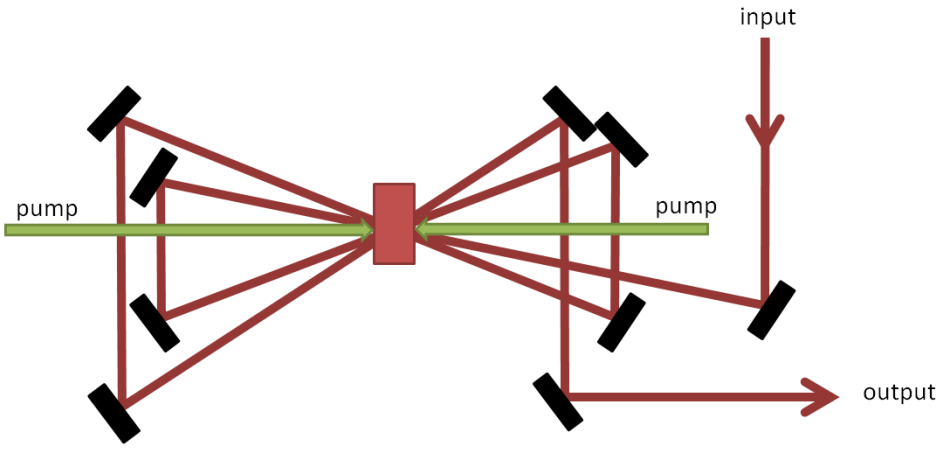

Figure 1.4: Multipass amplifier in a bow-tie configuration.

We can express equation 1.10 as a function of the pulse fluence ϕ, defined as:

$$\phi(z) = \int_{-\infty}^{\infty} I(z,t)dt \tag{1.11}$$

$$\frac{\partial \phi(z)}{\partial z} = \sigma \int_{-\infty}^{\infty} N(z,t)I(z,t)dt \tag{1.12}$$

Under the approximations of the model, the population inversion can be described by the following rate equation:

$$\frac{\partial N(z,t)}{\partial t} = -\frac{2\sigma}{h\nu}N(z,t)I \tag{1.13}$$

which means that $N(z,t)$ can be expressed as a function of $I(z,t)$:

$$N(z,t) = N(z,-\infty)\exp\left(-\frac{2\sigma}{h\nu}\int_{-\infty}^{t} I(z,t')dt'\right) \tag{1.14}$$

After the pulse has left the medium, the population difference reads

$$N(z,\infty) = N(z,-\infty)\exp\left(-\frac{\phi(z)}{\phi_{sat}}\right) \tag{1.15}$$

where

$$\phi_{sat} \equiv \frac{h\nu}{2\sigma} \tag{1.16}$$

Equation 1.13 can be solved using Eq. 1.14 if the signal gain coefficient $g_0 = \sigma N$ is considered constant over the length of the amplifier. This is a good approximation for an amplifying material that is uniformly pumped. In that case, the output fluence after a single pass is:

$$\phi_{out} = \phi_{sat}\ln\left[1 + G_0\left(\exp(\phi_{in}/\phi_{sat}) - 1\right]\right. \tag{1.17}$$

This equation can be generalise for n number of passes:

$$\phi_{out,n} = \phi_{sat}\ln\left[1 + G_0\left(\exp(\phi_{in,n}/\phi_{sat}) - 1\right]\right. \tag{1.18}$$

It must be taken into account that the input fluence of the pass number n will be lower than the output number $n-1$ due to the losses in the round trip in the amplifier. This is expressed by a loss factor $\Gamma < 1$:

$$\phi_{in,n+1} = \Gamma\phi_{out,n} \tag{1.19}$$

The gain after a certain pass number G_n can be expressed as a function of the stored fluence ϕ_{sto} in the amplifier, which is defined as:

$$\phi_{sto} \equiv \frac{Nh\nu}{2}L \tag{1.20}$$

where L is the length of the amplifier medium. The stored fluence represents the largest fluence that can be extracted from the amplifier, which is found by taking the limit $\phi_{in}/\phi_{out} >> 1$:

$$\phi_{out} \approx \phi_{in} + (g_0\phi_{sat})L = \phi_{in} + \frac{Nh\nu}{2}L = \phi_{in} + \phi_{sto} \tag{1.21}$$

After a pass, the stored fluence is lowered by the amount extracted by the pulse:

$$\phi_{sto,n+1} = \phi_{sto,n} - (\phi_{out,n} - \phi_{in,n}) \tag{1.22}$$

So the gain G_n for a certain pass number n will be:

$$G_n = \exp(g_n L) = \exp\left(\frac{\phi_{sto,n}}{\phi_{sat}}\right) \tag{1.23}$$

To compute the stored fluence in the amplifier, one must take first into account the fluence that is absorbed in the amplifier:

$$\phi_{abs} = \phi_{pump}\,(1 - \exp(-\alpha L)) \tag{1.24}$$

where ϕ_{pump} is the pump fluence and α is the absorption coefficient in the active medium. Also, one must take into account the quantum defect (factor $\frac{\lambda_p}{\lambda_s}$ where λ_p is the wavelength of the pump and λ_s the laser wavelength) and the thermal losses (factor η):

$$\phi_{sto} = \phi_{abs}\eta\frac{\lambda_p}{\lambda_s} \tag{1.25}$$

As we can see, the amplification is a non-linear process. This leads to two effects. On one hand, it produces *gain narrowing*: the central frequencies of the pulse are more amplified than the spectral wings. On the other hand, the intense parts of the beam profile saturates the amplifier more than the rest, so after several steps of amplification the laser presents a top-hat intensity distribution.

1.2.3 Compression

After being amplified, the pulse must recover its initial temporal duration. For that, the Group Delay Dispersion (GDD) introduced by the stretcher and the multiple passes through the active mediums must be compensated. As the GDD introduced by the active medium, and typically also by the stretcher, is positive, the compressor must introduced a negative GDD. Usually, two diffraction grating are used for this purpose (see Fig. 1.5). The phase that each frequency acquires in a compressor with this configuration can be written as:

$$\phi(\omega) = 2\left(\frac{\omega}{c}z(\omega) - \frac{2\pi}{L_g}d \cdot \tan(\theta(\omega))\right) \tag{1.26}$$

where $z(\omega)$ is the distance that the frequency ω goes through the compressor, $\theta(\omega)$ is the diffraction angle for the frequency ω, d is the distance between fringes in the grating and L_g is the distance between the two gratings. The GDD that the compressor introduces is in consequence:

$$\frac{d^2\phi(\omega)}{d\omega^2} = \frac{\lambda^3 L_g}{\pi c^2 d^2}\left[1 - \left(\frac{\lambda}{d} - \sin(\theta_{in})\right)^2\right]^{(-3/2)} \tag{1.27}$$

where θ_{in} is the incidence angle in the gratings. As we can see, choosing the proper distance between gratings, the GDD can be precisely controlled, allowing the pulse to recover its initial duration.

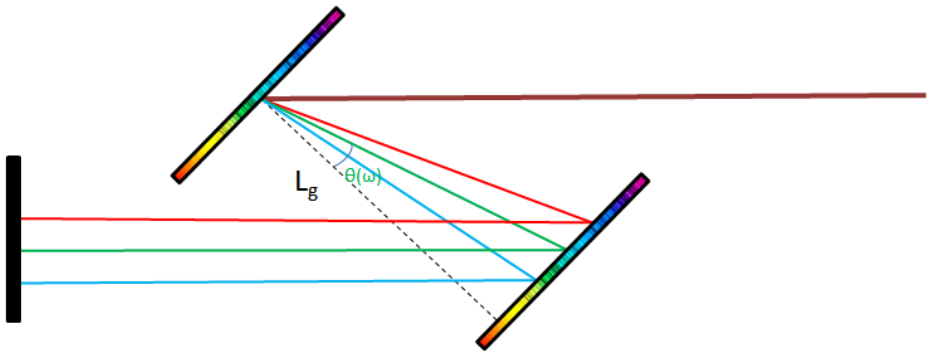

Figure 1.5: Laser compressor composed of two diffraction gratings and a reflector. The configuration is such that a negative GDD is introduced in the pulse.

The damage threshold of the gratings limits considerably the maximum power that a laser can reach. It is important to notice that the pulse has recovered its duration in the last diffraction, so that grating resists the laser at full power. The solution could be to increase the size of the laser beam. But diffraction gratings are fragile components and difficult to produce in big sizes, and so quite expensive.

1.3 Laser ionization

Once we have reviewed the main characteristic of ultraintense laser technology, in the following we will focus on the interaction of ultraintense pulses with matter.

Electrons are bound to the nucleus via Coulomb interaction. Thus, to ionize an atom, an electron has to overcome the attraction from the nucleus. In particular, they can obtain this energy by photon absorption. Ultraviolet, X-ray and γ-ray photons are energetic enough to produce ionization by the absorption of a single photon. For this reason, these kind of electromagnetic radiations are called ionizing radiations. Photons with longer wavelengths, like visible, microwave and radio photons can't ionize atoms by the absorption of one single photon. In consequence, this part of the electromagnetic spectrum is called non-ionizing radiation.

However, with the development of ultraintense lasers the classic definition of ionizing and non-ionizing radiation became rapidly obsolete. The high fluxes of photons that can be achieved with such lasers may induce non linear processes in atoms, e.g., the simultaneous absorption of more than one photon, and thus to introduce new mechanisms of ionization with radiation typically considered as non-ionizing.

For intensities in the range of $10^9 - 10^{13}\,\mathrm{W/cm^2}$ the photon flux is so high that electrons can absorb simultaneously more than one photon acquiring enough energy to overcome the attraction from the nucleus. This process is called *multiphoton ionization* (see Fig. 1.6).

For intensities of $10^{14}\,\mathrm{W/cm^2}$ we reach *tunnel ionization*. The laser electric field begins to be comparable with the Coulomb attraction from the nucleus. Thus, the electric field that the electron feels is the superposition of both contributions:

$$E = \frac{Zq^2}{r} + E_0 \cos(\omega t) \tag{1.28}$$

where ω is the laser frequency and E_0 is the electric field amplitude. Accordingly, the Coulomb potential is deformed allowing electrons to escape from the atom by tunnel effect.

For intensities at the order of $10^{15}\,\mathrm{W/cm^2}$ the electric field is higher than the electric field produced by the nucleus. The potential barrier is so deformed that the concept of atom disappears and the movement of the electron is driven only by the laser electric field. This is called *ionization over the barrier* (also known as *barrier suppression*) (see Fig. 1.6).

For intensities higher than $10^{16}\,\mathrm{W/cm^2}$ the Coulomb potential deformation is so high that most of the electrons are expelled and a plasma is formed.

The leading ionization mechanism is given by the Keldysh parameter, defined as [23]

$$\gamma_K = \omega \sqrt{\epsilon_0 m_e \frac{U_p}{I}} \tag{1.29}$$

where ω and I are the frequency and the intensity of the laser, E_b is the binding energy and m_e is the electron mass. For $\gamma_K >> 1$ the main ionization mechanism is multiphoton ionization. For $\gamma_K \sim 1$ atoms are ionized by tunnel effect. Finally, for $\gamma_K << 1$ the ionization is governed by barrier suppression.

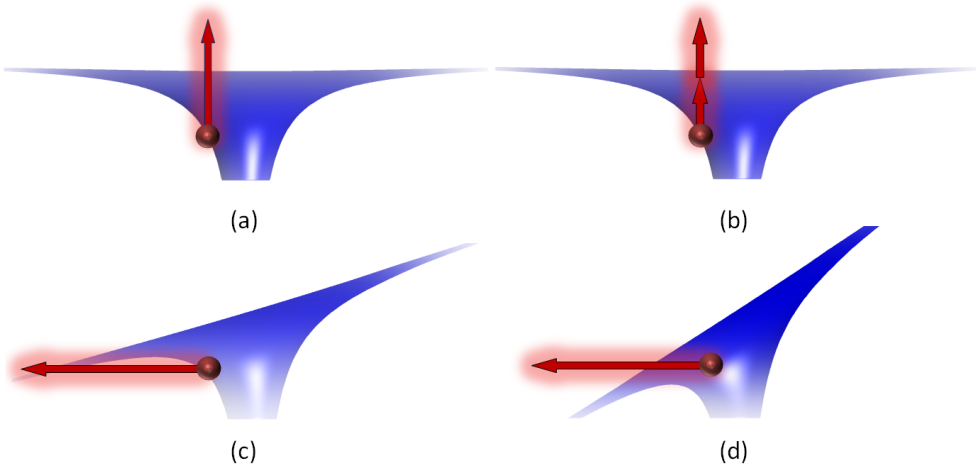

Figure 1.6: (a) Photoelectric effect ionization: the absorbed photon has enough energy to ionize the atom. (b) Multiphoton ionization: the photon flux is enough high to allow the electron absorbs more than one photon at the same time and reach enough energy to escape from the atom. It occurs from intensities greater than $10^9\,\mathrm{W/cm^2}$. (c) Tunnel effect ionization: for intensities higher than $10^{14}\,\mathrm{W/cm^2}$ the laser deforms the Coulomb potential and the electron can escape by tunnel effect. (d) Over the barrier ionization: for $10^{16}\,\mathrm{W/cm^2}$, the laser strongly deforms the Coulomb potential and the electron is above the potential barrier.

1.4 Laser filamentation

When a short ultraintense pulse propagates in a medium, nonlinear effects must be taken into account. In particular, the refractive index cannot be considered constant any more, being necessary to take into account higher orders:

$$n(I) = n_0 + n_2 I \tag{1.30}$$

where n_0 is the linear refractive index, n_2 is the second order refractive index and I is the intensity of the propagating beam. According to this, there is a refractive index gradient across the laser profile, leading to a self-focusing of the laser. It is possible to define a critical power above which the self-focusing effect takes place:

$$P_{crit} = \frac{0.148\lambda^2}{n_0 n_2} \tag{1.31}$$

The critical power does not depend on the original beam area. A larger beam only requires a longer propagation distance until it collapses. For a 800 nm laser propagating in air, $n_2 = 5.0 \times 10^{-19}\mathrm{cm^2/W}$ so $P_{cr} \approx 1.9\,\mathrm{GW}$.

During self-focusing, as the beam is reduced, the intensity rapidly increases, the medium gets rapidly ionized and a plasma is formed. This plasma produces the defocalization of the beam, that counteracts the self-focusing process. Therefore, there is a competition between the convergence leading by self-focusing and the divergence produced by the ionization of the material. As consequence, a plasma filament up to several centimeters is created (Fig. 1.7).

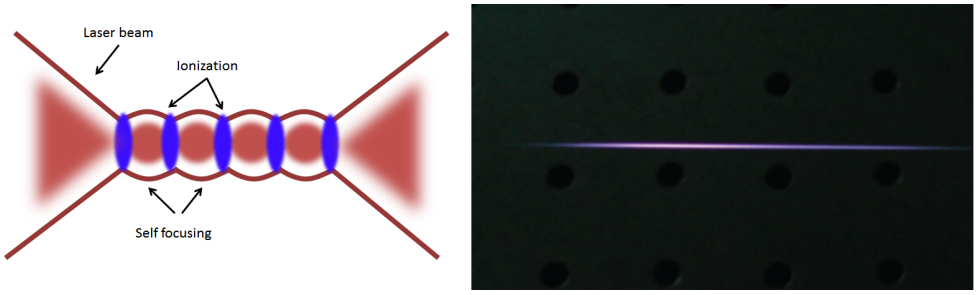

Figure 1.7: Filament created by the competition of the self-focusing of an ultraintense laser and the divergence produced by ionization.

Filamentation plays an important role in this thesis. All experiments carried out in this work took place at atmospheric pressure condition, and with laser powers overcoming the critical power, and thus forming a plasma filament. Since the plasma width is higher that the maximum achievable focus in vacuum, filamentation limits considerably the maximum intensity that we can reach, but presents several advantages, as we will see in the following chapters.

1.5 Electron acceleration

Once the atom is ionized, the free electrons move under the influence of the laser, being the equation that describes this movement:

$$\frac{d\mathbf{u}}{dt} = \frac{q}{m}\mathbf{E}\left(\mathbf{r},t\right) + \frac{q}{\gamma m}\mathbf{u}\times\mathbf{B}\left(\mathbf{r},t\right) \tag{1.32}$$

where $\mathbf{u} = \gamma\mathbf{v}$, $\gamma = \sqrt{1+u^2/c^2}$, c is the light velocity, $\mathbf{E}$ and $\mathbf{B}$ are the electric and magnetic field in the position of the electron and $\mathbf{v}$, q and m are the velocity, the charge and the mass of the electron respectively.

In a first approximation, we can study the electron movement under the influence of a plane wave. Let

$$\mathbf{E}\left(\mathbf{r},t\right) = E_0 e^{-i(\mathbf{k}\cdot\mathbf{r}-\omega t)} e^{-2.77\left(\frac{t}{\tau}\right)^2} \tag{1.33}$$

be the electromagnetic field of the laser, where ω is the frequency of the laser, λ the laser wavelength and τ the pulse duration, measured as FWHM (Full Width Half Maximum).

Figure 1.8 shows the movement of the electron for an intensity of $4\times10^{19}\,\mathrm{W/cm^2}$. We can observe how the electron reaches relativistic intensities, which justify the use of relativistic movement equations. On the other hand, we notice that the electron returns to its initial state of repose after the laser pulse has passed. However, to reach this conclusion we have done rough approximations. Actually, the laser does not have an infinity distribution of energy. Let us assume now a realistic electric field distribution. For example, let us consider a Gaussian beam:

$$\mathbf{E}\left(\mathbf{r},t\right)=\frac{\mathbf{E}_0}{\pi\frac{w(z)}{2w_0}}e^{-\frac{x^2+y^2}{w^2(z)}}e^{-i\left(\mathbf{k}\cdot\mathbf{r}+k\frac{x^2+y^2}{R(z)}-\arctan\left(\frac{\lambda z}{\pi w_0^2}\right)-\omega t\right)}e^{-2.77\left(\frac{t}{\tau}\right)^2} \tag{1.34}$$

where

$$w(z)=w_0\sqrt{1+\left(\frac{\pi w_0^2}{\lambda z}\right)^2} \tag{1.35}$$

is the beam radius in the propagation direction, w_0 is the beam waist and $R(z)$ is the curvature radius, defined as

$$R(z)=z\left(1+\left(\frac{\pi w_0^2}{\lambda z}\right)^2\right) \tag{1.36}$$

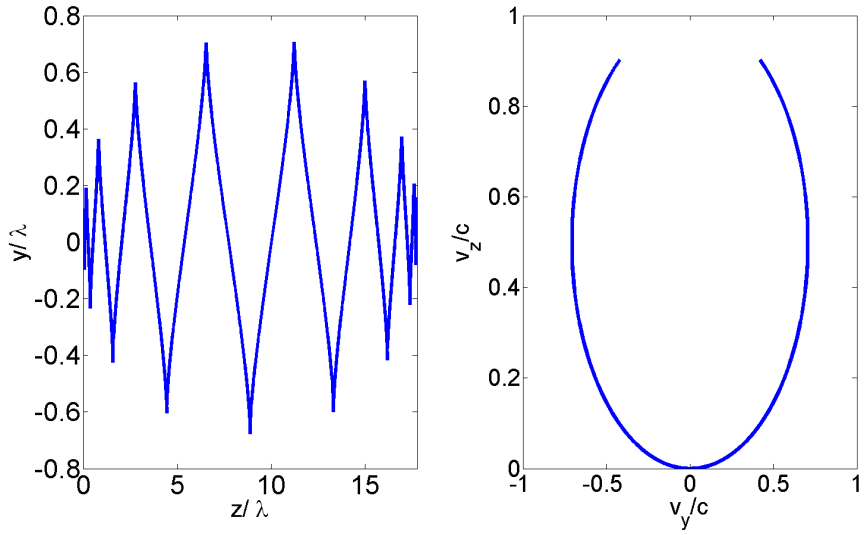

Figure 1.8: Trajectory and velocity of an electron under the influence of a laser pulse of five cycles, 800 nm of central wavelength and an intensity $4\times10^{19}\,\mathrm{W/cm^2}$, considering the laser as a plane wave with infinite and uniform energy. We observe that in these conditions the electron remains at rest at the end of the interaction.

Figure 1.9 shows the electron movement under the influence of this field. We observe that the finite size of the field expels the electron from the electric field and how it acquires a non-zero velocity after the interaction with the pulse.

As we observe in Fig. 1.9, the electron acquires a nonzero velocity with a component in the laser propagation direction. This is important in the production of X-rays with laser. When the laser is focalized on a target, the accelerated electrons are injected into the target. There, they are stopped by the atoms of the material producing the characteristic X-ray lines and Bremsstrahlung radiation.

So far we have just considered the interaction of the laser with an isolated electron. However, in reality the laser interacts with all the ionized electrons and ions at the same time. Picoseconds or nanoseconds before the arrival of the main laser pulse, the intensity is high enough to ionize the material at the focus through the processes that we have described. Thus, when the main part of the pulse arrives, it finds an expanding plasma. As a consequence, we need to refine our description and consider laser-plasma mechanisms for the acceleration of electrons.

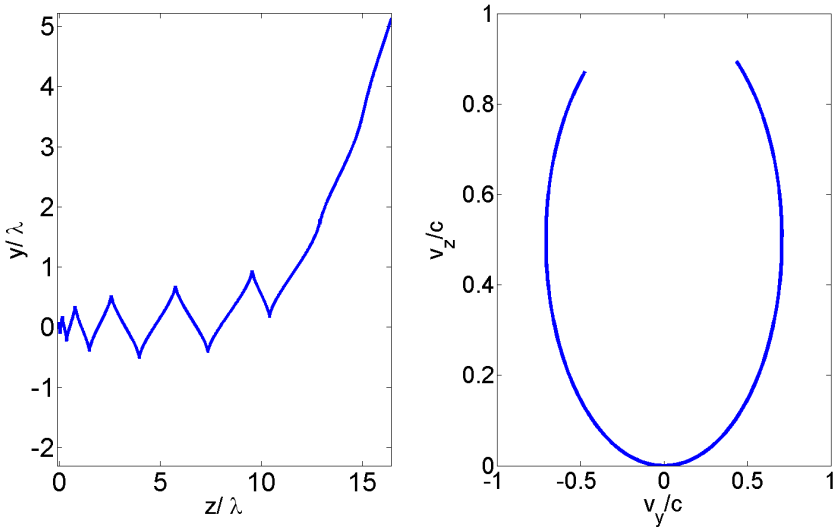

Figure 1.9: Trajectory and velocity of an electron under the influence of a laser pulse of five cycles, 800 nm of central wavelength which has been focalize up to 2 μm ($4 \times 10^{19}\,\mathrm{W/cm^2}$ of intensity). The center of the pulse is at $y = 0$. The electron is in $y = 0.1\lambda$. We can observe how the ponderomotive force expels the electron from the focus, so it has a final non-zero velocity.

1.5.1 Plasma heating mechanisms

As we said, the main part of the laser interacts with a plasma which is created at the first stages of the pulse. The refraction index inside a plasma is defined by:

$$n = \sqrt{1 - \frac{n_e^2}{n_c^2}} \tag{1.37}$$

where n_e is the density of plasma electrons and

$$n_c = \frac{\epsilon_0 m_e \omega^2}{e^2} \tag{1.38}$$

is the critical density, being m_e and e the mass and charge of the electron, and ω is the frequency of the laser. We observe that if $n_e > n_c$ the refraction index becomes imaginary, so the plasma, named overdense, reflects the incident radiation. However, if $n_e < n_c$ the plasma, named underdense, becomes transparent.

For 800 nm, the critical density is 1.75×10^{21} electrons/cm^3. This means that plasmas coming from solids and liquids targets, whose density is usually $> 10^{21}$ electrons/cm^3, are overdense to the laser radiation at that wavelength. On the other hand, plasma created in gas targets, with typical densities in the order of 10^{18} electrons/cm^3, are underdense.

The width of the plasma in which the density increase from 10 to 90% of the maximum plasma density is defined as *scale length*.

Brunel absorption (vacuum heating)

Brunel absorption takes place if the laser is polarized with a component parallel to the plasma gradient (perpendicular to the target) and the scale length is smaller that the laser wavelength. In these conditions, the electric field perpendicular to the target extracts electrons from the plasma and reinjects them once it reverses its oscillation. However, when the electrons reach the point where the plasma density equals the critical density, they escape from the electric field and penetrate inside the target (see Fig. 1.10).

An analytical model estimates the temperature of the electron accelerated by Brunel absorption as [24]:

$$T_e = 8 \left(\frac{I}{10^{16}} \lambda^2 \right)^{(1/3)} \text{[keV]} \tag{1.39}$$

where I is in W/cm^2 and λ is the laser wavelength in μm.

Resonance absorption

Like Brunel absorption, resonance absorption requires a component of the electric field perpendicular to the target. However, resonance absorption is effective when the scale length is

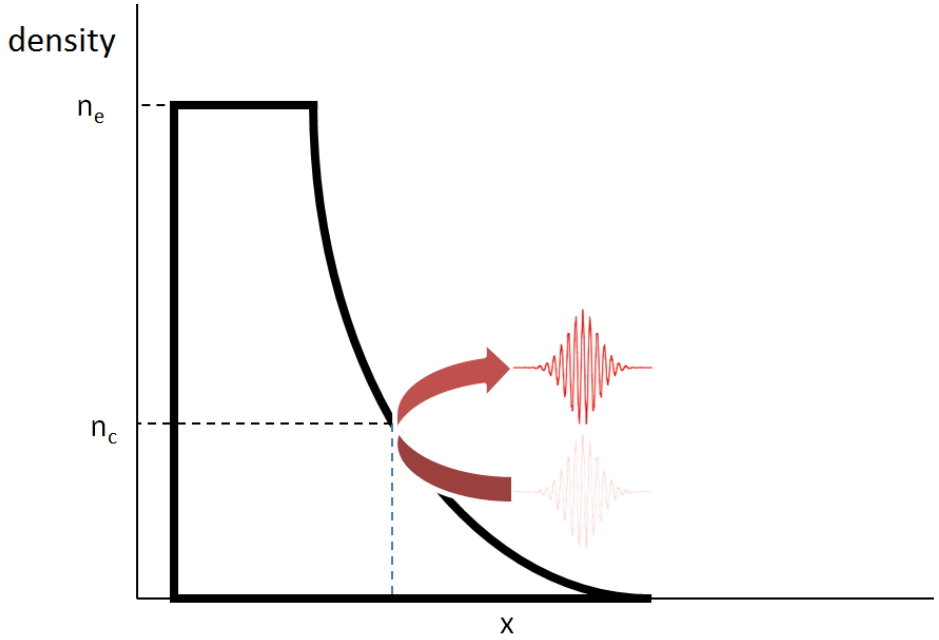

Figure 1.10: Laser reflecting in a expanding overdense plasm. The laser prepulse crate a plasma in the surface of the target. When the main pulse arrives, it can only penetrate in the plasma up to the point where the density reaches the critical density. There, the pulse is reflected.

larger than the laser wavelength. In such conditions, the laser induces resonant movement of the electrons in the point where it is reflected and a large fraction of the incident laser energy is transferred to the plasma wave.

The temperature scaling of the electrons accelerated by resonance absorption follows this expression [25]:

$$T_e \approx 14 \left(\frac{I}{10^{16}} \lambda^2 \right)^{\frac{1}{3}} T_{cold}^{\frac{1}{3}} \text{ [keV]} \tag{1.40}$$

where T_e and T_{cold}, which is the thermal electron temperature, are in keV, I is in W/cm^2 and λ is the laser wavelength in μm.

JxB absorption

For intensities of 10^{18} W/cm^2, electrons reach relativistic velocities and the magnetic field plays a role in the dynamics of their movement. Brunel and resonance absorption lose importance and JxB mechanism governs the plasma heating.

2-dimensional PIC simulations [26] show that the temperature of electrons heated by this mechanism scale as:

Mechanism	**Conditions**	$\mathbf{T_e}$ [keV]
Brunel absorption	Scale Length $< \lambda$	$T_e = 8\left(\frac{I}{10^{16}}\lambda^2\right)^{(1/3)}$
Resonance absorption	Scale Length $> \lambda$	$T_e \approx 14\left(\frac{I}{10^{16}}\lambda^2\right)^{\frac{1}{3}} T_{cold}^{\frac{1}{3}}$
Vacuum heating	$I_{laser} > 10^{18}\,\mathrm{W/cm^2}$	$T_e \simeq 511\left[\left(1+0.73\frac{I}{10^{18}}\lambda^2\right)^{1/2}-1\right]$

Table 1.1: Plasma heating mechanisms. The formulas for T_e are only estimations for a general case. The particular characteristics of the target and the laser could lead to different behaviours.

$$T_e \simeq 511\left[\left(1+0.73\frac{I}{10^{18}}\lambda^2\right)^{1/2}-1\right]\ [\mathrm{keV}] \tag{1.41}$$

Table 1.1 summarizes the three main phenomena that accelerates electrons when an ultraintense laser is focalized on an overdense target.

1.6 Ion acceleration

Ions are too heavy to be directly accelerated by the laser. However, the acceleration of electrons lead to a strong charge separation in the plasma and hence to the formation of an electric field that can accelerate ions to relevant energies. There are several mechanisms of laser-driven ion acceleration depending on the laser intensity or the plasma thickness (Fig. 1.11). In this section we review the most relevant ones.

1.6.1 Coulomb Explosion

When the laser pulse is focalized into a material, atoms are ionized and electrons are quickly expelled. However, since ions are far heavier than electrons, they remain in the bulk of the target. In consequence, a strong repulsion appears, and explosion driven by Coulomb forces takes place.

Coulomb explosion has been specially explored in double layer targets and in cluster targets. The first ones consist in a front layer of heavy atoms and a rear layer of light atoms. The front layer cannot be too thick to allow the laser to create strong field at the rear surface. Ideally, once the laser interacts with the target, all electrons are expelled. Then, the target explodes due to the repulsion of the ions and the light ions are preferentially accelerated.

In cluster experiments, clusters of typically $10^2 - 10^5$ atoms are expelled from a gas nozzle. The laser extracts all the electrons from the cluster and the Coulomb explosion

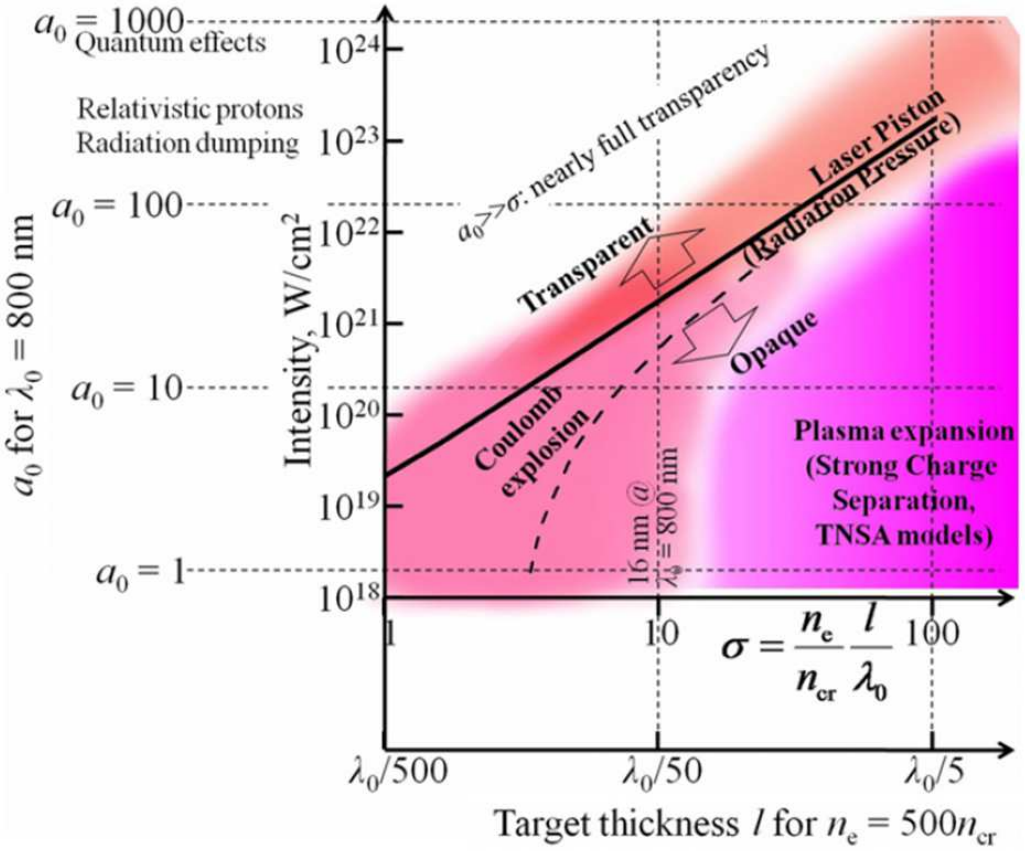

Figure 1.11: Different laser particle acceleration regimes as a function of the laser intensity and plasma thickness. Image from [1]

takes place [27]. Due to its small size, the laser intensity does not have to be too high to produce the explosion. Thus, this mechanism has been observed for intensities below 10^{16} W/cm^2. In Coulomb explosion, ions are expelled in an almost isotropic direction with a moderate anisotropy driven by the laser polarization direction.

1.6.2 Target Normal Sheath Acceleration (TNSA)

As we have seen in section 1.5, when an ultraintense laser is focalized into a solid target, the irradiated front side is rapidly ionized and an expanding plasma is formed. Part of the electrons are expelled out of the target, but some of them are injected into the target (see Fig. 1.12). If the target is thin enough (some microns), electrons are able to reach the rear side of the target and to scape. In this way, a charge separation is present at the rear and front part of the target, and an electric field pointing normal to the surface rises. This electric field is of the order of several TV/m and can be considered quasi-static because electrons are continuously pulled back into the target by the fields and replaced by recirculating hot

electrons from the front. Although the bulk ions are usually too heavy to be efficiently accelerated by this field, impurities as water tipically present in the surface of target can reach high velocities. Protons with energies between 58 MeV [28] to 67 MeV [29] has been observed thank to this mechanism. The energy spectrum is typically exponentially decaying with a sharp high energy cutoff (see Fig. 1.13).

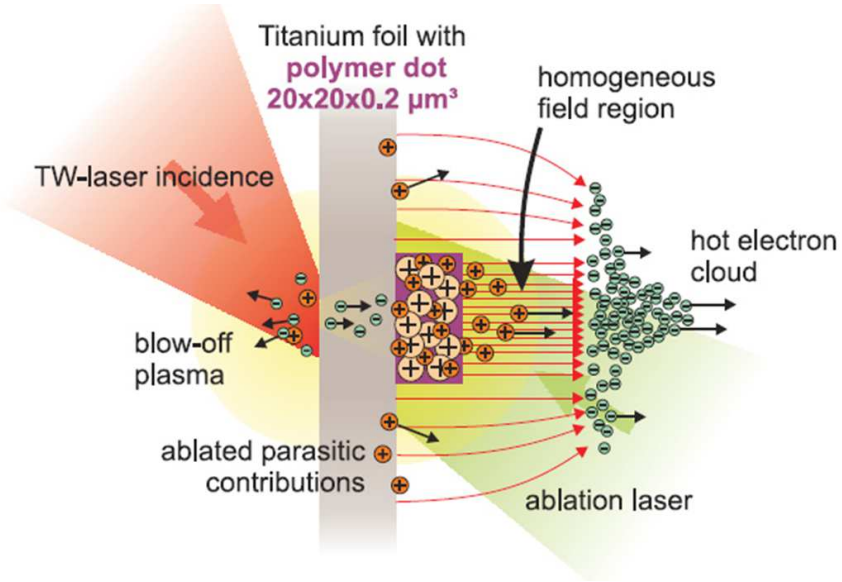

Figure 1.12: Sketch of the Target Normal Sheat Acceleration (TNSA) regime. The laser ionizes the front side of the target. When the accelerated electrons reach the rear side, a strong electric field is created and the ions from the target impurity (water) get accelerated. TNSA requires the presence of a prepulse preceding the main pulse strong enough to produce a preplasma in the target before the arrival of the main pulse. Image from [30]

Although the most energetic ions are expelled from the rear side of the target, also it is possible to find ions accelerated from the front side, but quite less energetic due to the lower field and the limited acceleration time. Also these ions typically exhibit a larger angular spread.

1.6.3 Radiation Pressure Acceleration (RPA)

When the laser irradiance is extremely high ($> 10^{22}\,\mathrm{W/cm^2}$), the radiation pressure is relevant and leads to a very efficient acceleration mechanism called radiation pressure acceleration (RPA) or laser piston regime.

In this scenario, a laser pulse with sufficiently large focal spot pushes forward the electrons by radiation pressure, producing a large separation field that accelerates the ions of the irradiated area. If the field is strong enough, ions are quickly accelerated to relativistic

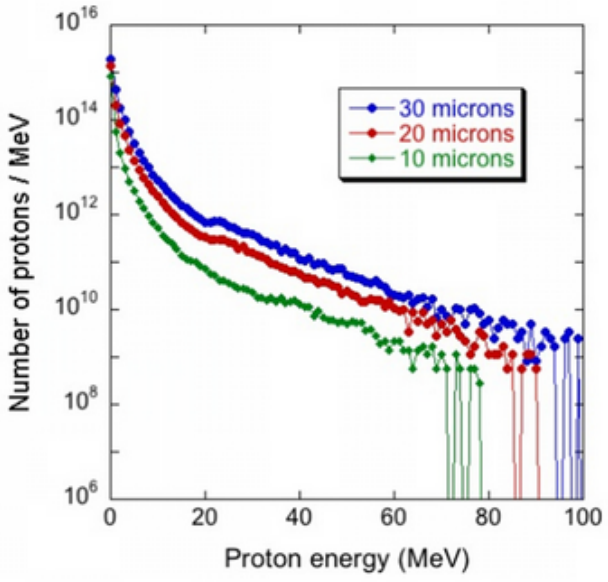

Figure 1.13: Typical TNSA spectrum performed by PIC simulations for different FWHM of the laser. We can observe a broad spectrum with a sharp energy cuttoff. Image from [31]

velocities and, in consequence, the distance between electrons and ions remains small. In such situation, ions and electrons move together forming a relativistic mirror, the so called Light Sail paradigm [32] (see Fig. 1.14). When the foil velocity approaches c, it becomes high reflective and almost all the energy of the laser pulse is transferred to the foil. Once the pulse is reflected or absorbed, ions take most of the energy of the electrons due to their much larger mass.

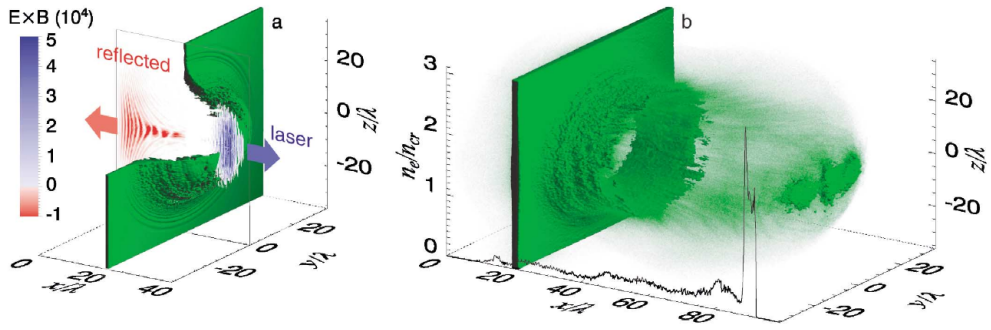

Figure 1.14: PIC simulations of the Light Sail mechanism. Image from [32]. In a first step, a relativistically strong laser pulse irradiates a thin foil with thickness where the laser pulse waist is sufficiently wide, so the quasi-one-dimensional geometry is in effect. Electrons are quickly accelerated and creates a charge separation field. In a second step, the accelerated foil, which consists of the electron and ion layers, can be regarded as a relativistic plasma mirror copropagating with the laser pulse.

Compared with TNSA, Light Sail mechanism produces narrower energy spectrum and emission cone. TNSA accelerates preferentially the protons from the contaminant layer, but in light sail all the bulk ions are accelerated by the charge-separation field. Light Sail also requires lasers with high contrast to avoid the target being destroyed before the arrival of the main pulse. Although high intensities are needed for RPA, this regime can be triggered for lower intensities ($\sim 10^{20}\,\mathrm{W/cm^2}$) if circular polarized beams are used.

Hole boring [33] or collisionless shock acceleration is another case of RPA that occurs when the target cannot be considered as a thin foil. In this case, electrons are still pushed forward by radiation pressure creating a thin electron spike in front of the pulse. The charge-separation field accelerates ions and a ion spike is formed following the electron spike (see Fig. 1.15).

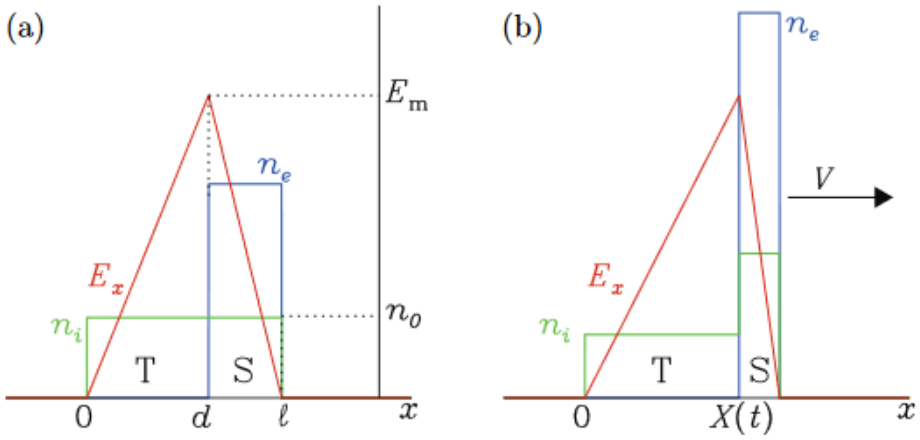

Figure 1.15: Sketch of Hole Boring. Image from [34]. First, the laser push and pile the electrons of the target. Then, a peak of ions is accelerated by the charge separation field.

1.6.4 Break-out afterburner (BOA)

When electron energies exceed their rest mass ($511\,\mathrm{kev/c^2}$, the effective electron mass increases by $\gamma = 1/\sqrt{1 - v^2/c^2}$, and so the refraction index becomes

$$n = \sqrt{1 - \frac{n_e^2}{\gamma n_c^2}} \tag{1.42}$$

If $n_e^2 > \gamma n_c^2$, the overdense plasma becomes relativisticly transparent and a new mechanism can take place: Break-out afterburner (BOA) [35, 36]. This mechanism is divided in two phases. The first phase is similar to TNSA: a linear polarized beam heats the electrons so they can travel trough the target to finally create an electric field in the rear side. As electrons in the front side of the target reach relativistic energies, that part of the target

becomes relativistic transparent and the laser penetrates more. If the target is sufficiently small, it becomes completely transparent to the pulse. In the second phase, the longitudinal field created by the charge separation accelerates ions to high energies. Since the target is transparent, electrons recover their lost energy. The process ends when the target becomes classically underdense because of the expansion of the plasma.

The target thickness for BOA must be carefully chosen. A too thin target becomes classically underdense too soon, while a too thick target do not experiment BOA.

1.7 Neutron Acceleration

Neutrons are non-charge particles and, in consequence, do not interact with the electric field of a laser. However, high energetic neutrons can be produced in nuclear reactions induced by the accelerated ions, electrons or γ photons generated by laser-plasma interactions. The most relevant mechanisms to produce accelerated neutrons are discussed in the following sections.

1.7.1 Nuclear Fusion

The most used mechanism for neutron production is nuclear fusion [37,38]. The high cross-section of different nuclear reactions allows to obtain neutrons with moderate ion energies, which are achievable via laser acceleration. A double target in a pitcher-catcher configuration is used to produce neutrons (see Fig. 1.16).

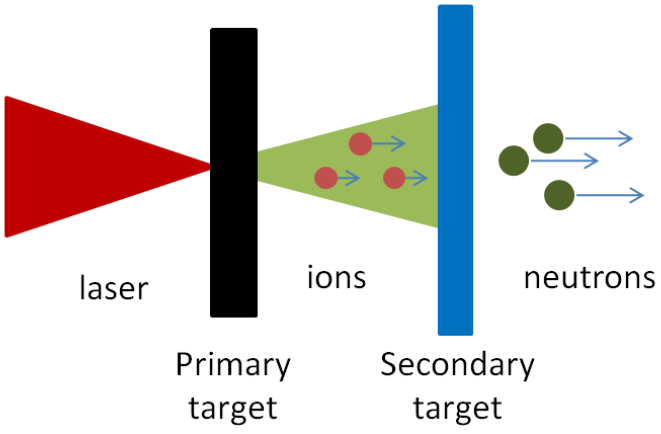

Figure 1.16: Schematic of the dual target configuration for nuclear fusion induced by laser accelerated ions. As an example of this configuration, we can find deuterated polystyrene (CD) as pitcher to produce nuclear reactions in a CD catcher, Au/CH $\rightarrow$ CD or CD+Al $\rightarrow$ CD.

In this configuration, ions are accelerated in the first target, called catcher, and shot over the second target, called pitcher, where the nuclear reaction takes place. Several ion acceleration mechanisms and different targets can be used in order to obtain the proper ion energy to induce the nuclear reaction. One advantage of this configuration is the directionality of the neutron beam due to the kinematics of the reaction.

1.7.2 Photonuclear reactions

High energetic γ photons can excite nuclei and lead to the emission of nucleons. The cross-section of these reactions is tipically in the order of MeV. Thus, the high energetic electron beams produced by laser plasma acceleration can be used to produced the required γ photons via Bremsstrahlung. A neutron source via photonuclear reaction has been demostrated by using a Cu converter to generate Bremsstrahlung with accelerated electrons from a plastic target [39] (^{65}Cu$(\gamma, \mathrm{n})^{64}$Cu and ^{63}Cu$(\gamma, \mathrm{n})^{62}$Cu, with cross section peaks in the range of 10-25 MeV).

1.7.3 Spallation reactions

Despite the ion energy required for spallation reactions is far from the obtained by laser acceleration, this process represents a possible future way to obtain neutron sources [40]. A spallation reaction consists in the release of several neutrons from high-Z nuclei following the bombardment with high energetic particles. Although this process is similar to nuclear fission, it has several differences. In nuclear fission, the absorption of thermal neutrons by the nuclei lead to the break-up of the nucleus followed by a nuclear decay with neutron emission. This process is exothermic and produce high energetic neutrons that can initiate a chain reaction. In spallation reaction the chain reaction is not possible because it is an endothermic process. In this case, the nucleus is bombarded with high-energy ions that produce its excitation. Then, nuclear evaporation occurs, i.e., the nucleons escape during the nuclear decay, resulting in the neutron source. The ion energy necessary to produce spallation is in the order of hundred of MeV, which, as it was mentioned, is still far from the usual laser-driven ion acceleration energies.

1.8 Possible applications

Laser-driven particle acceleration has promising applications, being one of the main advantages of this technology the price compare with the larger accelerator facilities. While a linear accelerator needs some hundreds of meters to accelerate electrons up to 1 GeV, an ultraintense laser can do it in only one centimetre [41]. This is an special advantage in ion

acceleration. For example, the protontherapy, which consists in irradiating tumours with accelerated protons or ions, is a well-established treatment but quite expensive. There are only few centres in the world where the protontherapy can be applied due to the huge infrastructure that is required to accelerate ions up to useful energies. The objective of the scientific community is to find the way to efficiently accelerate ions with laser, so ultraintense lasers could substitute the large accelerator facilities.

In the same way, laser accelerators could be used to produce radiopharmaceuticals used in Proton Emission Tomography (PET). This radioactive substances only have some hours of lifetime. They must be injected to the patient just after its production. The expensive accelerator that they require to be produced limits the places where a PET could be located. However, if we were able to produce radiopharmaceuticals with laser accelerated ions, the technology would be cheaper and every hospital could have a laser near the PET systems.

Neutron generation via laser-acceleration ions can be also used for cancer treatment [42, 43], but they have other promising applications, like fast neutron radiography [44], neutron resonance spectroscopy [45] or material testing for fusion energy research [46].

Laser accelerated electrons have also medical applications. In particular, they could be a source for intraoperative radiotherapy. The most damage cause by electrons is located in the surface of the irradiated tissue, so usually they must be used in an intraoperative way. However, this requires to move the patient in an sterilized environment or to have the accelerator systems in the operating room. An ultraintense laser, however, could be located in some place of the building and the beam could be guided to the location of the patient, giving service in addition to multiple surgery rooms.

Apart form this, accelerated electron generates X-rays that have multiple advantages and applications. As this issue is one of the central points of this thesis, it will be discussed in detail in Chap. 4.

However, we have to take into account that particle accelerators are well-established technology and their commercial world is rapidly maturing [47]. So to compete with them, not only an effort in discovering new applications must be done, but an effort in trying to overcome them in price and quality. In consequence, in this thesis we have studied new targets that could offer a robust source, as we will see in Chap. 2, as well as modifications in the laser system that could cheapen the final system cost, which will be presented in Chap. 5.

Chapter 2

X-ray generation by laser

2.1 Introduction

In this chapter, we present a laser driven X-ray source based on the mechanisms that take place when an ultraintense laser is focalized in a target and the atoms of the material are ionized.

First we present the radioactive facility where the experiments took place. Then, a conventional source with a solid target is presented. Finally, to overcome the problems that the use of a solid implies, mainly robustness and repeatability, a liquid curtain is analysed as a target.

2.1.1 X-ray generation

Once the electrons has been accelerated by the laser via the processes presented in Chapter 1 (Brunel absorption, resonance absorption or vacuum heating), there are two mechanisms that generate X-rays: bremsstrahlung and the creation of vacants in the atoms of the target, which leads to the emission of atomic characteristic lines.

Bremsstrahlung X-rays

The accelerated electrons penetrate into the target and lose energy by collisions with the atoms of the target, producing Bremsstrahlung in the process (see Fig. 2.1). The energy spectrum of the accelerated electrons can be described by the contribution of two Maxwell-Boltzmann distributions. One of the distributions corresponds to the electrons that are directly accelerated by the laser, and the other, which is less energetic, corresponds to the electrons that are accelerated in the plasma expansion.

The Bremsstrahlung photon distribution produced by a Maxwell-Boltzmann distribution of electrons can be expressed as [48]:

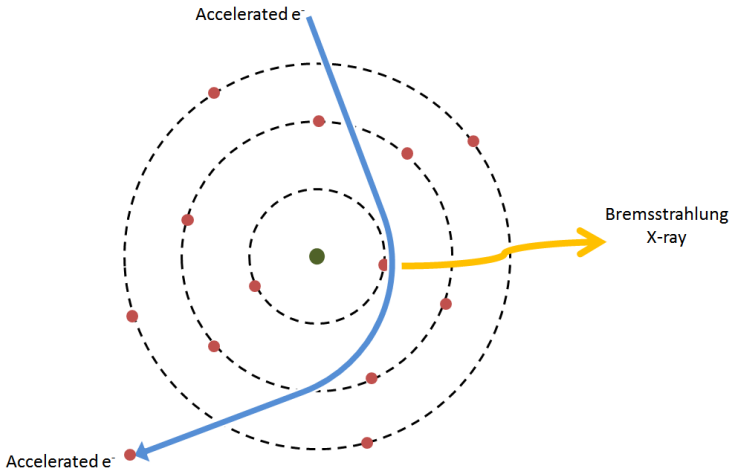

Figure 2.1: Bremsstrahlung X-ray emission. The accelerated electrons produce X-ray radiation when are stopped by the atoms of the target.

$$\frac{dN_\gamma}{dE_\gamma} \propto \frac{2e^{\frac{-E_\gamma}{kT_e}}\sqrt{E_\gamma kT_e} + (kT_e - 2bE_\gamma)\sqrt{\pi}\mathrm{erfc}\left(\sqrt{\frac{\mathrm{E}_\gamma}{\mathrm{kT_e}}}\right)}{3E_\gamma kT_e\sqrt{\pi}} \tag{2.1}$$

For $E > kT_e$, this distribution behaves as:

$$\frac{dN_\gamma}{dE_\gamma} \propto \frac{e^{\frac{-E_\gamma}{kT_e}}}{\sqrt{E_\gamma kT_e}} \tag{2.2}$$

For $E >> kT_e$, the distribution asymptotically tends to $\exp(-E/kT_e)$. Hence, the hot electron temperature can be obtained by a fitting of the bremsstrahlung spectrum for high energies.

Characteristic X-rays

Besides the X-ray emission produced by bremsstrahlung, characteristic X-rays of the target material are also produced. The accelerated electrons suffer high energetic collision with the atoms of the target that can extract electrons from the inner levels of their electronic structure. These vacancies are rapidly occupied by electrons of superior levels, generating characteristic X-ray lines in this process (see Fig. 2.2).

2.2 Radioactive Facility (IRA)

The laboratory where the experiments presented in this section have been carried out is considered as Radioactive Facility (IRA) of third category. IRA is the title given by Gov-

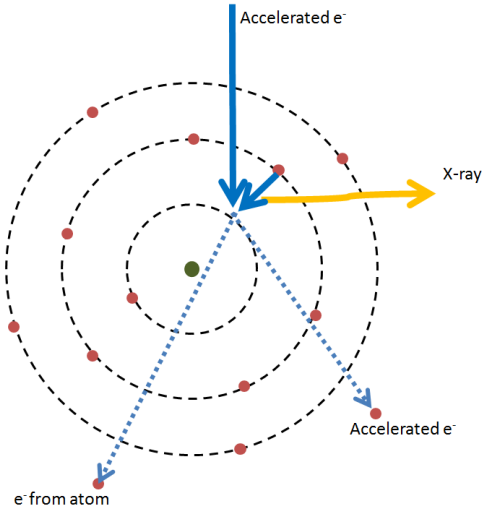

Figure 2.2: Characteristic X-ray emission. The accelerated electrons extract electrons from the inner layers of the atom. The desexcitation of the ion produces the characteristic X-ray lines.

ernment of Spain to the facilities as laboratories, industrial workplaces or hospital rooms where radioactive activities take place. Our facility, however, is singular because is the first one in Spain that has a radioactive installation associated to an IR laser, that according to the spanish law is considered non-ionizing radiation independently of the intensity. This represented an important breakthrough in the Spanish legislation of radioactive activities.

There are three categories in the classification of IRAs:

1. First Category radioactive facilities:
    - Factories producing uranium, thorium and its compounds.
    - Factories producing natural uranium fuel elements.
    - Installations using radiation for irradiation industrial purposes.
    - Complex facilities in which big amounts of radioactive substances are manipulated or high energy beams are produced with a potential radiological impact to the installation.
2. Second Category radioactive facilities:
    - Facilities in which radioactive nuclei are manipulated or stored for scientific, medical, agricultural, commercial purposes or industrial uses. The allowed activity is equal to or greater than 1000 times the limit established by the legislation.
    - Installations using X-ray apparatus with a peak voltage of over 200 kilovolts.

- Particle accelerators and facilities where neutron sources are stored and where First Category rating is not applicable.

3. Third Category radioactive facilities:

   - Facilities in which radioactive nuclei are manipulated or stored and where the allowed activity is less than 1000 times the limit stablished by the legislation.
   - Facilities that use X-ray apparatus with a peak voltage of less than 200 kV.

As we mentioned, IR radiation does not have enough energy to ionize atoms by the absorption of a single photon, and so the Spanish legislation considers it as a non-ionizing radiation. In consequence, laser facilities had never been taken into account so far when a IRA had to be licenced.

However, the Spanish Center for Pulsed Lasers (CLPU) has made an effort to fix this gap in the legislation (see Fig. 2.3). Thanks to its work, Spanish Government recognised the dangers that exist in a laboratory with an ultraintense laser, probing that a typically non-ionizing radiation can ionize atoms via non-linear processes and also produce ionizing radiation. Following this reasoning, the Center has licenced the first IRA associated to a laser (IRA number 3254). I collaborated in the set-up of this IRA and became a licenced supervisor of the facility.

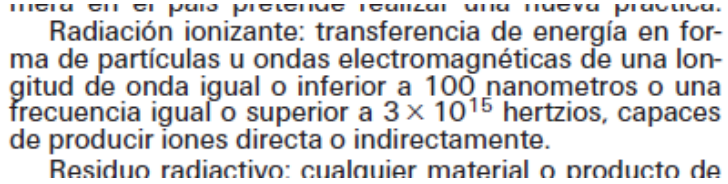
mera en el país pretende realizar una nueva práctica.
Radiación ionizante: transferencia de energía en forma de partículas u ondas electromagnéticas de una longitud de onda igual o inferior a 100 nanometros o una frecuencia igual o superior a 3×10^{15} hertzios, capaces de producir iones directa o indirectamente.
Residuo radiactivo: cualquier material o producto de

Figure 2.3: Spanish legislation for ionizing radiation. Only electromagnetic radiation of less than 100 nm wavelength is considered ionizing. Published in BOE of July, 21th 2001.

Afterwards, this licence has been extended to include the VEGA laser target area, increasing its category from third to second.

2.2.1 IRA 3254

In this section we present the IRA 3254. We take into account only the part of the licence that concerns to the X-ray station, which is the place where the experiments of this thesis took place.

The facility was conceived to carry out experiments of X-ray generation and electron acceleration with an ultraintense laser by focalizing the laser in a target, usually a metallic

sample. The mechanisms that were mentioned in Chap. 1 take place, atoms of the material are ionized, electrons are accelerated and X-rays are produced. The X-ray emission can be considered isotropic, as we will see when discussing the experimental results, while accelerated electrons are mainly produced in the reflection direction of the laser.

To obtain the IRA licence, the station must offer security measures for the people that work there and for the people that work in the surroundings. For that, the distribution of the laboratory was designed as Fig. 2.4 shows.

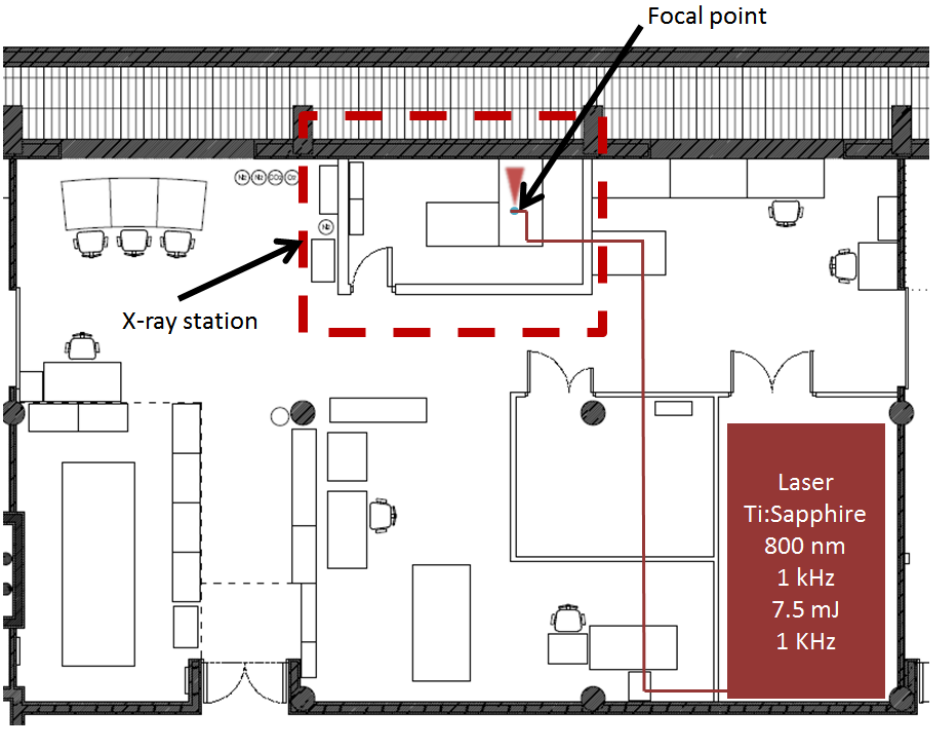

Figure 2.4: Plan of the X-ray station. The 7.5 mJ of the laser are divided between the different experimental stations in the laboratory. The X-ray station receives 2.5 mJ as maximum. The walls of the station have 2 mm thickness lead sheets to avoid any radiation leak to the exterior.

The room must have proper shielding to avoid radiation coming out of the room. Electrons must be stopped with a material of low atomic number to avoid the generation of high energetic Bremsstrahlung. However, to efficiently stop X-rays a material with high Z must be used. The disposal of the experimental setup directs the primary radiation emission to the external wall of the laboratory, where tens of cm of concrete stop both electrons and X-rays. The rest of the walls were constructed including in their design a lead sheet of 2 mm thickness for stopping the X-rays. The setup is enclosed in a box made by methacrylate (PMMA) of 5 mm thickness for stopping the electrons. The continuous slowing down ap-

proximation range (CSDA), that is the average path length travelled by a charged particle as it slows down to rest calculated in the continuous-slowing-down approximation is $0.59\,\mathrm{g/cm^2}$ for electrons of 1.25 MeV. Taking into account that the density of PMMA is $\rho = 1.18\,\mathrm{g/cm^3}$, that means that $\mathrm{CSDA}/\rho = 0.5\,\mathrm{cm}$ of methacrylate can stop electrons of less than 1.25 MeV, which is more than enough for the electrons generated in the station, as we will see.

The station has two modes of operation:

- **Optical mode:** In this mode, the maximum achievable laser intensity is not sufficient to produce ionization of the target.
- **Radioactive mode:** In this mode, the interaction of the laser with the target produces ionization with the subsequent emission of X-rays and accelerated electrons. No one can stay inside the station while this mode is activated. The critical optical elements are controlled remotely.

To guarantee the safety of the workers, a security interlock was built at the entrance of the laser in the room. This interlock consists in a neutral optical filter and a shutter. During the optical mode, the filter reduces the energy of the laser up to security levels. In the radioactive mode, the filter is removed. In case of necessity, some emergency buttons are placed in the laboratory. If pressed, the shutter blocks immediately the laser. To change from optical mode to radioactive mode, the station supervisor must check that there is no one inside the room, press a "last person button", go out and close the door. A key next to the station allows to remove the filter if the "last person button" is pressed and the door is closed. When the key is removed, the filter returns to its position. Some cameras allows the supervisor to watch the station from the outside during radioactive mode.

2.3 Experimental setup

We have used a commercial GW laser constructed by Spectra Physics. The laser is a Ti:Sapphire system that emits pulses of 120 fs of duration, with 800 nm of central wavelength, 1 kHz of repetition rate and a waist of 0.6 cm FWHM. The system can provide up to 7.5 mJ per pulse, i.e., 60 GW, but only 2.5 mJ are sent to the X-ray station. The rest of the energy is used in other experimental stations of the laboratory.

To focalize the laser (see Fig. 2.5), we have used a microscope objective of NA = 0.42. At low energy (only few microjoules), we achieved a focal spot of $1.5\,\mu\mathrm{m}$ in the horizontal and $1.2\,\mu\mathrm{m}$ in the vertical (see Fig. 2.6). Typically, we used up to 1.0 mJ when we worked with the microscope obective to avoid damaging the optics. With this spot size the expected intensity is around $\sim 5 \cdot 10^{17}\,\mathrm{Wcm^{-2}}$. However, we must notice that even with 1.0 mJ the

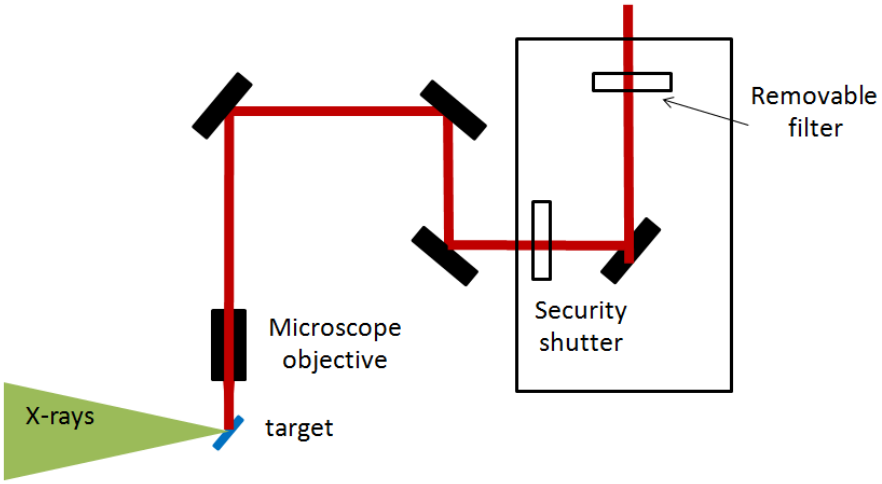

Figure 2.5: The laser was focalized with a NA = 0.42 microscope objective in a solid target. A filter reduced the intensity of the laser to work with the setup without radioactive hazards. In case of danger, an emergency shutter was placed to block the laser beam and so to stop the radiation production.

power of the laser is higher than the critical power of air ($\approx 1.9\,\mathrm{GW}$). That means that we fullfill the conditions for laser filamentation. In consequence, when working with 1 mJ, the focal spot was considerable larger due to filamentation (see for example [49] and reference therein). By imaging the plasma created by filamentation in air, an upper limit of the size of the focus can be obtained. In that case, we estimated a focal spot with a diameter of the order of $100\,\mu$m and a filament extension of around $200\,\mu$m yielding to an minimum intensity of the order of $10^{14}\,\mathrm{Wcm}^{-2}$.

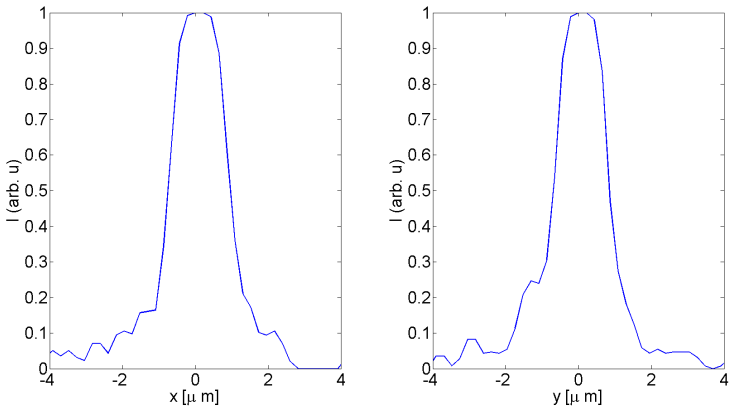

Figure 2.6: Laser focal spot for the X-ray generation experiments. We achieved a focal spot of $1.5\,\mu$m in the horizontal and $1.2\,\mu$m in the vertical

The laser intensity at the focus is so high that any material is ionized. That is, any material can be used as a target for X-ray generation. When the laser pulse hits a solid target, some portion of the material is ablationed and a hole is created. If we want to obtain a stable source, we have to avoid the overlapping of the laser pulses. For this purpose, we put the sheet of the solid target in a motorized stage that spins it and moves it along the plane of its surface. Thus, the laser described an spiral, finding each pulse a fresh zone of the target.

To measure the X-ray spectrum we have used an Amptek X-SDD-123 detector. This detector is based in a Si-PIN photodiode with a cooler that reduces the electronic noise. Semiconductor spectrometers allowed us to measure the generated X-ray spectrum, but it must be taken with caution, because it is easy to suffer from pile-up in the measurement. Pile-up happens when the detector is not capable to discriminate between two events that are close in time. In this case, rather than two events, the detector emits a signal corresponding to a single event but with double the energy. Unfortunately, this is a common problem for particle and radiation spectrometers that becomes specially relevant for pulse radiation due to the high instantaneous fluxes achieved. Nowadays, due to the fast development of laser-based ultrashort particle and radiation sources there is a growing interest in this instrumental artefact.

Figure 2.7 shows an example of the pile-up problem. We observe the normal spectrum that is obtained with the Amptek detector and the same spectrum measured with a methacrylate filter. We can observe how the filter reduces the photon flux and avoids pile-up. In this case, the counts per shot without filter are 0.57 counts per shot, while the presence of the methacrylate reduces this number up to 0.13 counts per shot.

It is important to mention that Amptek detector measures counts per channel. There is a linear relation between channel and photon energy, which also depends on the measurement parameters of the detector. In particular, it depends on the gain of the detector. To calibrate the energy-channel relationship, we used an americium source with known emission as well as K_α lines form different targets in the experiments.

The width of each channel of the Amptek spectrometer is proportional to the gain applied in the detector. That means that the height of the K_α and K_β peak depends on the gain. To obtain a correct spectra, one must divided the counts per channel per the energy width of the channel.

Although a conversion from count to photons could be done, we decided to show in this thesis the raw spectra (with a FFT filtering) from the detector for the following reasons:

- Unfortunately there is at the moment no detector specifically devoted to ultrashort – in the femtosecond time regime- and with huge instantaneous fluxes radiation, being necessary to use conventional detectors for these measurements. Thus, we must be

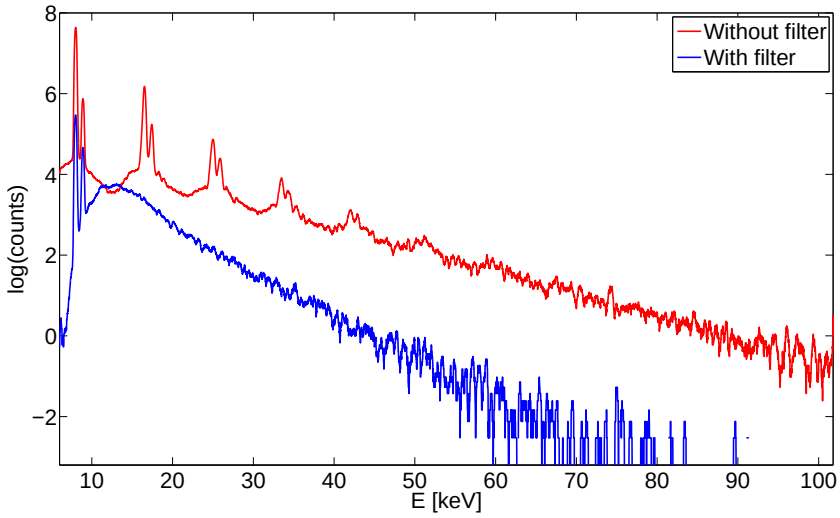

Figure 2.7: Typical spectrum obtained with Amptek Detector X-SDD-123 placed at 90 cm from our X-ray source in the direction of the laser reflection. Red line corresponds to the direct measurement of the spectra. Blue line is the same spectra but with a 0.5 mm methacrylate filter in front of the detector which reduces the photon flux reaching the detector. We can observe peaks at 8.0 and 8.9 keV, which corresponds to the K_α and K_β lines of the copper target. The continuum part of the spectra corresponds to the Bremsstrahlung radiation. If the photon flux is too high (red line), pile-up occurs and the detector consider two or more events as a single one with the energy of the sum of the events. A filter must be used to reduce the flux and avoid pile-up (blue line).

really careful when transforming the data from the detector, .i.e., count per channel, to photons: not only phenomenon like pile-up can be extremely relevant, but instantaneous saturation of the active medium of the detector -this is different from the electronic dead-time inherent to any device- can play an important role. So far, all these processes are not fully understood existing at the moment several groups devoted to this (we are also studying these phenomena at CLPU).

- For those readers who may use the thesis as a reference or for comparison, we believe it is more useful to have at first glance the raw data from the spectrometer than those corrected for the filters and the detector efficiency.

In this context, and from a conservative point of view, we rather preferred to keep the raw data from the spectrometer, except from the calculation of the electron temperature and the estimation of the efficiencies.

2.3.1 X-ray emission

In Fig. 2.8 we can observe a typical spectrum from our source. In this case, the target was a sheet of copper. We can observe the mentioned two contributions in the X-ray spectrum. On one hand, we have the characteristic lines of the target. In our case, we have the K_α and K_β lines of copper, which correspond to an energy of 8.0 and 8.9 keV respectively. On the other hand, we have a continuous spectrum of X-rays, which corresponds to the Bremsstrahlung emission of the accelerated electrons.

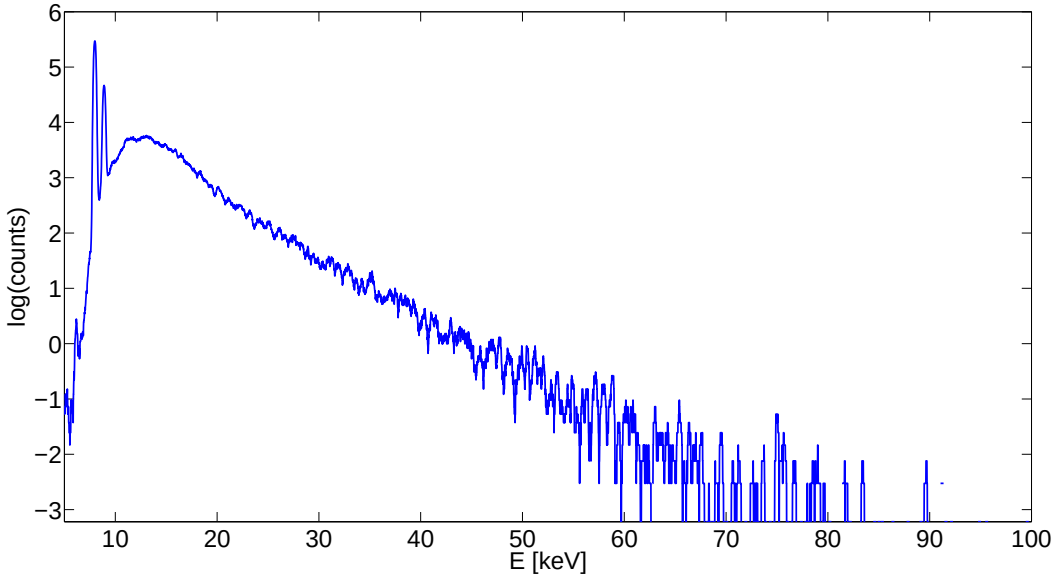

Figure 2.8: X-ray emission from a Cu target. A smooth filter has been applied to avoid the fast oscillations produced by spurious noise. The pulse energy was 1.0 mJ. The spectrometer was placed at 90 cm from the source in the laser reflection direction. A 0.5 cm methacrylate filter was put to avoid pile-up. We observe the contribution of the bremsstrahlung and the characteristic lines from copper (K_α and K_β at 8.0 and 8.9 keV respectively).

To have an estimation of the electron temperature, we can deconvolute the measured spectra with the transmission of the filters (90 cm of air + 0.5 cm of methacrylate) and the efficiency of the detector. Figure 2.9 shows the result if these factors are taken into account. If we fit this part of the spectrum to the function:

$$A\frac{e^{\left(-\frac{E}{T_{hot}}\right)}}{\sqrt{ET_{hot}}} \tag{2.3}$$

we have an estimation of the hot electron temperature, that is, the energy of the electrons directly accelerated by the laser, which is 30.1 keV in this case. In the following sections,

we will compare this value with the temperature obtained for the liquid target and we will discuss the mechanism that lead to these results.

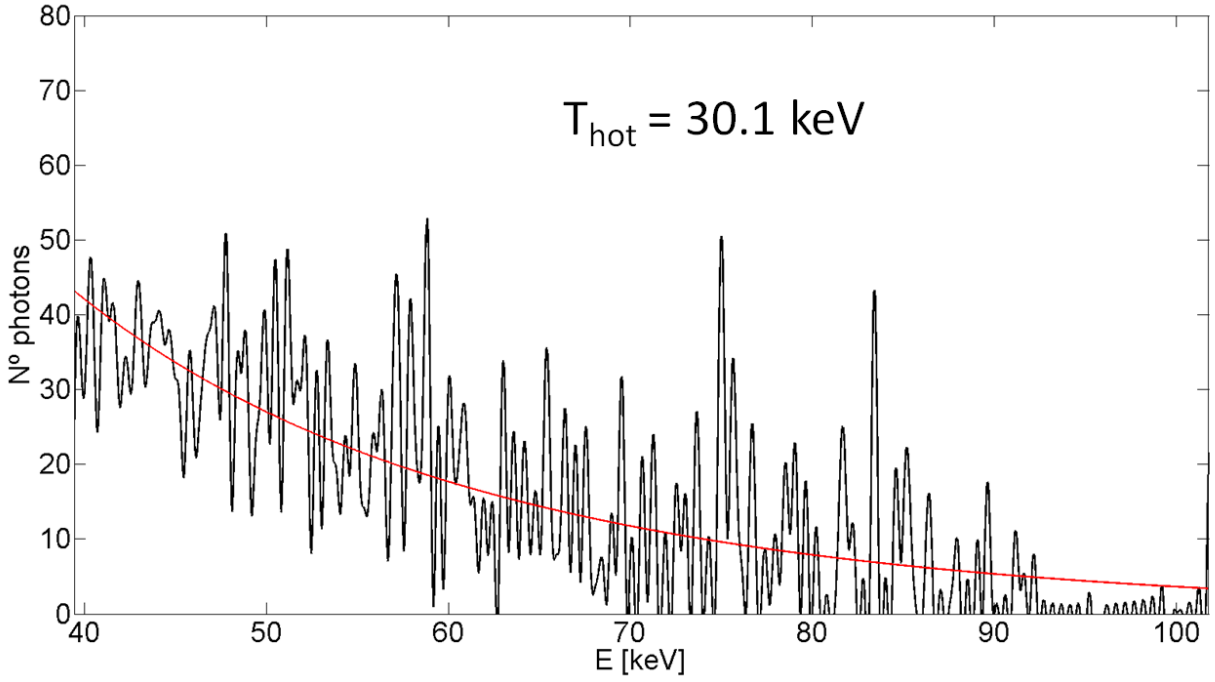

Figure 2.9: X-ray emission from a Cu target showed in Fig. 2.8 taking into account the transmission of the filters and the efficiency of the detector, and thus having an estimation of the photons arriving to the detector. A fit for high energy to the equation 2.3 gives us 30.1 keV for the hot electron temperature.

2.3.2 X-ray yield vs laser energy

As we established in chapter 1, the efficiency of our source is limited by filamentation. When a laser pulse filaments, the intensity along the filament path remains constant. An increment in the pulse energy does not imply an increment in the intensity along the filament, but an increment in the longitude of the filament and/or the birth of a second filament (multifilamentation). Thus, it is worth asking which is the dependence of the X-ray emission efficiency as a function of the pulse energy.

Figure 2.10 shows the X-ray emission for different laser pulse energies. We can observe how the photon emission increments with the pulse energy from 0.1 mJ to 0.9 mJ. However, the emission for 1.0 mJ is practically the same than for 0.9 mJ. We attribute this to the fact that the intensity in the filament saturates and the effects of the laser pulse are the same that for 0.9 mJ. Below 0.1 mJ, the laser did not have enough energy to ionize the target or to produce a measurable X-ray signal.

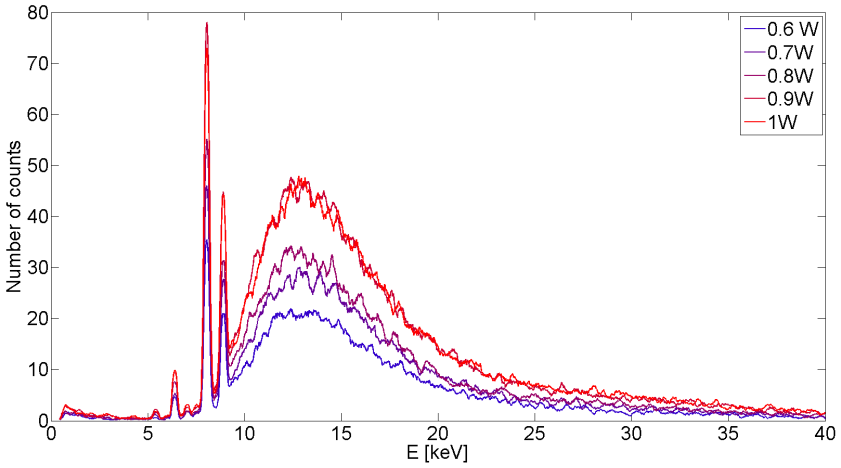

Figure 2.10: X-ray emission from a Cu target as a function of the pulse energy. The saturation in the X-ray conversion yields suggests a limit in the maximum achievable intensity in the laser spot due to filamentation.

2.3.3 Angular X-ray emission

We have measured the X-ray spectra for the angles that were accessible with the given setup (from 0º to 30º). Figure 2.11 shows the results of these measurements. As we can see, we find an isotropic X-ray emission in this range of angles.

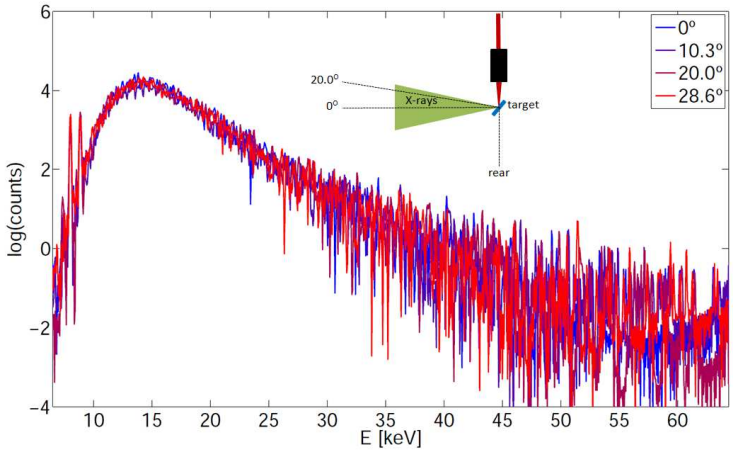

Figure 2.11: Angular X-ray emission from a Cu target. A Fourier Transform Filter (FFT) has been applied to avoid the fast oscillations produced by spurious noise. The pulse energy was 0.65 mJ. The spectrometer was place at 55 cm from the source in the laser reflection direction. A 1 cm methacrylate filter was put to avoid pile-up. The accumulation time was 5 minutes. The low temperature of hot electrons leads to a quasi isotropic Bremsstrahlung emission [50].

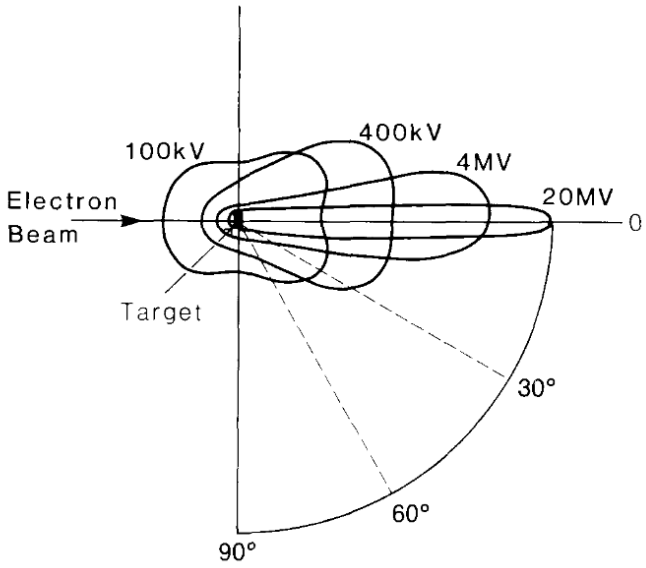

Figure 2.12: Schematic illustration of the spatial distribution of x-rays around a thin target. Image from [50].

It is interesting to mention that although the K_α and K_β emission is expected to be isotropic, for the Bremsstrahlung this is not so clear. The nature of the Bremsstrahlung emission -which is produced by the sudden loss of energy of accelerated electrons reinjected in the plasma bulk- and the fact that, as we will show later, the accelerated electrons are produced exclusively in the reflection direction of the laser radiation may introduce some sort of anisotropy in the emission. In fact for conventional X-ray tubes, this anisotropy is well established depending on the energy of the electrons (see Fig. 2.12). While for few keV electrons the emission is quasi-isotropic, for higher energies the emission is predominant in the forward direction. In our case, the hot electron temperature is 33.5 keV, so it reasonable to have an isotropic Bremsstrahlung distribution.

2.3.4 X-ray emission as a function of the laser polarization

It has been shown [51] that the electron emission depends on the laser polarization. Electrons are emitted in two lobules in the direction of the laser polarization. Thus, it is expected that the bremmstrahlung emission is directional too. However, we have measured the spectrum for different laser polarizations (see Fig. 2.13) and we did not observe any significant difference. Again, we attribute this isotropy to the low electron temperature (both T_{cold} and T_{hot}) [50].

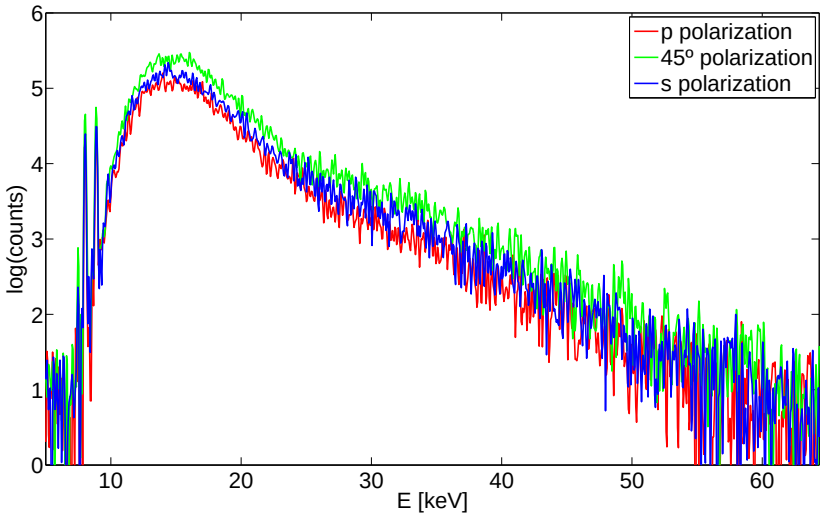

Figure 2.13: X-ray emission from a Cu target for different laser polarizations. The experimental conditions were the same than in figure 2.11. We noticed that the X-ray emission does not depend on the laser polarization. We observed a slightly increment in the count rate for 45º polarization, but we attribute this change to a small variations in the experimental conditions. Although the number of counts increases, the shape of the spectrum is the same than for the rest of polarizations.

2.3.5 Electron emission

Although we have checked that the X-ray emission seems to be isotropic, previous studies show that the electron emission is strongly directional [51]. To check this fact, we have observed the dose deposited by electrons in a Gafchromic film. These films consists in a plastic sheet with an active layer that darken where it receives radiation. Thus, the advantage of the use of Gafchromic films is that they do not need a post-exposition process. Besides, they can work under light conditions, since their reaction to visible light is very low.

In particular, we have use the Gafchromic EBT2 model. This type of films present a high spatial resolution and can register a dose between 1 to 10 Gy. Its composition is showed in Fig. 2.14.

The dose registered in the Gafchromic film is related to its optical density, defined as:

$$OD = \log_{10} \frac{I_0}{I} \tag{2.4}$$

where I is the light intensity that has passed through the exposed film when scanned and I_0 is the light intensity that has passed through the film before the exposition. The relation between the dose and the optical density can be written as:

$$\text{Dose} = \text{p}_0\text{OD} + \text{p}_1\text{OD}^{\text{p}_2} \tag{2.5}$$

where p_0, p_1 and p_2 are parameters to be calibrated. Thus, to measure the dose, the film only has to be scanned with a calibrated scanner. However, the determination of these parameter is not trivial in the case of our source since we have a mixture of X-rays and electrons in ultrashort bunches. The dosimetry of the new generation of laser-based radiation sources is an open issue and will be further discussed in Chap. 4. For this experiment, we used Gafchromic films just to have a picture of the emission direction and divergence of the accelerated electrons. To perform this experiment, a stack of three Gafchromic films was placed at 5 cm of the source in the laser reflection direction (see Fig. 2.15) and were exposed during 50 minutes. We must notice that the dose that was deposited in the film is mostly induced by the electrons. In normal conditions, a Gafchromic film placed next to the the source darkened in 5 minutes. But if a methacrylate filter of 2 mm was placed in front of it stopping electrons, the exposure time increased up to 3 hours just to overcome the low dose threshold of the film. In consequence, we can dismiss the contribution of the X-rays. Figure 2.16 shows the optical density in arbitrary units of the stack of films after exposition.

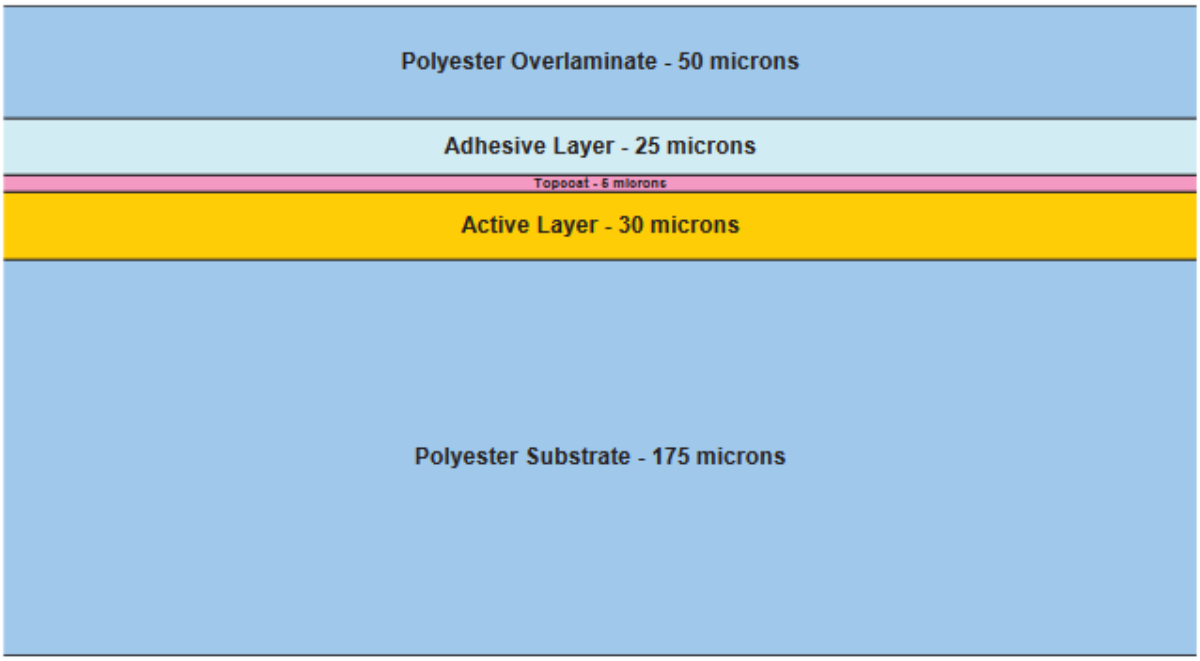

Figure 2.14: Composition of EBT2 Gafchromic film.

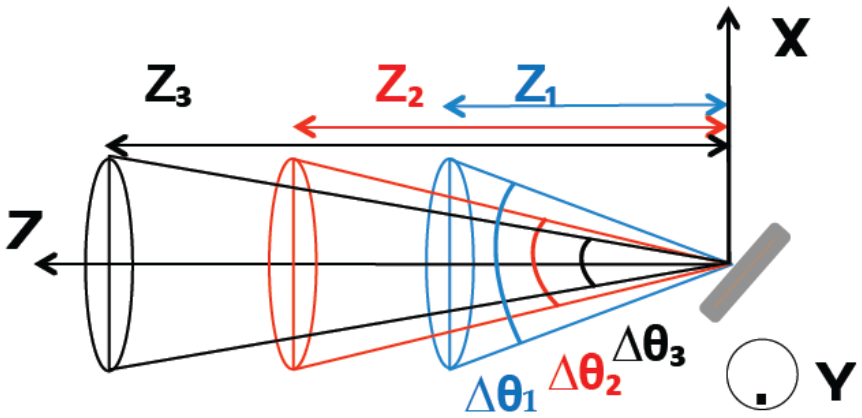

Figure 2.15: Setup for the electron emission characterization. A stack of three gafchromic films was placed at $z_1 = 5\,\text{cm}$ from the source in the laser reflection direction.

FLUKA simulations performed by M. Huault has showed that the necessary electron energy to reach the first film is 60 keV due to the air attenuation, while these particles needs an energy of 175 keV to reach the second film. To reach the last film, it would be necessary an energy of 250 keV. Taking into account that the estimated Maxwell-Boltzman distribution of hot electrons has a temperature of around 30 keV, is plausible to observe a minimum mark in the second layer and no presence of radiation in the third one. Table 2.1 summarizes the divergence of the electron beam in each layer and the minimum energy of the electron in that beam.

Layer	**X divergence $\Delta\theta_x/2$**	**Y divergence $\Delta\theta_y/2$**	**E_{min}**
1	38.0º	33.3º	60 keV
2	22.3º	15.5º	175 keV
3	-	-	250 keV

Table 2.1: Divergence and minimum energy of the electron beam in each layer of the Gafchromic stack

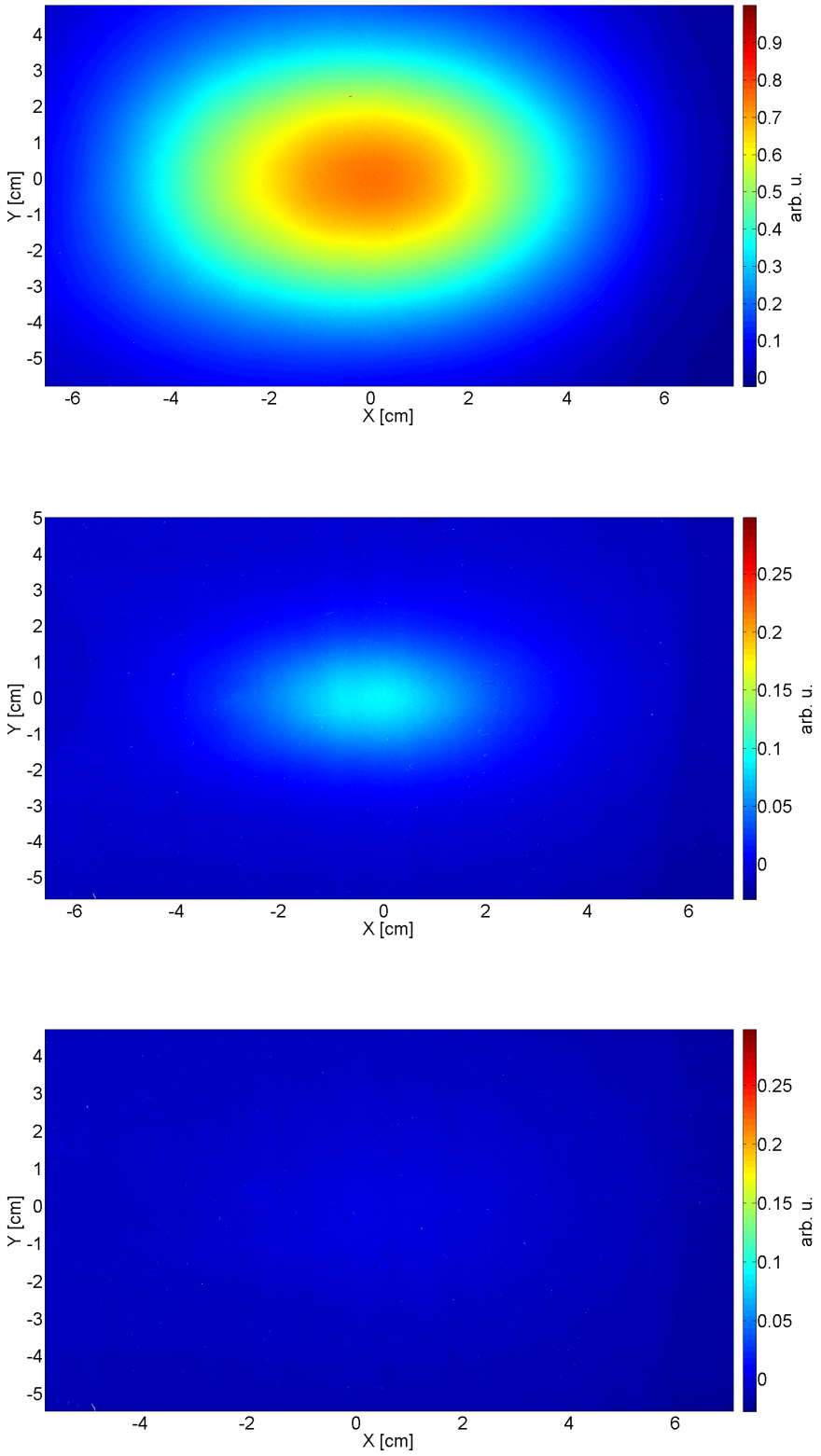

Figure 2.16: Dose deposition in a stack of three Gafchromic EBT2 films placed at 5 cm from the source in the laser reflection direction.

2.4 Liquid target

So far, different laser-based sources have been proposed but mostly relying on solid targets, and in the direction of achieving challenging performances rather than robustness and user-friendliness [1, 2]. For example, as we have seen previously, nowadays one can find relatively simple setups capable to produce ultrashort bunches of X-rays and electrons using moderate laser intensities in the range of 10^{16}-$10^{17}\,\mathrm{Wcm}^{-2}$ [1, 2, 19, 20, 52–56].

However, the use of solid targets for laser driven X-ray production presents several difficulties. Once the laser interacts with the target, this is heavily damage being necessary to move it to find a fresh area for the following laser shot. This limits considerably the reproducibility of the X-ray radiation generated because one cannot ensure the same experimental conditions after the target movement. Also the live time, defined as the time of recording events or total time of acquisition, of the possible experiments is reduced by the required target replacement and subsequent realignment. According to this, we can say that sources based on solid targets have severe limitations for many applications, like biomedical studies, being necessary a new generation of sources robust enough to permit systematic measurements and focused on an exquisite control over the radiation characteristics.

With the intention to offer a solution for the above described problems, we have studied the generation of laser-based soft X-rays from a liquid jet curtain [57–61] at atmospheric pressure conditions. Avoiding vacuum results particularly important when working with biological samples and cheapens the final cost of the source. The used setup maintains stable the density profile of the liquid shot to shot, allowing a stable X-ray generation without the need of moving and replacing the target. Furthermore, similarly to solid target where the X-rays the emission can be tuned using different materials, for liquids targets this tunability is obtained by solving different salts. For this experiment, we have used KCl and KBr, in an adequate solvent.

The liquid jet curtain used as target was generated by a dye circulator connected to a nozzle (Sirah lasertechnik). This kind of circulators are normally used to provide the active medium for CW lasers. However for X-ray production we used rather than the solution of a laser dye in a organic solvent, e.g., ethylene glycol, a mixture of water, glycerin and potassium chloride (KCl) or potassium bromide (KBr). In principle, according to the manufacturer, it is possible to use different salts with different concentrations, just keeping a similar density in the solution than the ethylene glycol ($1.1132\,\mathrm{g/cm^3}$). Otherwise, the liquid jet become unstable and the nozzle and the circulator can get damage. We achieved that with a mixture of 65% of glycerol and 35% of water in weight [62]. Although the solubility of KCl in water is $34.2\,\mathrm{g}/100\,\mathrm{g}$ we used just $25\,\mathrm{g}/100\,\mathrm{g}$ for precaution. For KBr we just used $28.6\,\mathrm{g}/100\,\mathrm{g}$ being the solubility in water 67.8g/100g. The circulator was operating at a stagnation pressure of 7 bars although it was possible to obtain a stable jet without flickering and/or air bubbles

for a wide range of pressures. The dimensions of the jet were $\sim 65\,\mu$m thickness times 4 mm in the widest part (see Fig. 2.17). As we observe in this picture, the jet is not flat in the edges of the liquid column. Thus, to measure the thickness we have observed the jet with a magnification system and approaching two needles from both sides until they both touched the jet. Then, we measured the distance between the two needles (Fig. 2.18).

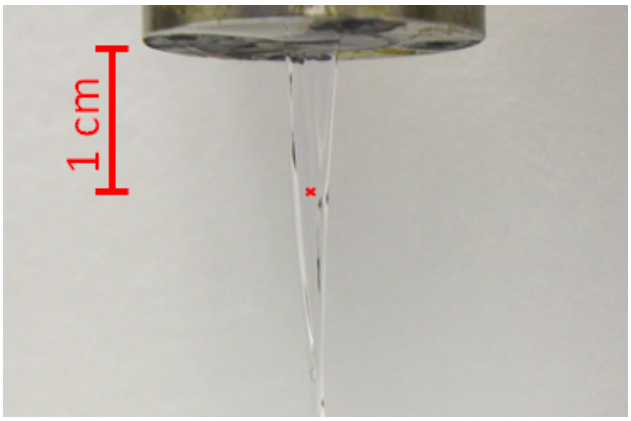

Figure 2.17: Liquid jet. Dimensions: 4 mm wide $\times \sim 65\,\mu$m thick $\times$ 5 mm long. The laser is shot at 1 cm of the jet, as the cross indicates

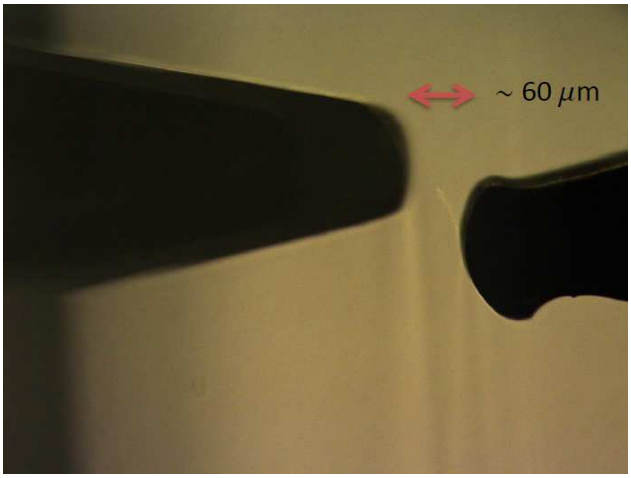

Figure 2.18: Liquid jet thickness measurement by approaching two needles until they touch the jet.

2.4.1 X-ray emission from liquid targets

Figure 2.19 shows a typical X-ray spectrum for a solution of glycerin, water and KBr, and glycerin, water and KCl. Both spectra are defined by a Bremsstrahlung emission extending to approximately 60 keV produced in the bulk of the liquid jet, and the characteristic X-

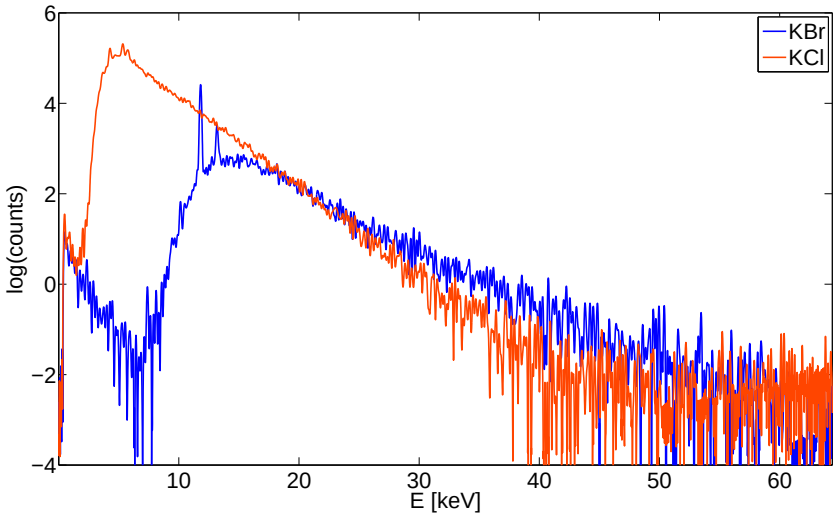

Figure 2.19: Typical X-ray spectrum for a solution of KBr or KCl. The experimental conditions were the same than figure 2.11, measured at 0º from the laser reflection direction.

ray emission of the solute. Concretely, we can see the K_α and K_β lines of Br at 11.9 keV and 13.3 keV. The X-ray emission of Cl and K couldn't be detected (K_α =2.6 keV and K_β =2.8 keV for Cl, and K_α =3.3 keV and K_β =3.6 keV for K) because they are heavely absorbed by air and filters [63]. The differences in the spectra for the low energy emission are due to a 1 cm methacrylate filter used for recording the spectrum of KBr.

To obtain the efficiency of the liquid target, we can compare the K_α energy conversion for KBr and for solid Cu targets. Figure 2.20 shows the spectra used for this comparison. Both measurements were taken in the same conditions: we placed the detector in the laser reflection direction at a distance of 55 cm from the target. We filtered the radiation with a 1 cm thickness methacrylate filter to avoid pile up.

To calculate correctly the efficiency of the source, it is necessary to take into account all the elements that reduce the X-ray photon flux prior it reaches the detector: 54 cm path in air, 1 cm thickness methacrylate filter, 12.5 μm thickness beryllium window that protect the detector, and the characteristic quantum efficiency of the detector. Figure 2.21 shows these data. The showed efficiency provided by Amptek company includes the transmission through the beryllium window. Taking all these factors into account, we obtain a total transmission of 1.2% for 8.0 keV and 14.6% for 11.9 keV.

According to Fig. 2.20 we registered 0.0009 counts/shot for the K_α line of Cu at 8.0 keV and 0.011 counts/shot for the K_α line of Br at 11.9 keV (taking into account the number of counts in 1 keV around the K_α peak, the total acquisition time - 300 seconds- and the repetition rate of the laser - 1 kHz -) . If we assume a 4π distribution for the K_α emission, and consider the effective area of the detector (25 mm^2), the total number of photons of these

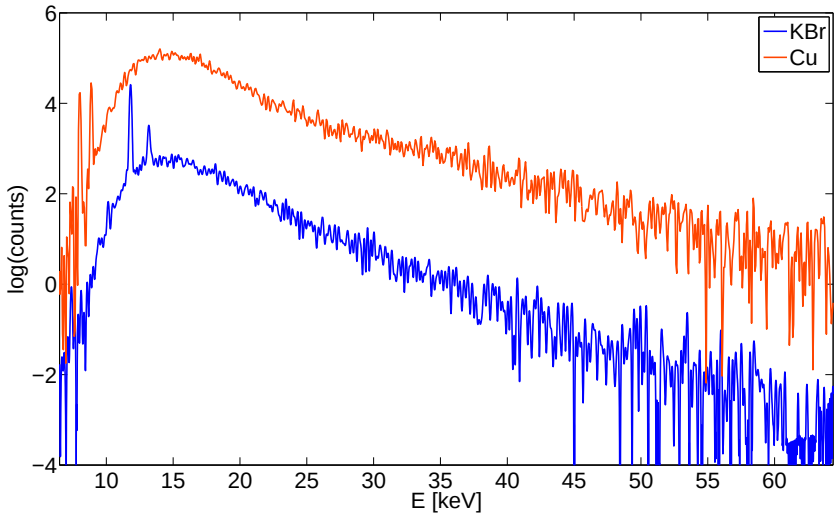

Figure 2.20: Spectra comparison between the emission of a liquid jet target -solution of KBr- and a solid Cu target.The experimental conditions were the same than figure 2.11.

energies emitted by the source will be:

$$N_{photons} = \frac{N_{counts}}{t_{acq.} RR} \frac{1}{T_{filters} \epsilon} \frac{4\pi r^2}{A} \tag{2.6}$$

where $t_{acq.}$ is the total acquisition time (around 300 s), RR the laser repetition rate (1 kHz), $T_{filters}$ the transmission of air and methacrylate, ϵ the efficiency of the detector for the selected K_α line, r is the distance to the detector (55 cm), and A the effective area of the detector (25 mm^2). The efficiency μ in the K_α production is

$$\mu = N_{photons} \frac{E_{K_\alpha}}{E_{laser}} \tag{2.7}$$

where E_{K_α} is the energy of the K_α and E_{pulse} is the pulse energy.

Taking this into account, we obtain 7.79×10^4 photons per pulse for Cu K_α line and 1.16×10^4 photons per pulse for Br K_α line. This is equivalent to an efficiency of 1.5×10^{-7} for solid Cu and 3.4×10^{-8} for the liquid solution of KBr.

In literature one can find several works reporting the efficiency of different targets in vacuum conditions (see Table 2.2). For example, for Cu targets (wire and tape) the efficiency range from 10^{-7} to 10^{-5} [64–67], while for molybdenum (Mo) disks one can obtain slightly higher efficiencies of the order of 10^{-5} [54, 56]. The efficiency of liquid sources in vacuum has been also subject of research. Tompkins *et al* measured an efficiency of 10^{-8} for 200 μm water jet with solved copper (II) nitrate ($Cu(NO_3)_2$) [60], while for a gallium (Ga) jet Zhavoronkov *et al* measured an efficiency of 10^{-6} [59]. The efficiency reported in this work for liquid target jets at atmospheric pressure conditions is slightly smaller (10^{-8}) than those

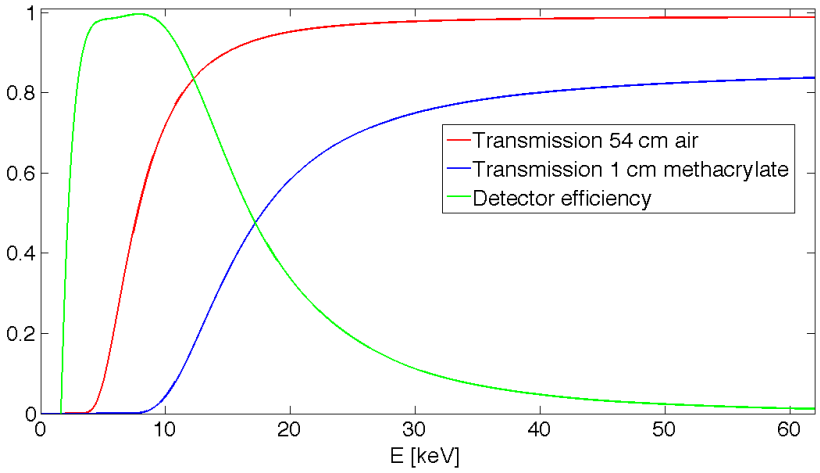

Figure 2.21: Absorption of X-ray in 54 cm of air, 1 cm of methacrylate and Amptek SDD-123 efficiency. This data must be taken into account to compute the total number of photons emitted by the source.

values. We attribute these differences to the absorption in air and the limitation imposed by filamentation for the minimum achievable focal spot. This leads to a lower intensity and, thus, to a lower electron temperature. Despite of this difference, the advantage of working at much simpler experimental conditions, i.e., at atmospheric pressure, and with a target that does not need replacement compensates by far this yield reduction.

Aiming to fully characterize the liquid curtain jet source, Fig. 2.22 shows the X-ray yield for KBr solution as a function of the laser pulse energy. Interestingly, although the emission yield decrease with the energy, even for low energies per pulse there is an appreciable X-ray generation. Below 0.1 mJ the X-ray emission was below our setup sensitivity.

Another interesting aspect to be determined is the directionality of the X-ray emission which cannot be properly measured for solid targets due to the limitations of the setup. Figure 2.23 shows the X-ray spectrum for different angles of emission being the emission completely isotropic. The slightly smaller yield production for the rear direction, i.e., in the direction of the laser incidence, is produced by the absorption of the target itself.

If we correct those spectra for KBr showed in Fig. 2.23 for the X-ray absorption in air and methacrylate, and for the efficiency of the detector, we can obtain the hot electron temperature T_{hot} by fitting the most energetic part of the spectrum (see Fig. 2.24). The obtained temperature $T_{hot} = 24.2\,keV$ is in agreement with an isotropic Bremsstrahlung distribution [50]. For T_{cold}, the Bremsstrahlung emission generated by the cold electrons and the K_α and K_β emission are superimposed. Thus, it is not possible to obtain a reliable fitting of the data.

According to the obtained T_{hot}, we can discard Brunel absorption as the main laser-

Target	Vacuum conditions	Efficiency	Reference
Cu (wire and tape)	Yes	10^{-7} to 10^{-5}	[64–67]
Mo disks	Yes	10^{-5}	[54, 56]
Water jet with $Cu(NO_3)_2$	Yes	10^{-8}	[60]
Ga jet	Yes	10^{-6}	[59]
Cu	No	10^{-7}	this work
KBr solution	No	10^{-8}	this work

Table 2.2: Summary of the K_α conversion efficiencies for different targets.

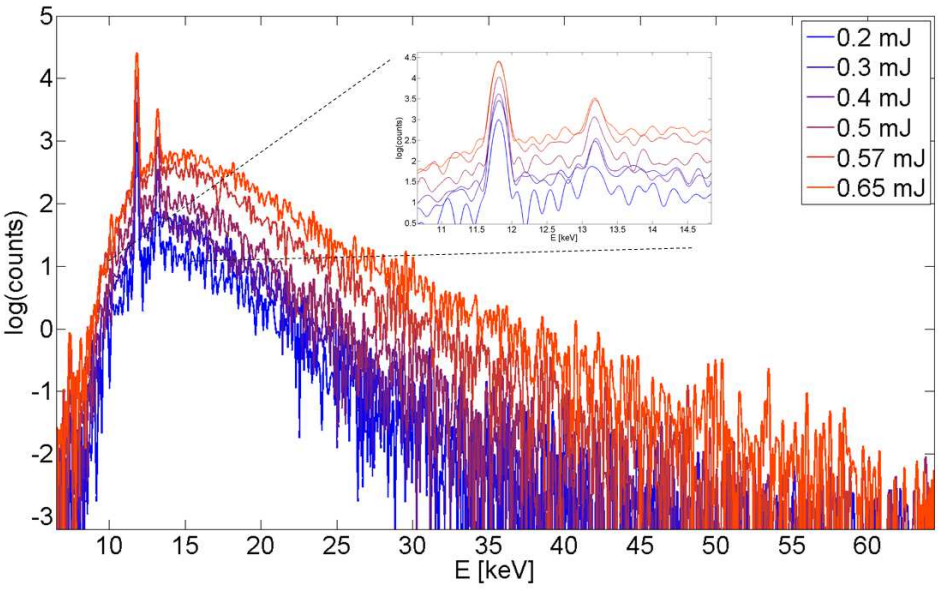

Figure 2.22: X-ray spectrum for a KBr solution liquid target as a function of the pulse energy.

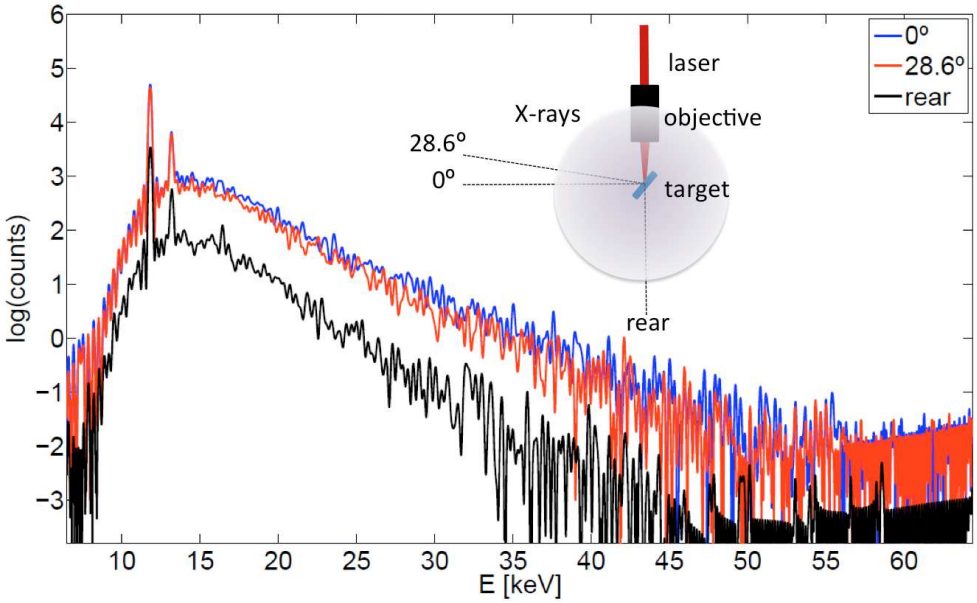

Figure 2.23: X-ray spectrum for a KBr solution liquid target as a function of the emission angle.

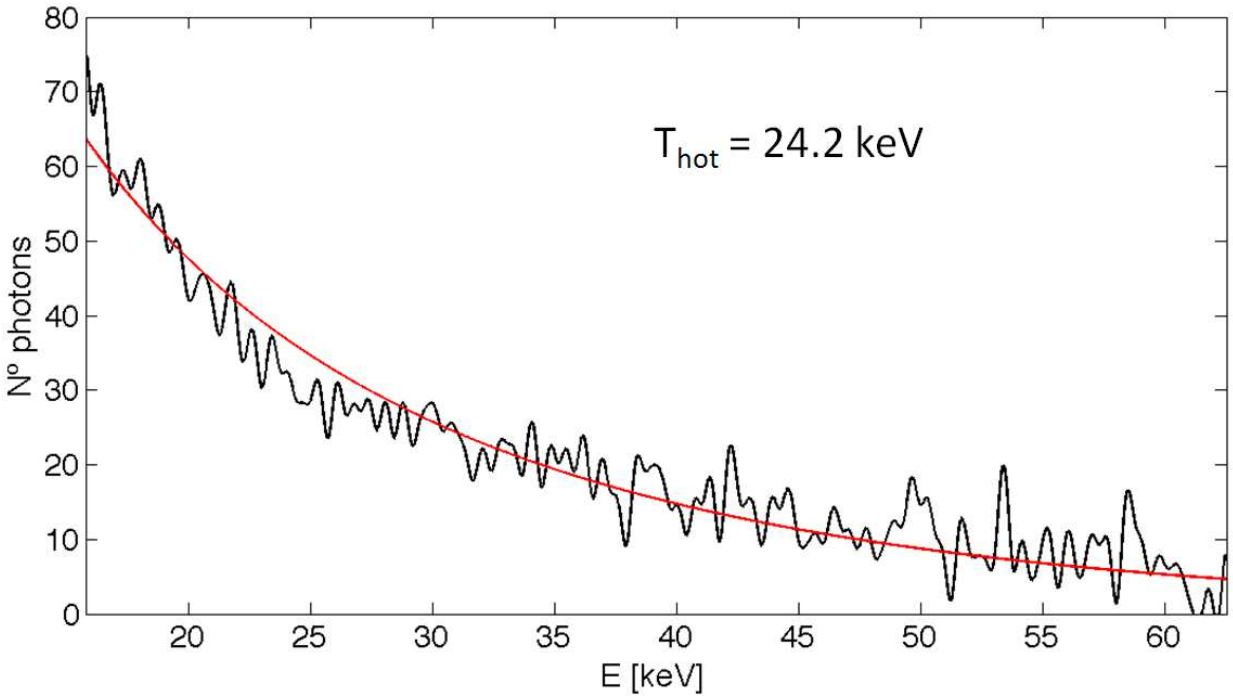

Figure 2.24: High energy X-ray spectrum for KBr fitted by Eq. 2.2

plasma interaction mechanism [68]. In this case, the energy of the expelled electrons is described by [24],

$$T_{hot} = 8 \left(\frac{I}{10^{16}} \lambda^2 \right)^{1/3} [keV] \tag{2.8}$$

where I is the laser intensity in Wcm^{-2} and λ the laser wavelength in μm. A $T_{hot} = 24.2\,keV$ corresponds to an intensity of the order of $10^{17}\,Wcm^{-2}$ which is beyond the capabilities of our experimental setup at atmospheric pressure conditions due to the limitation in the focal spot size imposed by filamentation.

For the resonance absorption mechanism the energy of the expelled electrons is slightly higher [25]

$$T_{hot} \approx 14 \left(\frac{I}{10^{16}} \lambda^2 \right)^{1/3} T_{cold}^{1/3} [keV]. \tag{2.9}$$

Assuming a cold electron temperature of $T_{cold} = 10\,keV$, the required intensity is in the order of $10^{15}\,Wcm^{-2}$, which corresponds to a focus diameter of $\sim 30\,\mu m$. This value is in between the measured diameter for low energies $1\,\mu m$ and the limitation imposed by filamentation in air $100\,\mu m$. This difference can be understood if we take into account that once the plasma is formed, i.e., just after the interaction of the early stages of the laser pulse with the target, the filamentation process takes place in a medium with a different diffraction index than air allowing a slightly tighter focusing. It is important to remark that so far we have only hints about the relevant acceleration mechanisms. For a reliable description, it is mandatory to run complex PIC (particle-in-cell) simulations of the interaction of a filamenting femtosecond laser with a target.

Figure 2.25 shows the electron emission direction. These measurements were carried out placing a EBT2 Gafchromic film at 5 cm from the target in the laser reflection direction. These kind of films are very insensitive to the X-ray emission in the range of energies of this work. Thus, we can assure that the signature in the film is exclusively produced by accelerated electrons. As expected, the electron emission is directional corresponding the position (x=0, y=0) to laser reflection direction.

We also tested the dependence of the X-ray emission in function of the laser polarization. As in the case of solid target, no difference was observed when polarization was changed (figure 2.26) due to the low energy of the accelerated electrons, which leads to an isotropic X-ray emission.

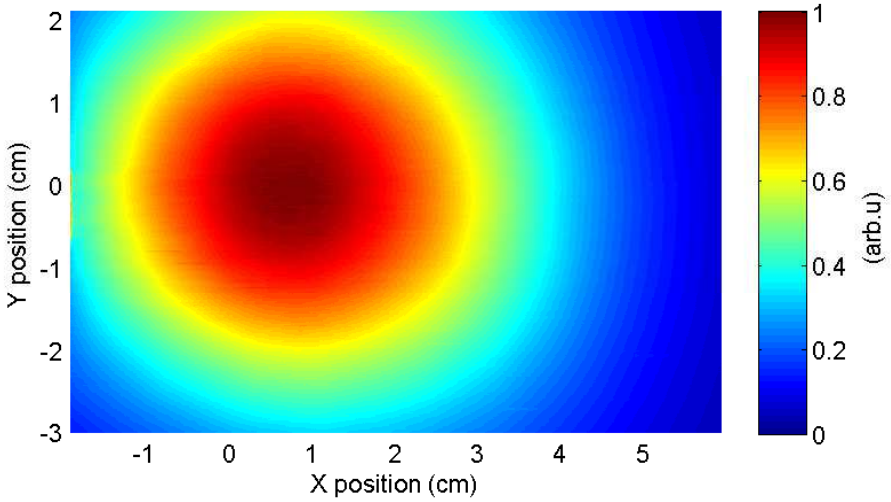

Figure 2.25: Dose profile in arbitrary units registered in a Gafchromic film for liquid KBr target.

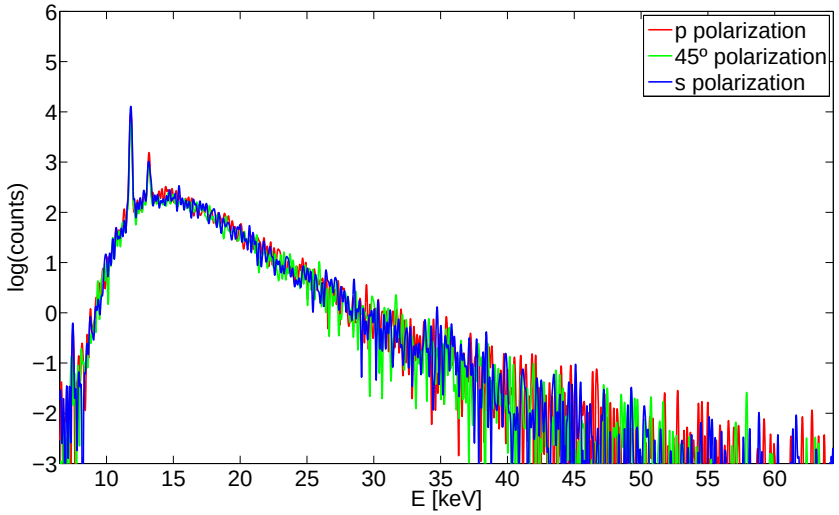

Figure 2.26: X-ray spectrum for a KBr solution liquid target with different laser polarizations. The spectra were measured at 55 cm from the source in the laser reflection direction. To avoid pile-up, a 1 mm methacrylate filter was placed before the detector. We observe the K_α and K_β lines of Br at 11.9 and 13.3 keV respectively. The peak at 7.48 keV corresponds to the K_α line of Fe and comes from the background setup.

2.4.2 X-ray emission by double pulses in liquid targets

The influence of a prepulse in laser-based X-ray generation has been proved in several experiments (see for example [69–77]). The observed enhancement is related with the increased coupling of the stronger second laser pulse with an expanding plasma -created by the first weaker pulse- from the target surface. This expansion takes place in the picosecond time scale, and leads to a volume increase producing a smoother density profile, and, hence, a reduction in the opacity of the plasma. Since the laser-X-ray conversion efficiency strongly depends of the density gradient of the expanding plasma, at a certain delay the laser-plasma coupling is maximized. If the delay between the laser pulses is too small, the density profile is still steep and there is not any difference in the laser-plasma coupling. On the other hand, if the delay is too long, the density drops rapidly and the second laser cannot efficiently heat the plasma electrons with the subsequent reduction in the X-ray emission.

To study this phenomenon we slightly modified the setup described above. The original laser radiation was divided using a beam splitter 20:80 into a prepulse and a main pulse (see Fig. 2.27). The delay between both pulses was controlled with a precision motorized delay stage with submicron precision. Once delayed one pulse with respect to the other, they were set collinear by a beam combiner, and focalized by the microscope objective into the same spot. The final energy of the pulses were approximately 0.24 mJ and 0.10 mJ.

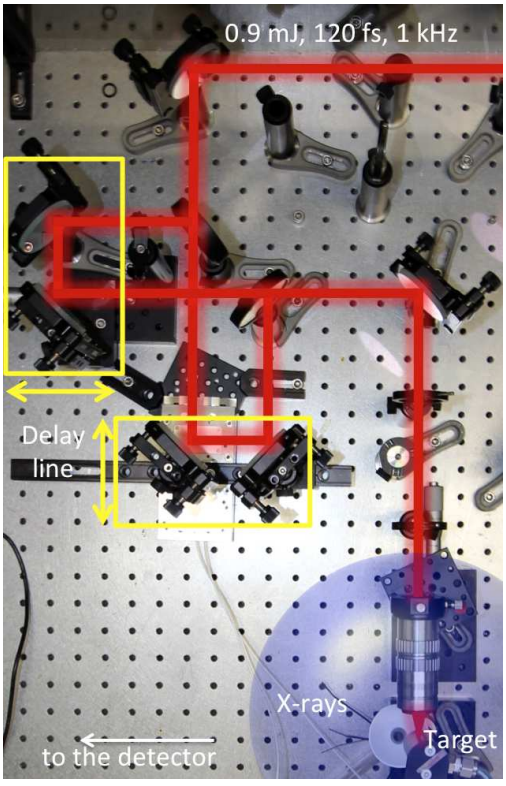

Figure 2.27: Experimental setup for double pulse experiments.

The different spectra were taken during 5 minutes, at a distance of 55 cm, in the direction of laser reflection, with a filter of 1 cm of methacrylate in front of the detector to avoid pile up. For each delay we recorded the spectrum generated by both pulses independently, and by the combined effect of them. At these low energies, the pre-pulse did not produce any measurable X-ray emission. Figure 2.28 shows the X-ray yield increment with respect to the situation when both pulses are temporally overlapping. We can clearly see for a delay of 3 ps an increment in the X-ray yield up to 50%. This result is compatible with the enhancement observed by Hatanaka *et al* in [73] although there are certain differences in the experimental setup. The pulses used in this work are considerable shorter, 120 fs versus 260 fs, and the laser was set parallel for both pulses (p-polarized) while in [73] the prepulse is s-polarized and the main pulse p-polarized.

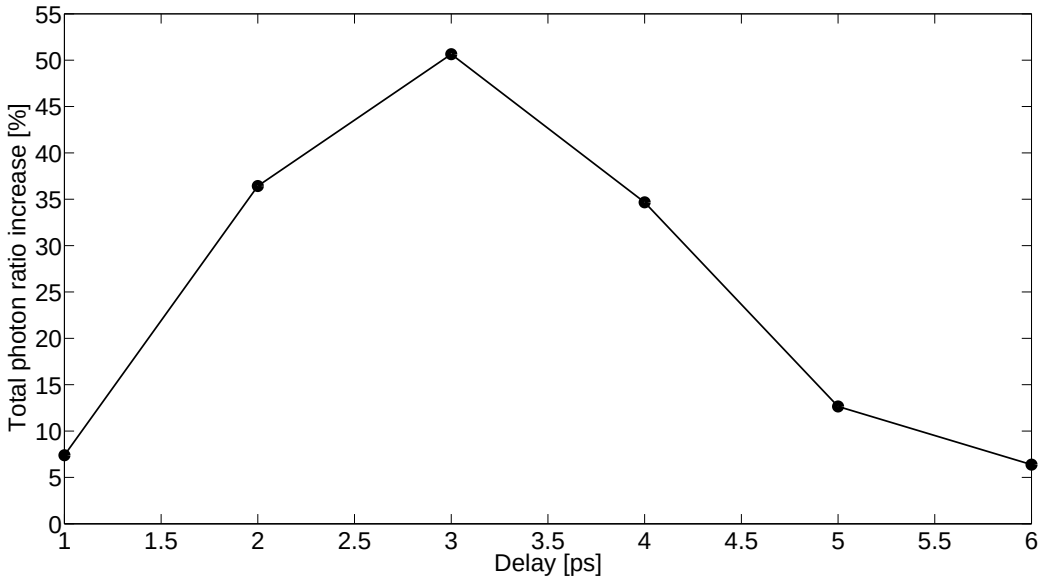

Figure 2.28: X-ray yield increment as a function of the delay between the pulses respect to the case where there is no prepulse.

2.5 Conclusions

In this work we have shown the potential of liquid jets as a target for X-ray production in air, characterizing their main properties experimentally. Although the X-ray emission efficiency of liquid and solid targets is comparable, the main advantage of liquids is their robustness and stability. Since there is no need to replace the target, as it is the case for solids, it is possible to carry out systematic and/or long-live measurements. These characteristics are mandatory if we want to explore the challenging possibilities that laser-based sources

of ionizing radiation may offer like for example new radiotherapy studies. These promising applications will be discussed in Chap. 4.

Chapter 3

Plasma mass spectrometry

3.1 Introduction

One of the most important features of the X-ray laser source presented in Chapter 2 is the temporal duration of the radiation pulse. While a conventional X-ray tube emits pulses in the range of microsencond, a laser driven X-ray source inherits the temporal characteristics of the laser pulse, with durations in the range of femtosecond or picoseconds [69, 78]. This peculiarity allows to reach high radiation fluxes and rises promising applications. We will discuss this in detail in Chapter 4.

Unfortunately, to measure a X-ray pulse in the range of femtoseconds is not a trivial issue. For longer pulses, in the picosecond scale, streak cameras are used. These devices transform the fast temporal information into spatial information. Figure 3.1 shows a typical streak camera. The incoming light pulses generate electrons in a photocatode. Then, electrons are dispersed with a time depending field and recorded in a 2D detector. Knowing the field that has been applied, one can extract the temporal information of the light pulses looking at the trace of the electrons. However, commercial X-ray streak cameras have a temporal resolution of approximately 0.5 ps [79], which is not adequate in our framework (we expect X-ray pulses of hundred of femtoseconds), and usually are quite expensive. To fix this issue, a proposal for a home-made X-ray streak camera is presented in this chapter. A modified version of our proposal was built to test the capabilities of the device and to perform plasma mass spectrometry of the filament generated by the laser. Here, we will present and discuss the results.

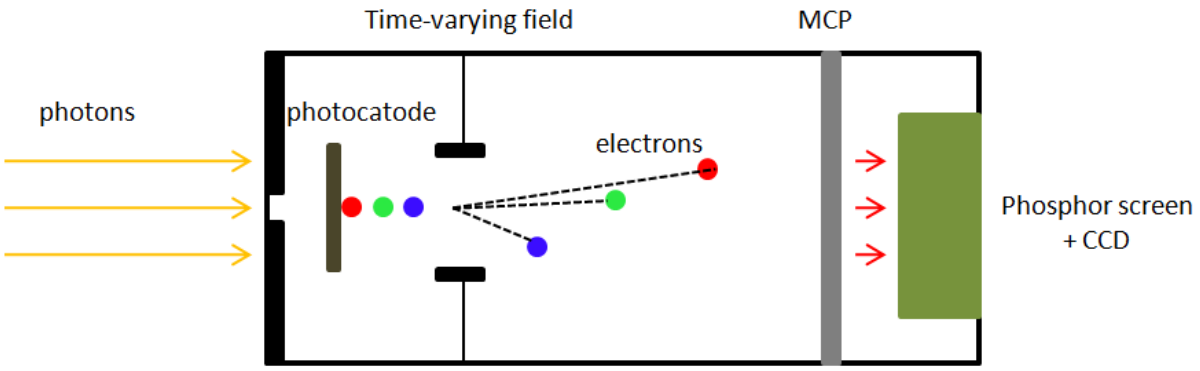

Figure 3.1: Example of a X-ray streak camera

3.2 Proposal for a X-ray streak camera

To measure the laser driven X-ray pulse of our source, we propose a streak camera based in the ionization of the air by the generated radiation (see Fig. 3.2).

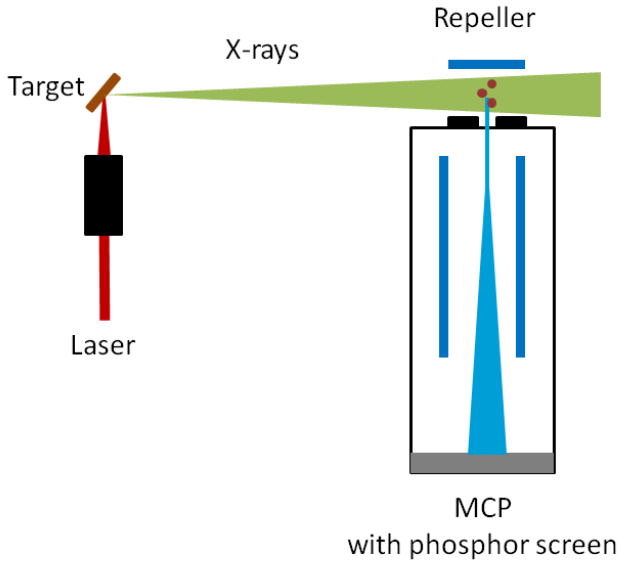

Figure 3.2: Proposal for a X-ray Streak Camera. The ions produced by the X-ray pulse are pushed into a vacuum tube where are deflected with a time-varying field. The trace collected in an MCP allows to infer the temporal information of the X-ray pulse

The setup contains a vacuum tube with a pinhole at the entrance, that allows a differential vacuum, and a repeller plate generating a field that points towards the pinhole. The radiation pulse ionizes the air between the pinhole and the repeller. Then, the plate pushes the ions

into the vacuum tube, where a time-varying field change the trajectory of the ions. A Micro Channel Plate (MCP) detector is placed at the end of the tube to detect the deflected ions. A MCP is a device that allows to detect particles or ionizing radiation working as an electron multiplier (see Fig. 3.3). It is composed of a panel of metallic channels in which a voltage is applied between the entrance and the end. When a particle or a high energetic photon hits the wall of the channel, an electron is emitted and is accelerated between the two voltages, hitting continuously the walls of the channel and generating a cascade of electron in consecutive impacts. Finally, a detector is put at the end of the channel to measure the total electronic signal.

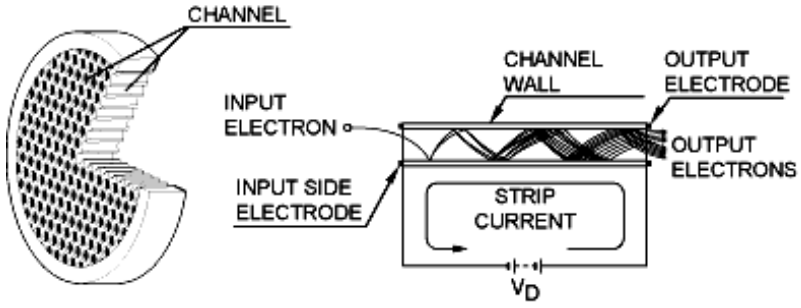

Figure 3.3: Scheme of a Micro Channel Plate (MCP). Image from [79]

Alternatively, a phosphor screen can be place to have a 2D image of the radiation impact in the MCP, as it is the case of our proposal for a streak camera. Usually, two panels in a V configuration (the so called chevron MCP, Fig. 3.4) can be used to increased the signal.

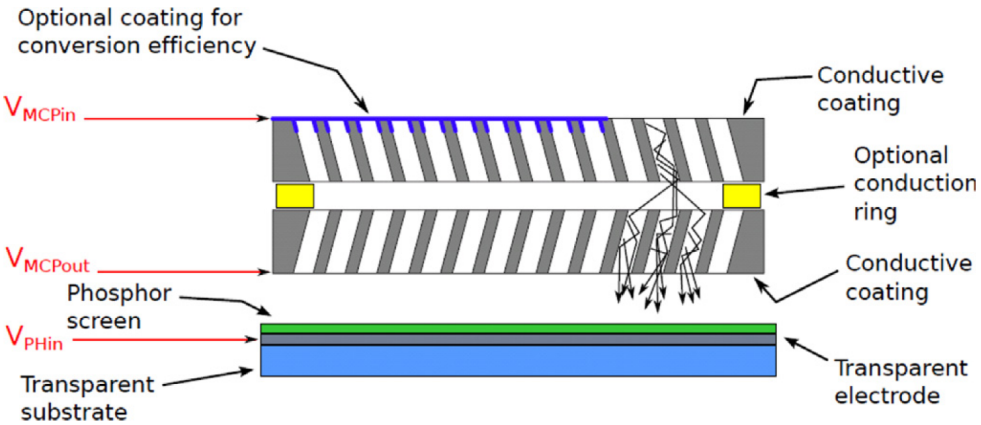

Figure 3.4: MCP in a chevron configuration. Two consecutive MPCs are place with a 90º tilt to increase the signal. Image from [80]

Instead of using a MCP with a phosphor screen and a capacitor with a time-varying field, other possiblility is to use MCP coupled with a high voltage switch to rise the voltage

difference in the MCP. In that case, the MCP only measure the signal when the high voltage switch is on. Although the rise time of this devices is in the order of nanosecond, a delay between the laser and the rise voltage could be applied, so a scan with different delays would allow to know the duration of the pulse.

One advantage of our proposal for a streak camera compared to a conventional one (Fig. 3.1) is that our camera could be used to study both X-ray and electron pulse. A camera like the one showed in Fig. 3.1 cannot be used for electrons because the entrance pinhole would be charged and it would repel the incoming electrons.

MCP must work in vacuum conditions, approximately at 10^{-5}m bar. Otherwise a discharge may take place between the two voltages and the detector will be damage. In consequence, to know if the proposed setup have the capability to measure the generated ions, we have to know if the presence of a pinhole allows to maintain the safety vacuum level of the MCP while allowing a clear ion signal. To answer this question, we built a modified version of the proposed streak camera that can be used as a Time of Flight detector. This simplified device was used to measure the dynamics of the plasma filament created by a ultraintense laser, as we will see in the following sections.

3.3 Time of flight detector

3.3.1 Introduction

As we stablished in Chap. 1, filamentacion is a non-linear phenomena linked with ultraintense lasers. The parameters of the plasma generated in this processs are fundamentally limited, e.g., density and temperature, by the characteristics of the laser propagation in the medium. Many different groups have devoted their efforts to study the process of filamentation itself and the possible applications of the plasma channel induced by the laser field (see for example [49, 81–85] and references therein). If we concentrate in the field of filamentation on atmospheric Sciences some of the on-going applications are the use of laser filaments to control lighting [86–89] and rainfalls [87, 90, 91], the guiding of high power microwaves using the ionisation channel created by the filament [92, 93], or the remote sensing of pollutants in air using molecular fluorescence and LIDAR (Laser Illuminated Detection And Ranging) [49, 94, 95]. It is important to recognise that for a successful implementation of such techniques it is required a complete understanding of the process of laser filamentation and, more important, of the subsequent plasma dynamics. Thus, questions like which species are formed inside the plasma channel, at what time after the formation of the filament new species are generated, or at what time after the pulse the plasma density becomes negligible and the species can move freely, need to be addressed to provide predictable and

reliable models not only of the filamentation process itself but also of plasmas at atmospheric pressure conditions. So far different groups have dealt with these problems mainly using spectroscopic techniques like Raman spectroscopy (see for example [96–98]) providing useful information about the process dynamics. However, these analysis rely on the correct identification of the fluorescence lines of the plasma which is usually a difficult and arduous task.

In this section we present a Time of Flight spectrometer (TOF) developed in our laboratory where the sample does not need to be isolated from the circumvent medium for the ionization process. Thus, we have obtained detailed information on the different ion species generated within the plasma, in the inner core as well as the surroundings, at atmospheric pressure conditions, as well as on the relaxation mechanisms related with the plasma dynamics like for example molecular recombination. The results proved the validity of the system to measure formed ions, proving that it can be used to develop a X-ray streak camera. The TOF can also have applications to study the plasma filament dynamics and so to understand the X-ray generation process itself.

3.3.2 Experimental setup

Figure 3.5 shows our TOF spectrometer.

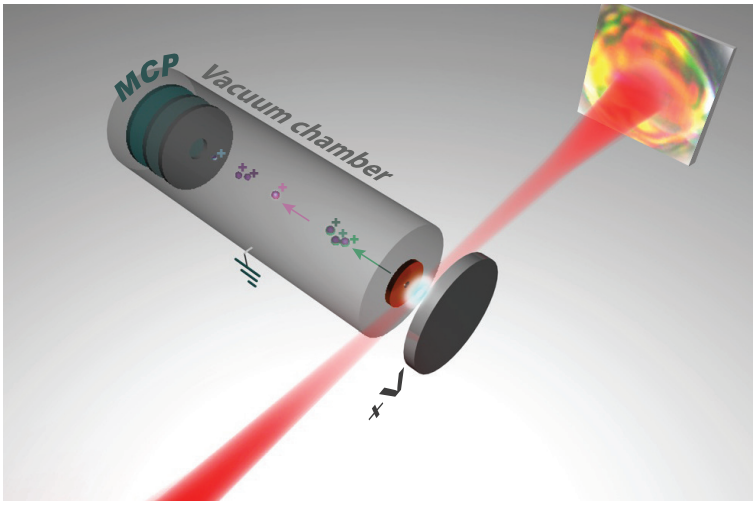

Figure 3.5: A pulsed intense laser is focused in air or in a gas cell generating a filament. The produced ions are repelled by a positive voltage plate and driven towards the TOF spectrometer. A pinhole with a diameter of 30 μm aligned with the plasma allows the ions to enter the high-vacuum chamber of the TOF spectrometer and reach a microchannel plate (MCP) detector after a free flight of 30 cm. The distance from the filament to the pinhole is 2 mm, and from the filament to the repeller plate 10 mm. A supercontinuum is also generated in the filament.

A repeller plate pushed the generated ions to the MCP detector in a vacuum tube. A pinhole of 30 μm and thickness of around 10 μm was placed at the entrance of the tube dividing the ionization zone and the free fly zone of the spectrometer. This pinhole was small enough to allow a proper vacuum to work with the MCP (10^{-4} mbar), but big enough to allow the repelled ions to enter in the vacuum tube and to have a measurable signal, as we will see. The length of the tube was 30 cm. We focalized the laser at the entrance of the tube. The distance from the filament to the pinhole was 2 mm and from the filament to the repeller plate, 10 mm. Once the ions entered the spectrometer they travelled freely, i.e., there were no further acceleration stages, towards the MCP. To avoid a charge accumulation in the body of the TOF spectrometer, the outer structure had to be properly connected to ground. The signal from the MCP was collected and integrated in an oscilloscope triggered with the laser by a photodetector signal.

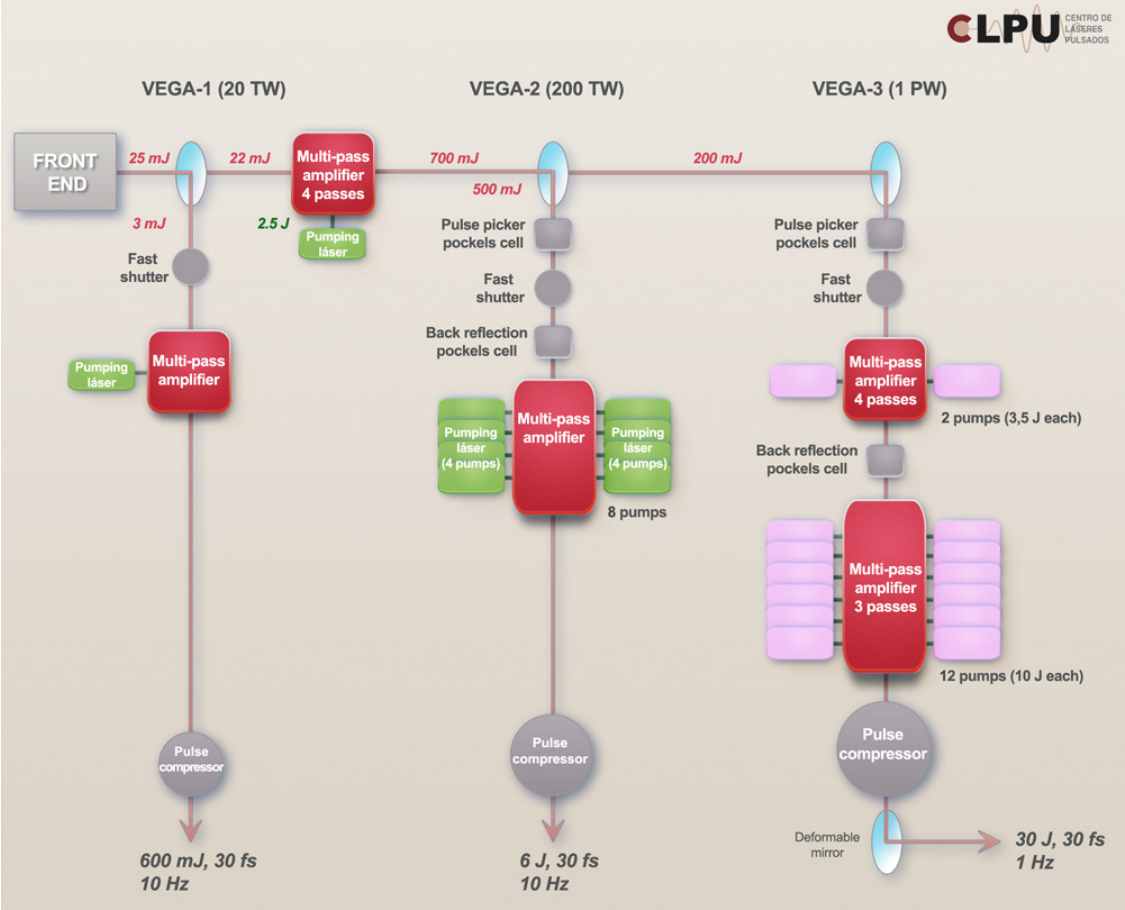

Figure 3.6: Structure of VEGA laser. The laser, developed by Amplitude Technologies, has three ouputs, named VEGA I (20 TW, 600 mJ, 30 fs, 800 nm, 10 Hz), VEGA II (200 TW, 6 J, 30 fs, 800 nm, 10 Hz) and VEGA III (1 PW, 30 mJ, 30 fs, 800 nm, 1 Hz).

To test our system, we have used VEGA laser (see Fig. 3.6). VEGA is the main laser

equipment of CLPU and it has been developed by Amplitude Technologies. It is a unique system that consists of three outputs, named VEGA I (20 TW, 600 mJ, 30 fs, 800 nm, 10 Hz), VEGA II (200 TW, 6 J, 30 fs, 800 nm, 10 Hz) and VEGA III (1 PW, 30 mJ, 30 fs, 800 nm, 1 Hz). In addition to be one of the few PW systems in the world, VEGA is unique because of its high repetition rate, its high contrast and the possibility of carrying out pump-probe experiments with the combination of its outputs.

For the experiments of this chapter, we used VEGA II as laser system. In particular, the system delivered pulses of 30 fs, 800 nm of central wavelength, 10 Hz of repetition rate and 30 mJ per pulse in order to work at atmospheric pressure conditions after compression, avoiding filamentation during the propagation of the pulse. The beam diameter of around 10 cm was focused by the combination of a spherical mirror and a plan-convex lens with focal lengths of 1 m and 20 cm respectively, resulting in an effective focal length of the whole system of 28 cm. With these conditions, a filament was created in the vicinity of the focal plane. The alignment of the laser filament with respect to the entrance of the TOF was carried out maximising the UV light detected by the MCP at time zero. The integration time for the experimental data shown in this work was approximately five minutes.

3.3.3 Experimental results

Figure 3.7 shows the ion spectrum when the filament was produced in air at atmospheric pressure. A Fast Fourier Transform (FFT) filter has been applied to remove the fast frequencies produced by spurious noise.

We can clearly observe three different contributions:

- A peak at time zero, attributed to the X-rays and UV generated in the plasma. This was used to align the filament with the pinhole
- A resolved ion structure for about 50 μs.
- An unresolved continuous of about 1 ms of duration.

To check that the resolved and unresolved structure correspond to an ion signal, we performed the following tests:

- We observed that the signal was sensitive to the voltage of the repeller, which means that it was produced by charged particles.
- We checked that the signal disappeared if the repeller voltage was inverted, which implies that the charged particles producing the signal were ions.

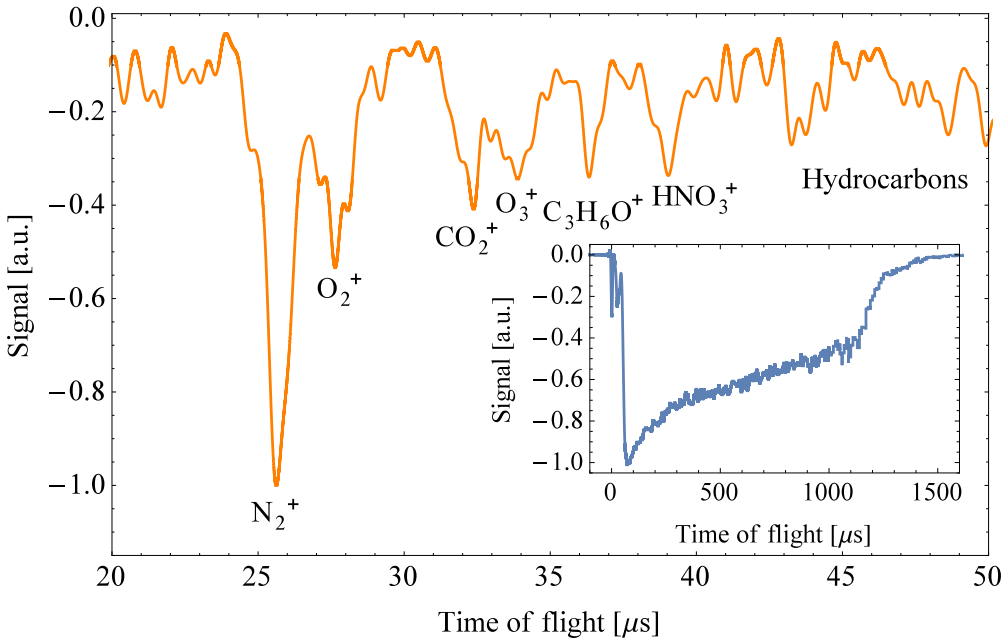

Figure 3.7: Time of flight spectrum of a laser filament in air at atmospheric pressure. The voltage of the repeller was set to V=1 kV.

If we focus in the first resolved part of the spectrum, we can assign the peaks to the different ions present in the plasma. Taking into account that air is mostly composed by N_2 (78% of N_2, 21% of O_2, 0.93% of Ar and 0.04% of CO_2), it is a plausible assumption to identify the largest peak to this molecule. Then, if we assume that ions feel an uniform field cause by the repeller, we can identify the mass of the ions that cause the other peaks using the following expression:

$$m_{ion} = m_{N_2} \left(\frac{t_{N_2}}{t_{ion}} \right)^2 \tag{3.1}$$

According to Eq. 3.1, we identify in Fig. 3.7 the different species produced during the ionization of air: N_2^+, O_2^+ and CO_2^+. But also we observe the appearance of new compounds like O_3^+ and HNO_3^+. The ions found at a time of flight of around 36 μs and 50 μs correspond to a mass of 57 amu and 101 amu respectively. These masses are typically assigned in mass spectrometry to a hydrocarbon chain and its photofragments. They are possibly produced by an unwanted contamination. The large peak at 36 μs can also be tentatively assigned to some traces of acetone, which was used to clean optics and the apparatus.

Let's focus now in the continuum structure from around 50 μs s to 1.2 ms (see Fig. 3.7 inset). The origin of this continuum is unclear. It could correspond to the ions that are accelerated towards the spectrometer simultaneously but with an initial kinetic energy distribution extremely large. Another possible origin could be the spectrum of ions that are

accelerated at very different times ones with respect to the others. In any case, we assume these ions must come from the ionization of air and not from the ablation of the metallic plate holding the pinhole. The reason is because we could not identify any metallic ions like for example Al^+ or Cu^+, and different pinholes (different materials) provided the same signal.

As we stated above and attending to Fig. 3.7 it is interesting to notice that during the relaxation path of the primary air molecules, new compounds like nitric acid (HNO_3) or ozone (O_3), energetically more stable than air compounds, are formed. The presence of these molecules indicates not only that in the energy reservoir a major ionization and photofragmentation is taking place but also a highly collisional environment. The final relaxation products of laser filamentation in air is attracting a huge interest lately by their role in the control of atmospheric processes using laser filaments. For example, the role of HNO_3 in induced snow formation by laser filamentation was recently acknowledge by the group of Prof. S.L. Chin (see for example [99]).

For a better undertanding of the origin of the ion signals, filamentation experiments in pure N_2 were carried out. For this purpose, we built a methacrylate cell that could be hold in front of the pinhole with orificies for the entrance and output of the laser and for the filling gas. We introduced gas and checked with a CO_2 detector that there was no oxygen in the cell, and so the other components of air apart from N_2 were removed. Figure 3.8 shows the result of this experiment. We can see the ion peaks corresponding to N_2^+ and N^+. Here we also observe the unresolved mass spectrum. Thus, it is plausible to think that ions in the resolved part of the espectra have the origin in the energy reservoir that surround the core of the filament which sustains its propagation (see [81]). The laser intensity reached in this reservoir is much lower than in the filament core but it is still sufficient to produce photoionization and photofragmentation of molecules. Another possible ionization mechanism is electron-impact ionization. In the first stages of the filament formation, electrons are heated up to a free-electron temperature of the order of 10^4-10^5 K being the thermal equilibrium reached in the order of tens of nanoseconds once the laser interaction has ceased. This relaxation is mediated by elastic and inelastic collisions that produce new ions in the surrounding molecules.

Another fact that must be discussed is the considerably large time of flights of the different ion (in the order of tens of microseconds) when compared with a conventional TOF of the same length (in the order of just few microseconds). To understand this fact, we plot the time of flight versus voltage applied in the repeller (see Fig. 3.9). Figure 3.9 inset shows the expected length for different initial velocities that the N_2 have depending on the applied voltage. In an ideal time of flight, we have

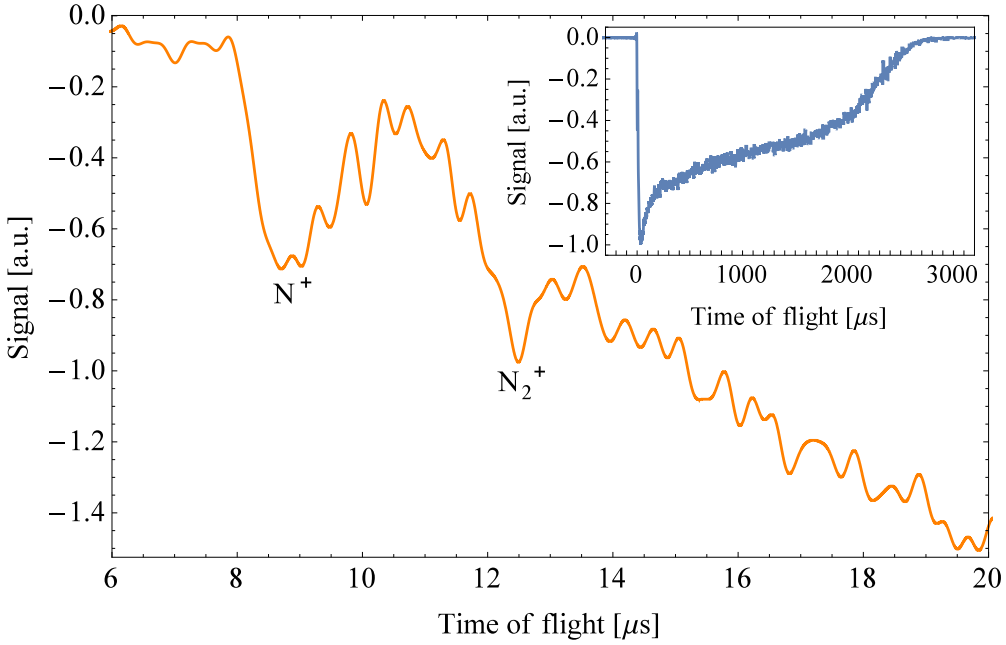

Figure 3.8: Time of flight spectrum of a laser filament in N_2 at atmospheric pressure. The voltage of the repeller was set to V=2.5 kV.

$$vt_{measured} = L \tag{3.2}$$

where v is the velocity of the ion, L is the length of the TOF and $t_{measured}$ is the time in which we observe the N_2 peak. However if there is dead time t_0 in which the ions are not accelerated, we have

$$vt_{measured} = vt_{real\,flight} + vt_0 = L + vt_0 \tag{3.3}$$

where $t_{real\,flight}$ is the time in which the ions are in fact travelling towards the MCP. This linear tendency is the situation that we observe in figure 3.9 inset. This indicates that there is some sort of mechanism that delays the particles in their trip to the detector. This dead time is given by the slope of the curve, which is around 8.5 μs.

We attribute this delay time to the multiple collisions that the generated ions suffer in the atmosphere just before the pinhole entrance to the spectrometer. To get a complete picture of the problem we also need to take into account that the filament core once the laser is gone, i.e., the plasma left behind, behaves like a dielectric material. Therefore, the plasma gets polarized by the voltage difference between the repeller plate and the grounded spectrometer, having as a consequence the cancellation of the electric field. Accordingly, the effective acceleration voltage is extremely low producing the large observed time of flights. It is true that the plasma expands, and consequently its density is reduced, but the time scale

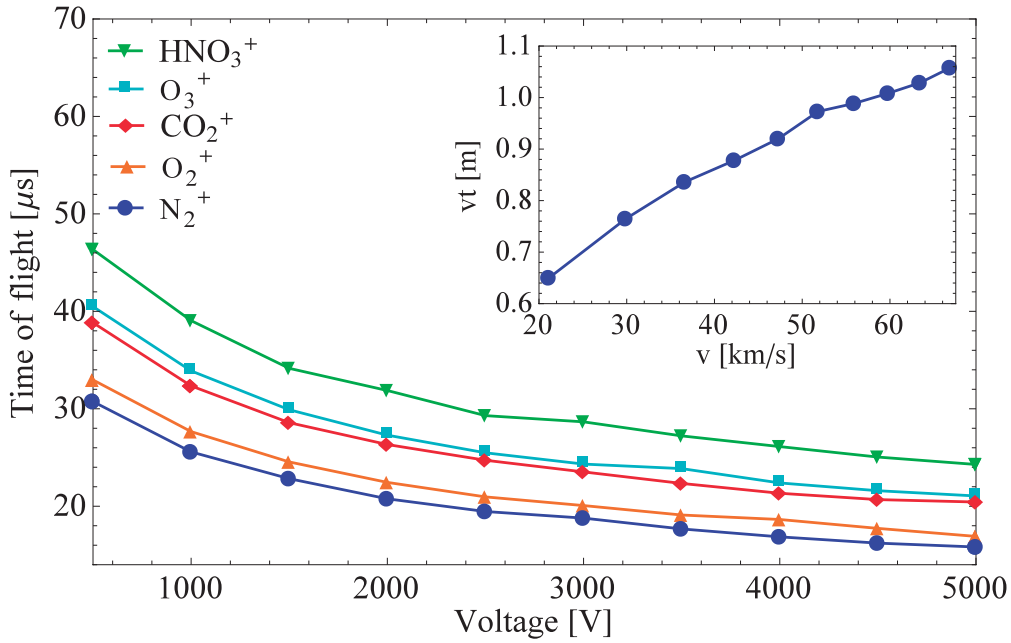

Figure 3.9: Main graph: time of flight versus voltage applied in the repeller for different species in experimental conditions similar to Fig. 3.7. Inset: expected distance travelled by N_2^+ molecules versus its expected velocity

of this process is much slower than the time of flight of the ions generated in the reservoir region.

This idea links directly with the origin of the unresolved ion signal seen in Fig. 3.7 and Fig. 3.8 insets. We attribute this unresolved part of the measurements to the ions generated in the filament core. Once the interaction ceases a plasma with an electron density in the order of $10^{16}\,\mathrm{cm}^{-3}$ is formed. Although plasmas with these electron densities are underdense, the electromagnetic forces between ions and electrons are sufficient to hold the species together preventing any significant leak towards the spectrometer. In fact, as it was discussed above, there is an effective charge separation in the plasma induced by the external acceleration voltage. Once the plasma expands, the density drops and thus the forces among the plasma species are reduced. The experimental data indicates that this process is gradual, producing a continuous leak of ions and therefore an unresolved ion signal.

Numerical simulations

To justify our conclusions, we simulated the behaviour of a plasma under the influence of an external electric field. This simulation was done with a one dimensional PIC (particle in cell, see for example [100]) code. The code and simulation were performed by J. I. Apiñaniz. We implemented a plasma with an electronic density of $10^{20}\,\mathrm{m}^{-3}$ in a square profile of $20\,\mu\mathrm{m}$ of width at t=0 in vacuum. The initial temperature was set to 1 eV and the applied external

field to -10^7 Vm^{-1}. These parameters and the external field represent an extreme situation that favors the charge separation in plasmas for a better visualization of the results. In laser-based filaments the density and the temperature are of the order of 10^{22} m^{-3} and 0.5 eV respectively [83, 101]. Nevertheless the choice of parameters does not affect the Physics that underlies this process. As PIC parameters we selected a time step of 50 fs, a spatial cell of 0.01 μm, and a macro particle size of 10^4 (real particles per computational particle). With these characteristics, the Debye length, that is, the effective length over which electrostatic potential disturbances are "screened out", in this plasma is 0.74 μm. On the other hand, the plasma frequency, i.e., that is, the oscillation frequency of the charge in the plasma, is $\sim 9{\cdot}10^{10}$ s^{-1}.

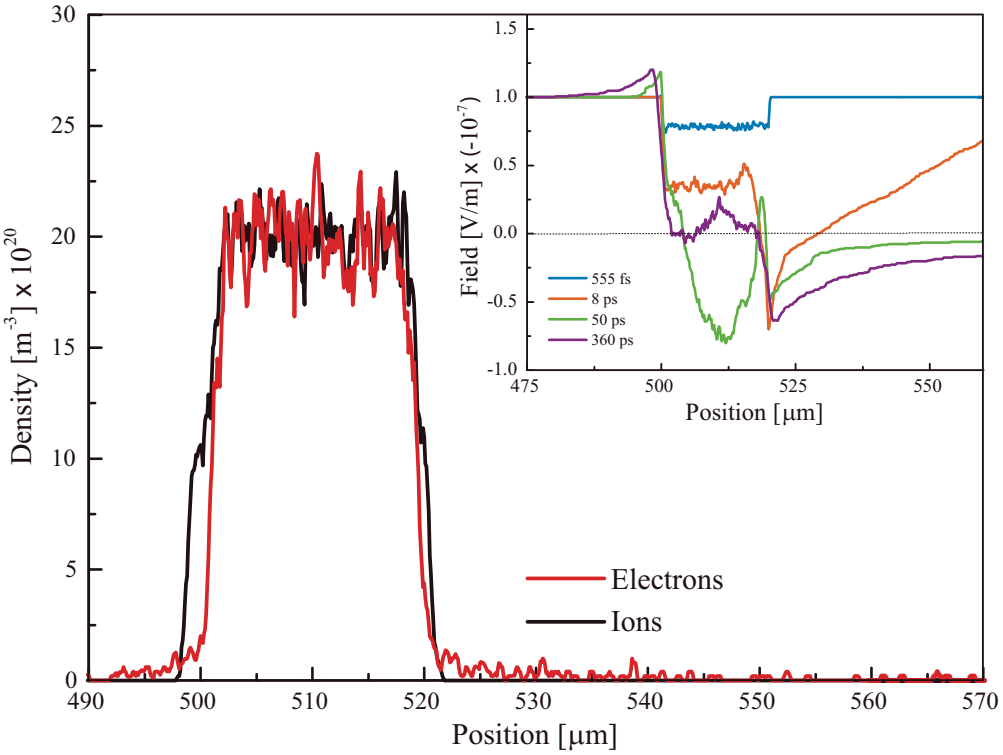

Figure 3.10: Main graph: ion and electron density at different times. Inset: total field, i.e., external applied field plus internal field generated by the plasma polarization, for different times of evolution. The parameters of the simulation were chosen for the sake of the argument: computational time, better visualization, etc. No relevant differences are expected with another set of parameters.

Figure 3.10 main graph shows the ion and electron density from 5.5 fs to 360 ps. We can clearly see an effective charge separation in the plasma (notice the separation of electrons and ions at the edges) producing its polarisation and consequently the cancellation of the external electric field. For a better understanding of this phenomenon the inset of Fig. 3.10

shows the total field, i.e., the sum of the external field plus the internal one created by the charge separation, as a function of the position for different evolution times. Even at the first stages of the evolution the plasma becomes quickly polarised under the influence of the external field. The total field inside the plasma oscillates around zero at the plasma frequency. It must be noticed that at the first stages of the dynamics, before the plasma gets polarised and there is an effective charge separation, some electrons can escape from the plasma deviating it slightly from the electrical neutrality. This non-neutrality of the plasma causes the field to be shielded not only inside its boundaries but also outside it, following the escape direction of the electrons (right side in Fig. 3.10). On the opposite side (from the plasma to the left in the graph) the field remains at its initial value of -10^7 Vm^{-1}. This behaviour stays constant until the ions expand significantly, reducing the density and thus increasing the Debye length to scales of the order of the experiment boundaries. Finally, it is interesting to pay attention to the sheaths at the edges of the plasma in Fig. 3.10. These sheaths give rise to field gradients at the plasma boundaries that extend for several tens of Debye lengths.

3.3.4 Conclusions

In conclusion, our TOF detector is able to study the ions generated by a laser filament by mass spectrometry techniques. Our original mass spectrometer design allowed us to distinguish the ions generated within the filament energy reservoir, characterized by a clear mass spectrum, and the ones coming from the filament core, characterized by a continuous one. The sensitivity of the device also is suitable for studying the photofragmentation taking place in the plasma and surroundings. Furthermore, analyzing the form and characteristics of the mass spectra for both components, we obtained valuable information about the plasma dynamics and relaxation channels. For example, final relaxation products with huge importance for filament based atmospheric applications like O_3 and HNO_3 have been clearly observed. In our opinion this work and the new developed apparatus pave the way for further studies on plasma dynamics and relaxation using mass spectrometry techniques. An example of a further development is the use of high voltage switch to pulse the repeller voltage at a controllable temporal delay with respect to the laser pulse. Operating in this way, it is possible to obtain snapshots at different moments of the relaxation dynamics obtaining a very valuable information of the involved relaxation processes.

These studies are important for the production of laser based X-rays at atmospheric pressure condition that we studied in Chap. 2 due to the importance of laser filamentation. Interaction of a filamenting femtosecond laser beam with a target in air is a very difficult theoretical problem and requires huge PIC simulations. To know in first place the dynamics of the plasma filament is necessary to simulate in the future the X-ray generation process.

3.4 Future work

With the studies of the plasma filament with the TOF detector we have proved the capability of our proposed streak camera to maintain the vacuum up to security levels of the MCP while allowing a measurable ion signal. The next step is to use the TOF setup to measure the ions produced by the pulse radiation of our source. For that, a proper shielding must be built, since the ionization of the walls of the TOF could lead to a false signal.

After that, a MCP with a phosphor screen must be tested, and a repeller plate with a time dependent field must be placed inside the tube. To build this field, we could use a high voltage switch like the one we proposed to obtain snapshots of the dynamics of the plasma filament.

3.4.1 Second order autocorrelator

Apart from an streak camera, the X-ray pulse duration could be measured by performing an autocorrelation. For that, the X-ray pulse must be divided with a split mirror that allows to control the delay between the two pulses and focalizes them in a gas jet (see Fig. 3.11). The first pulse ionizes the gas, while the second pulse increases the energy of the ionized electrons. To measure the energy of the electrons for different pulse delays allows to know when the pulses are overlapped, and so to know the duration of the X-ray pulse.

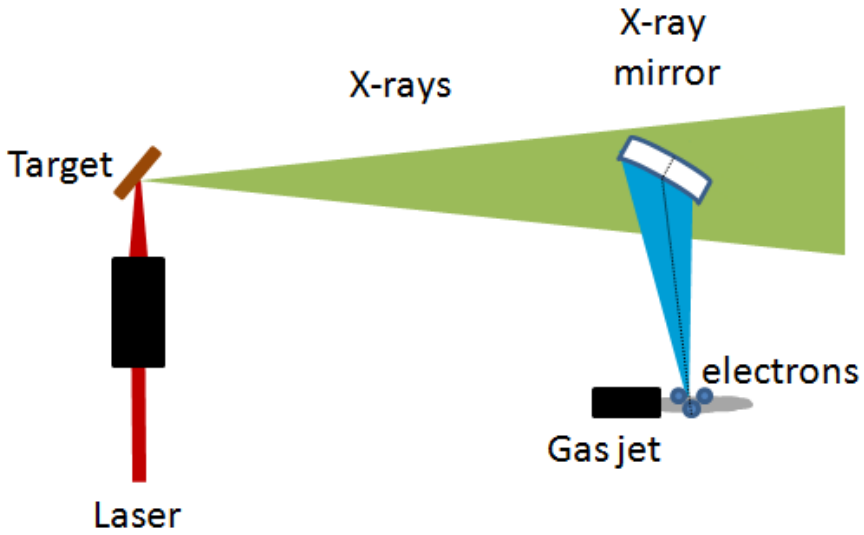

Figure 3.11: X-ray pulse autocorrelation experiment. A split mirror divides the X-ray pulse, allowing to control the delay between them by a mechanical adjustment between the two sections of the mirror. The X-ray pulse is focalized in a gas jet, where the atoms are ionized. The energy of the ionized electrons gives an autocorrelation trace that allows to determine the pulse duration.

To reflect X-rays, a toroidal diffraction mirror [102] or a Kirkpatrick-Baez mirror, based in the reflection of X-rays at grazing incidence on a curved metallic surface [103], can be used. This path will be hopefully explored in a near future.

Chapter 4

Applications

As we have seen in Chap. 2, the X-ray spectra of our source corresponds to the Bremsstrahlung produced by the spectrum of two Maxwell distributions of electrons, which have their origin in the direct acceleration by the laser and in the expansion of the plasma. We have estimated the hot electrons temperature around $T_{hot} \approx 30\,\mathrm{keV}$, leading to a X-ray spectrum that tends to $exp(-E/k_B T_{hot})$ for $E > k_B T_{hot}$. In addition, characteristic lines of the target are emitted. Also, and although we couldn't measured exactly this parameter, the pulse duration of our source inherits the temporal characteristics of the laser pulse, i.e., it is in the range of femtoseconds or picoseconds.

A laser driven x-ray source presents several peculiarities respect to conventional sources like X-ray tubes. In these tubes, typically electrons are accelerated up to a certain energy an then collide with a target, generating Bremsstrahlung radiation. In consequence, the maximum X-ray energy that can be obtained is the maximum energy that electrons gain in their acceleration. The characteristic lines of the target are also present in the emitted spectrum. Regarding the temporal duration, the X-ray pulse is usually in the range of microsencods.

X-rays tubes are a consolidated and relatively cheap technology that nowadays we can find in many fields. They are present in security scanners in airports or government buildings. Also, they are used in hospitals for medical treatment and diagnosis. And they are used in art for dating artworks.

In consequence, a laser driven x-ray source contrasts with conventional X-ray tubes in the following points:

- It emits accelerated electron besides X-ray radiation.
- While in X-ray tubes the target must be a heavy element to stop the electrons efficiently and thus to obtain high energy X-rays, with such laser intensities any kind of atom gets ionized. In consequence, in a laser based X-ray source any material can be used

as a target. The broad range of targets that can be used allows to select the proper X-ray spectrum for a particular application, and even to change it easily.

- The radiation pulse inherits the temporal characteristic of the laser pulse, so we have an ultrashort radiation pulse (femtosecond/picosecond range), and hence, we have at our disposal sources with high ultrabright instantaneous fluxes that may be capable to induce non-linear processes.

In this chapter, we take into account all this singularities and explore the potential applications of laser driven X-ray sources. We take advantage of the dual electron/X-ray radiation pulse to prove the benefits of using laser driven X-ray sources for X-ray fluorescence analysis in artworks. Also, we use the versatility of selecting the X-ray spectrum to propose a X-ray polarimetry for calibration of astronomical measurement devices. Finally, we discuss how the ultrashort duration of the radiation pulse can be used to calibrate detectors for the new generation of laser-driven radiation sources and how these sources may open unexpected new treatments and studies in radiotherapy.

4.1 X-ray fluorescence (XRF)

4.1.1 Introduction

X-ray fluorescence (XRF) is a well established technique that provides valuable information about the presence of chemical elements in a sample (see for example [104–106] and references therein). When the sample is irradiated with X-rays (or electrons), inner electrons of the atoms are excited. Once the produced vacancies in the electronic configuration are occupied by other electrons of higher energies, the atoms emit characteristic X-rays which are a fingerprint of each element. Nowadays, the importance of XRF is beyond doubt. For example, when applied to paintings, this technique reveals the elemental composition of the pigments used by the artist helping the art restorers to prevent the degradation of the colors as well as to answer questions related with authenticity and provenance. However the interpretation of the XRF data is not always straightforward. X-ray emission from the instrument itself and/or the surroundings of the artwork under analysis, e.g., the holder, can induce misinterpretation. Another important factor that must be taken into account is the penetration depth of the X-rays. For example, considering that oil paintings have as a basis a drying oil, e.g., poppy seed oil or safflower oil, with densities lower than $1\,\mathrm{gcm}^{-3}$, a material like PMMA with a density of $1.18\,\mathrm{gcm}^{-3}$ can be used to determine an upper limit for the X-ray penetration. According to [63] 10 keV X-rays are attenuated up to 90 % in 0.6 cm of PMMA, while for 100 keV this thickness is of around 12 cm. Thus, one must be

aware when analysing paintings with this technique that the obtained X-ray fluorescence is produced not only on the superficial paint layer, but also on those layers behind the visible one.

This difficulty can be overcome if electrons are used as excitation source. Due to the strong energy loss of electrons when they travel through any material, even air, only those with the higher kinetic energy are capable to reach the sample. For example to pass through 5 cm of air, electrons with a kinetic energy of 60 keV or higher are needed [107]. If we assume as an extreme case that electrons of 60 keV excite the sample, according to [107] the CSDA (continuous slowing down approximation) range for PMMA is $0.006\,\mathrm{gcm}^{-2}$. As the density of PMMA is $\rho = 1.18\,g/cm^3$, the electrons penetrate up to CSDA$/\rho = 50\,\mu$m in the material. Thus, electrons only interacts with the most external layer.

In this chapter we describe the use of a laser-based X-rays and electrons source for XRF analysis. The obtained results allow us to study not only several layers of pigment simultaneously using X-rays as in a conventional XRF technique, but also due to the limited penetration depth of electrons we can study just the surface of the artwork. In the following, we will first briefly describe our setup for XRF studies with X-rays and electrons. Then we will present the X-ray fluorescence of different pigments obtained by exciting them with our source. We will discuss the experimental data underlying the differences between both excitation sources. Finally, we complete this section with a brief summary and outlook.

4.1.2 Experimental setup

To carry out the XRF experiments, comparing the results with excitation of the sample with X-rays or with electrons, we need to separate the accelerated electrons and the X-rays. For this purpose, we built the setup that is shown in figure 4.1. The laser and the focalization system were the same that in Chap. 2, i.e, a Ti:Saphire system of 800 nm central wavelength, 120 fs pulse duration, 1 kHz repetition rate and an energy up to 0.9 mJ was focalized with a microscope objective of numerical aperture NA = 0.42 in a Cu target, achieving a measured focal spot at low intensity of the order of 1.5 μm in the horizontal and 1.2 μm in the vertical direction. As usual, for high energy conditions the focal spot will be considerable larger due to filamentation. If we consider the image of the plasma filament as a upper limit of the spot size, we found that the maximum size was of the order of 100 μm, leading to a minimum intensity of $\sim 1{\cdot}10^{14}\,\mathrm{Wcm}^{-2}$.

We placed a lead sheet with an orifice to reduce the divergence of the radiation beam. After this sheet we placed two magnets that deflect electrons. This deflection was checked with a Gafchromic film (EBT2). If we place the sample in position 1 (figure 4.2) we can analyse the XRF produced by electrons, while if we place the sample in position 2 (figure 4.2), we can analyse the XRF produced by X-rays. For X-rays the distance between the

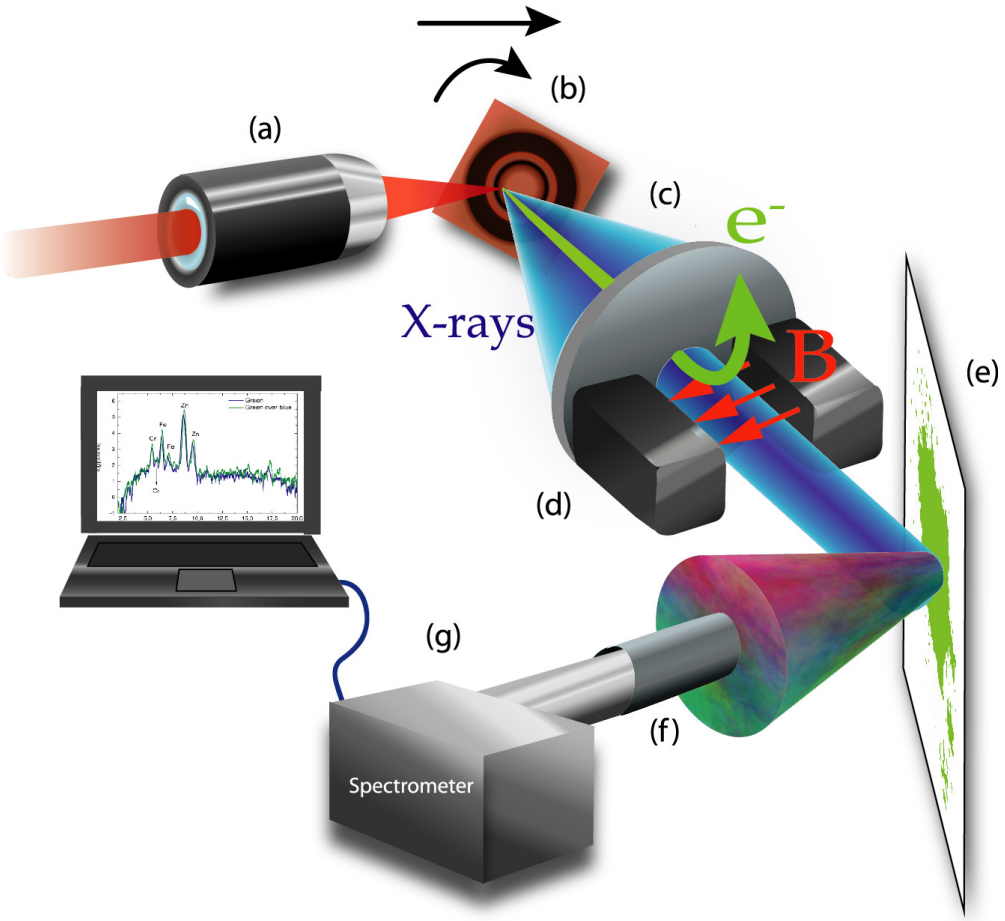

Figure 4.1: Experimental setup for XRF experiments with a X-ray laser-based source: (a) microscope objective (b) copper target (c) collimator (d) magnets (e) sample (f) collimator (g) spectrometer.

copper target and the pigments was 8 cm, and between the pigments and the detector, 5 cm.

For electrons, the distance between the pigments and the detector was 12 cm and a commercial collimator was used to avoid the noise. In the case of excitation with X-rays, the distance between the sample and the detector was 5 cm, and a custom collimator of lead was placed. In this case, the area seen by the detector is larger than in the case of electrons due to the fact that XRF signal was lower. These collimators allowed us to avoid the background radiation produced by the collisions between the electrons and the setup.

For a proof of principle experiment, we used two oil pigments (Marie's brand): emerald green (usual composition Cu(CH3COO)2·3Cu(AsO2)) and cerulean blue (CoO·nSnO2) [108]. We placed these pigments over watercolour paper in four different samples: green or blue solely, green over blue, and blue over green (see Fig. 4.3).

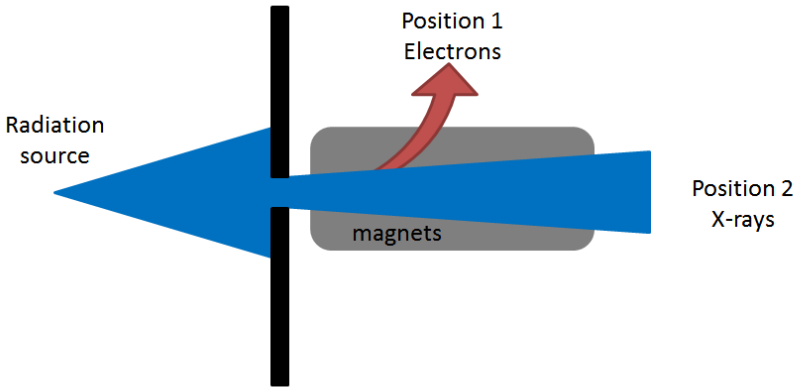

Figure 4.2: Detail of the experimental setup for XRF experiments with a X-ray laser-based source. A collimator is used to reduce the divergence of the radiation beam. Magnets are placed to deflect electrons and to have a clean electron or X-ray beam.

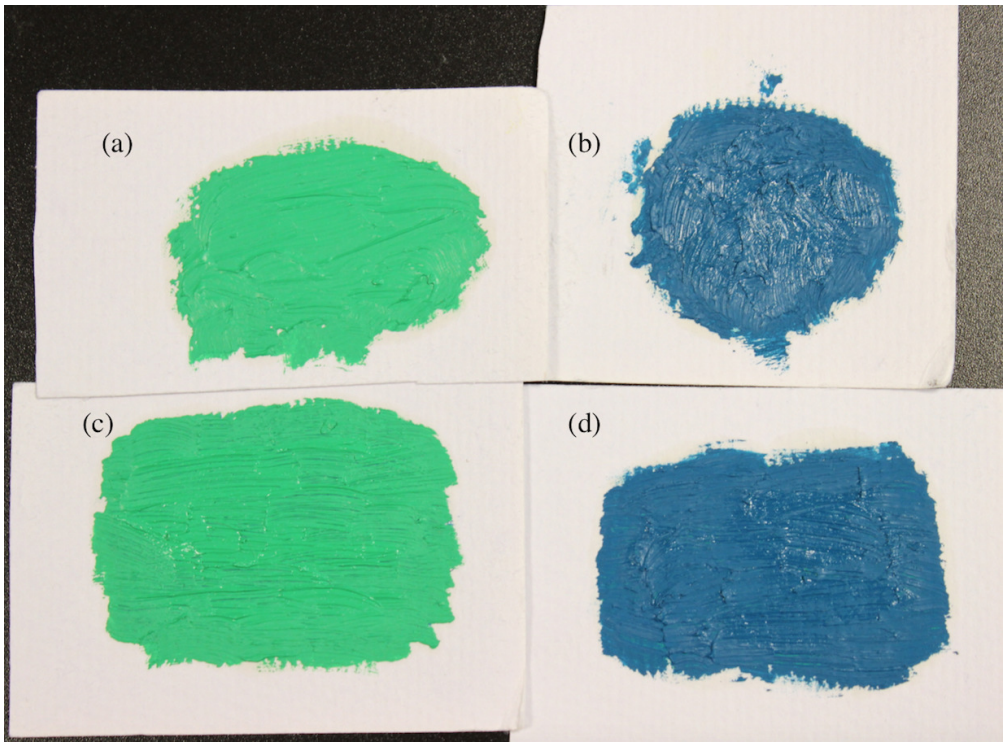

Figure 4.3: Samples used for the measurements of XRF. We used as pigments emerald green and cerulean blue over watercolour paper: (a) solely green, (b) solely blue, (c) green over blue and (d) blue over green.

Reference spectra of the pigments

First we obtained a reference spectrum without samples in order to calibrate the background produced by the X-ray fluorescence of the materials of the setup. This spectrum is shown in Figure 4.4. Here, we identified the K_α and K_β emissions of the following elements: Cr 5.4 keV and 5.9 keV, Fe 6.4 keV and 7.1 keV, Ni 7.5 keV and 8.3 keV, and Cu 8.0 keV and 8.9 keV [109]. These are typical materials in the fabrication of the optomechanics. At 2.7 keV we can see the emission lines of Ar in air (natural abundance 0.934 %). Argon is the only element in air with emission lines that are energetic enough to be observed in our detector (lower limit of 1 keV). Since this peak is present with the same magnitude for all the samples, we have normalized all spectra to it.

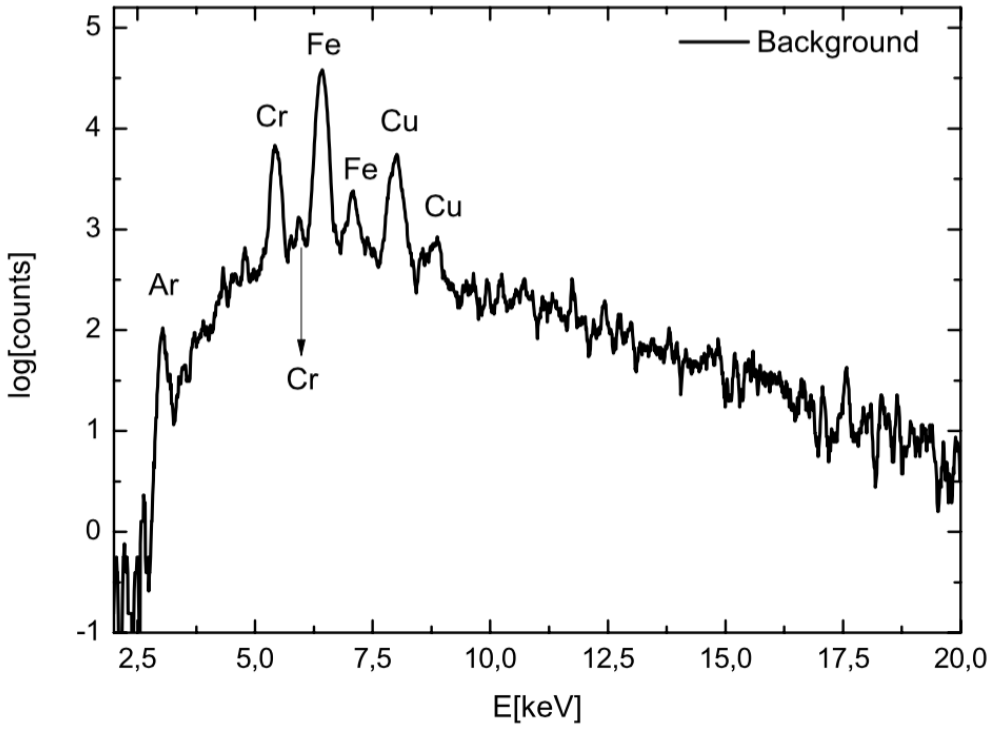

Figure 4.4: Background spectrum. We observed peaks coming from the fluorescence of the material of the optomechanics, from the copper target and from the ionization of air (Ar).

Figure 4.5 shows the XRF spectra of the oil pigments solely and the watercolour paper when we exposed them directly to the source, i.e., the samples were excited with X-rays and with electrons simultaneously. We can observe how the samples produce characteristic peaks apart from the peaks coming from the background. In particular, we observe peaks at 3.7 keV and 4.0 keV in the case of blue pigment and the watercolour paper, which we assign to the K_α and K_β lines of Ca. Our hypothesis is that Ca is present in the form of calcium carbonate ($CaCO_3$). This compound is normally used in the pigment industry as

a whitening agent. However, these peaks are not present in the case of the green pigment although we used the same watercolour paper. Our hypothesis is that green pigment has a strong absorption at these energies, suppressing the X-ray fluorescence of this energy coming from the paper. For the blue pigment, the presence of the peaks could be explained either because the pigment does not absorb these energies or the calcium carbonate is also part of the pigment composition.

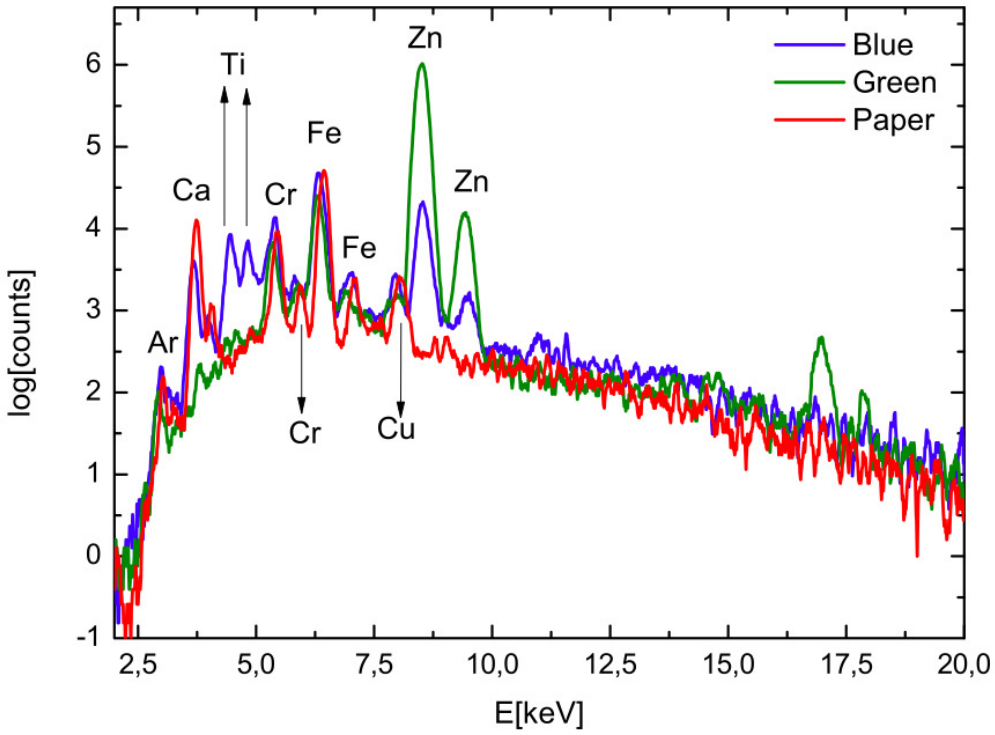

Figure 4.5: Reference X-ray fluorescence spectrum for the blue and green pigments and for the watercolour paper. It has been measured exposing the sample to the direct radiation beam. We observe the presence of Ca, Zn and Ti, which are commonly used as whitening agents. The presence of these elements allow us to identify each pigment.

For the blue pigment, we observe characteristic peaks at 4.5 keV and 4.9 keV. These peaks correspond to the K_α and K_β lines of Ti. Titanium is normally used in the pigment industry in the form of titanium dioxide (TiO_2). This compound is usually known as titanium white, and it is used for whitening. The titanium dioxide was introduce for artistic purposes in 1921. In oil, it dries to a spongy film, so usually is blended with other white pigments [110]. In fact, at 8.5 keV and 9.5 keV the K_α and K_β lines of Zn are visible in the case of blue and green pigments. The green concentration is significantly higher than for the blue. Zinc is normally presents as zinc oxide (ZnO) and is usually known as zinc white.

Finally, for the green pigment, we observe peaks at 17 keV and 17.9 keV. However no

reasonable element assignment could be made. Thus, it is plausible to attribute these signals to pile-up events of the Zn lines.

According to the chemical composition of the pigments, it was expected to find the emission of Co and Cu for the blue and green colors, respectively. However, the K_α emission of Co lies at 6.9 keV which is close to the much more intense background K_α line of Fe located at 7.1 keV (see figure 4.4). We have the same problem for the Cu. There is a strong background emission from the setup and the target itself, hiding probably the Cu emission of the pigment. It is also possible that the amount of these elements necessary to generate the color is tiny, being therefore below our detection limit. Alternatively, it is plausible that the color was generated adding organic pigments like, for example, indigo $C_{16}H_{10}N_2O_2$ whose X-ray emissions lie below 1 keV and are normally not detected by XRF techniques.

Green over blue sample analysis

Once we had the calibration of the background and the characteristic peaks of the pigments, we measured the XRF spectra of our samples with X-rays and electrons independently. The acquisition time for the different measurements was around 15 minutes for X-rays, and 25 minutes for electrons.

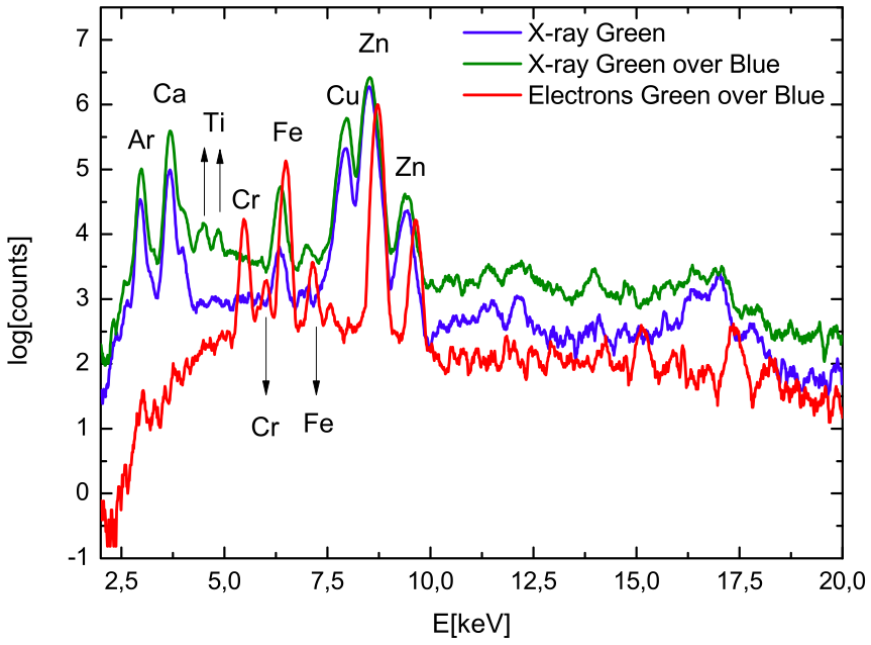

Figure 4.6: X-ray fluorescence spectrum for the green pigment when excited by X-rays, and for the composed sample green over blue when excited by X-rays and electrons. The X-rays reveal the Ti characteristic peaks of the underneath blue layer, but the electrons only show the green superficial layer.

Figure 4.6 shows the results obtained for a green layer of paint over a blue one (see Fig. 4.3, sample (c)). As reference, we show the green pigment when excited by X-rays. Although X-ray measurements are normalized to the Ar signal as discussed above, for the electron measurements this is not possible. The area seen by the collimator in the case of electrons is so small that the signal produced by Ar is too small. Also we have to take into account the different excitation yields of Ar for X-rays and electrons.

Let focus on Ti lines at 4.5 keV and 4.9 keV. This element is present in the cerulean blue but not in the emerald green pigment (see Fig. 4.5). Here we can see how these peaks are present when we irradiated the green over blue sample with X-rays, but they are absent in the case of only green paint. This means that X-rays can penetrate in the sample ($\sim$600 μm penetration for 10 keV) and produce fluorescence not only from the upper paint layer but also from the lower one. Thus, the signal from the different layers overlap and complicate the pigment identification. This difficulty can be solved if electrons are used as excitation source as shown in figure 4.6. In this case only the superficial layer is excited (the penetration is $\sim$ 50 μm for 60 keV electrons). The Ti peaks that the blue layer would produce are missing in this case.

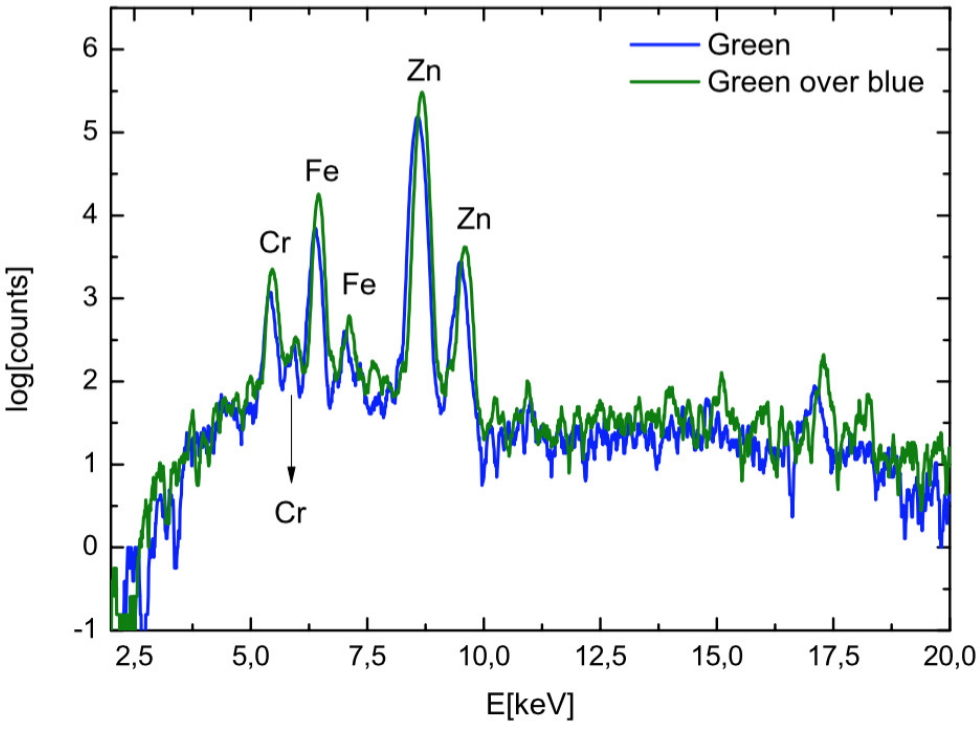

Figure 4.7: X-ray fluorescence spectrum of the green pigment and the composed sample green over blue when excited by electrons.

As it can be seen, the Ca peaks are present in the case of only green painting in figure 4.6 but not in 4.5. This is because the collimator of the detector in the case of X-rays excitation

setup collects a large area and see signal coming from the watercolour paper. The same argument applies to the large Cu peak at 8.0 and 8.9 keV.

To confirm our results we compare the green sample and the composed sample with green over blue when they are excited by electrons. As is shown in figure 4.7 both curves are essentially identical. There is no any evidence of the Ti peaks which are characteristic of the blue pigment. This clearly indicate that electrons only generate an appreciable fluorescence signal in the superficial layer.

Blue over green sample analysis

Figure 4.8 shows the obtained results when a blue over green composite sample (see figure 4.3 (d)) was irradiated by X-rays and electrons.

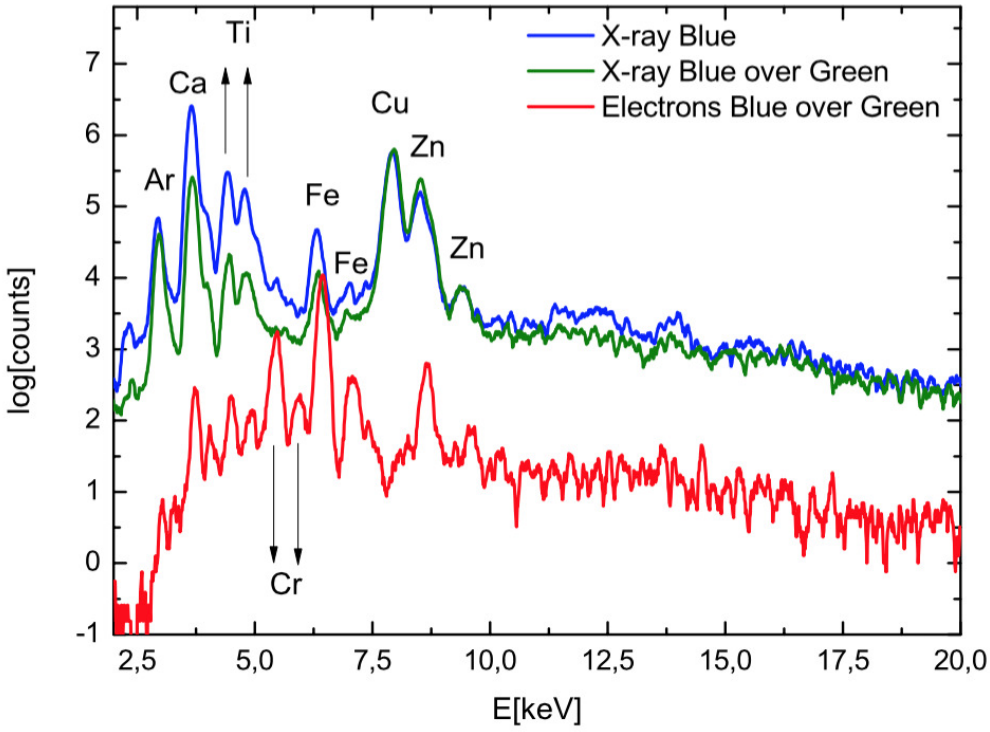

Figure 4.8: X-ray fluorescence spectrum for the blue pigment when excited by X-rays, and for the composed sample blue over green when excited by X-rays and electrons. In this case there is no characteristic peaks that can evidence the presence of the green painting under the blue one, but we can see a remarkable increment in the ratio between the peak of Zn and the Ti peak when we irradiated the blue over green sample with X-rays. As we checked in figure 4.5, green painting produce a stronger Zn signal than blue painting, showing thus that this painting is present in our sample.

As we observed in the calibration measurements (Fig. 4.5), the green painting does

not have characteristic peaks different from blue that could allow us to clearly identify it, so we will focus on the ratio between the Zn and Ti (K_α lines located at 8.6 and 4.5 keV, respectively). When the blue sample was irradiated by X-rays the fluorescence ratio between the Zn and Ti lines was 0.7. However, when the composite sample blue over green was irradiated also by X-rays, this ratio increased to 2.7, i.e., an increase of $\sim 387\,\%$, because of the high concentration of Zn of the green pigment. When electrons were used as irradiation source because of their limited penetration depth this ratio was reduced to 1.2 which is only $\sim 70\,\%$ larger than the original ratio. We attribute this $\sim 70\,\%$ difference to the difference in the relative excitation yields when X-rays or X-rays and electrons are used.

4.1.3 Conclusions and future applications

We have proved that our X-ray laser source can be used to analyse complex samples with the XRF technique. In particular, we have shown the potential of the combined use of electrons and X-rays, both emitted simultaneously from our source. While the high X-ray penetration permits a complete analysis of all the composition of the sample, using electrons we obtain information of just the superficial layer. According to this, our source allows to simplify the analysis of the XRF spectra and to obtain extremely valuable information about the superficial layers of the artwork. This technique could be used, for example, to study underlying painting and to extract not only its shape, as it is possible with radiography, but also to know the colours of this hidden painting.

In addition, the XRF analysis could be extended to other fields, like archaeology. In particular, this technique could be useful for studying dental pieces, and to extract information about the lifestyle of our ancestors. Although a tooth could seem to be composed only of Ca, it presents other elements that give valuable information. To mention some of them, we can find:

- *Fluorine (F)*, which is attributed to the caries inhibition.
- *Vanadium (V)*, which stimulate the mineralization of living bones and protect against the caries.
- *Strontium(Sr)*, which appears before the eruption of the teeth.
- *Lead (Pb)*, which is accumulated in the teeth.

We have tried to analyse the fluorescence signal from a dental piece. However, our preliminary studies did not give rise to conclusive results. The signal coming from to the impurities of the sample was too low to be measured with our setup (see Fig. 4.9). However, an improvement in the signal-to-noise ratio would allow to carry on this kind of analysis.

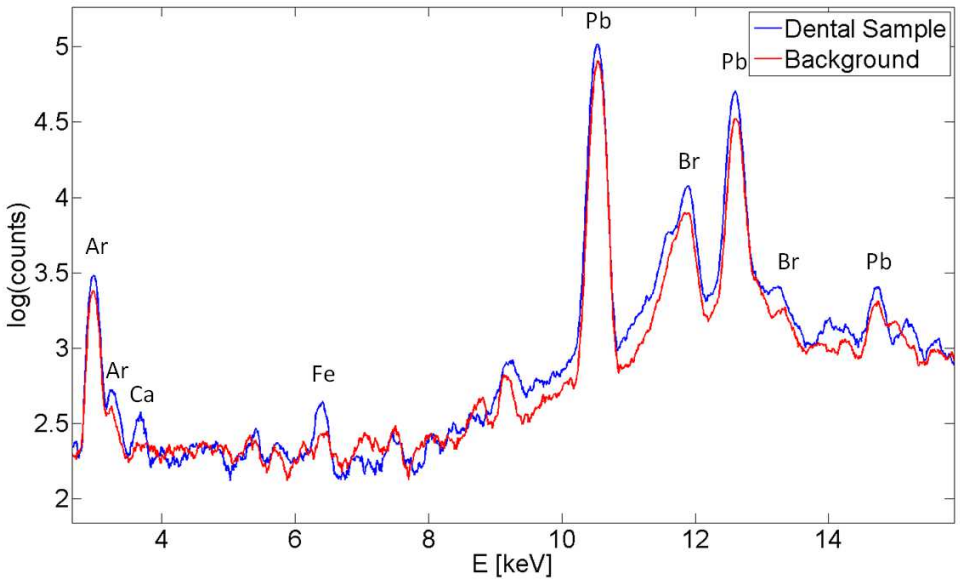

Figure 4.9: X-ray fluorescence spectrum for a dental piece. A Calcium K_α peak is observed over the background.

4.2 X-ray imaging

X-ray imaging is usually based on the absorption of a X-ray beam in a sample. Looking at the shadow of the sample, we can obtain information of its internal structure. Thus, the definition of the image is linked to the size of the source. If the source is too extended, the contrast of the shadow will decrease and information will be lose. In conventional X-ray tubes, a pinhole is usually used to have a small spot size. As we can focalize the laser to the order of microns, our source is suitable to make radiographies with high definition.

To test the capability of our laser driven source, we performed some radiography tests. These images were obtained in the commission stage of the X-ray station facility. At that point, the focalization system consisted in a 90 degrees off-axis parabola with 10 cm of focal length, which provides a focal of 4.2 μm spot when measured at low energy (avoiding filamentation). The parabola has a higher damage threshold than a microscope objective, since it is a reflective optic. In consequence, we could increase the pulse energy up to 2.5 mJ. With the measured focal spot, the maximum theoretical intensity that we could reach was $3.5 \times 10^{16}\,\mathrm{W/cm^2}$, but in practice it was limited by filamentation as usual. The target was a sheet of copper. The sample to be imaged was placed 5 cm away from the source in the direction of laser reflection as Fig. 4.10 shows. To acquire the image, we used EBT2 Gafchromic film over a RTQA2 Gafchromic film layer. The EBT2 has a dynamic range from 1 cGy to 10 Gy, while RTQA2 has a dynamic range from 0.02 Gy to 8 Gy.

In the first tests, we observed that the scattering of electrons in the sample produced a

blur image. To obtain an image produced only by the X-rays coming from the source, we filtered the electrons with a 2 mm methacrylate sheet placed between the target and the sample. An acquisition time of 3 hours was needed to obtain a clear image due to the high threshold of the films and the filtering of X-rays by the methacrylate.

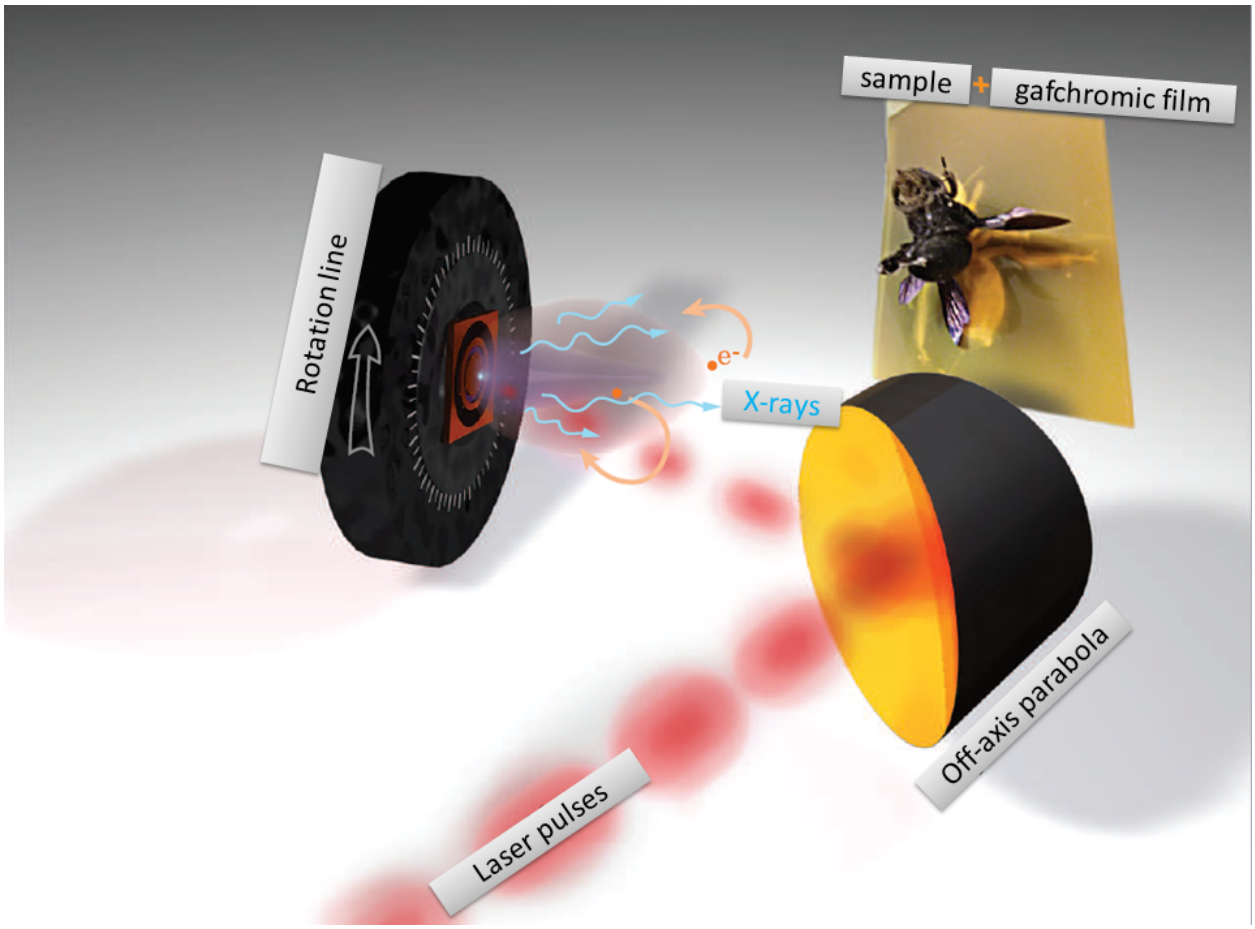

Figure 4.10: setup for X-ray imaging. In this case, the laser was focalized with a 90° off-axis parabola of 10 cm of effective focal length. The measured focus at low energy was 4.2 μm.

Figure 4.11 shows the radiography of a xylocopa purpurea. As we can observe, the small focal X-ray spot allowed us to obtain a high definition image of the sample. The details of the sample, like the capillaries in the legs of the xylocopa, are clearly defined. We also observe that the different response of the films emphasizes different details of the sample.

As we have confirmed, the small X-ray spot size made this source suitable for X-ray phase-contrast imaging. To obtain a phase-contrast image, it is only necessary to have a source small enough and to have the detector at a large distance from the sample [111]. In that condition, the images are formed due to Fresnel diffraction, providing information on both the real (X-ray phase shift) and the imaginary (X-ray absorption) components of the X-ray refractive index in the object. Thus, this technique allows to observe objects with low

(a) EBT2 film (b) RTQA2 film

Figure 4.11: X-ray radiographies made in the conditions of 4.11. Two different Gafchromic films have been used: EBT2 (uppest layer) and RTQA2 (lowest layer)

absorption, which present low contrast results when studied with conventional radiography, being specially useful in biomedical and industrial applications.

The conventional X-ray tubes and synchrotron sources are not suitable for the phase-contrast method. The X-ray tubes have a small spot size but the anode cooling leads to an unacceptably long imaging time. On the other hand, synchrotron radiation, which could be another source for phase-contrast imaging, is very bright and coherent, but is quite expensive.

However, the X-rays generated by laser have a very small focal spot size and a high repetition rate, the spectrum can be adjusted selecting the correct target and laser energy and they have an affordable price for laboratories. To adapt our setup for phase-contrast imaging, we only need a vacuum tube with an entrance filter to let the X-rays propagate without loses because of the air and to have a better image system than Gafchromic film, like a X-ray CCD camera.

Although there was no time for carrying out such images, they represent a good perspective to explore in the future.

4.3 X-ray polarimetry

Polarization is an important phenomenon in astronomy, as it provides information about the sources of radiation and allows to probe interstellar magnetic field in our Galaxy as well as in radio galaxies [112, 113]. Nowadays, new X-rays polarimeters are being developed to study polarized emission from astrophysical sources [114]. However, this polarimeters have to be

Incident radiation	**Energy (keV)**	**Crystal**	θ	**P**
Continuum	2.04	PET ($C(CH_2OH)_4$, 002)	45º	~ 1.0
Continuum	2.61	Graphite (002)	45º	~ 1.0
K_α Copper	8.048	Germanium (333)	45.06º	0.9849

Table 4.1: θ is the incident angle, P is the ratio between the incident radiation and the difracted for π-polarization. Data from calculation performed by [116]

tested and calibrated previously. For that reason, a polarized X-ray source is of interest for this scientific community.

In principle, our X-ray source is composed of unpolarized lines and a continuum Bremsstrahlung emission, since K_α photons are emitted without a preferential direction and electrons are randomly stopped in the bulk of the target. However, this emission can be polarized by the proper diffraction in a Bragg crystal. The diffraction angle θ in a Bragg crystal depends on the wavelength of the incoming radiation λ and the lattice spacing d according to the equation:

$$n\lambda = 2d \sin\theta \tag{4.1}$$

At 45º only the component of polarization perpendicular to the incidence plane is reflected [115]. Thus, selecting the crystal and target, we could obtain a polarized X-ray source for different energies. Table 4.1 shows some examples of the polarized lines that we could obtain. The versatility of our source allows to work with a broad spectrum of polarized lines.

We have tried to obtain polarized X-rays with our source. For that, the setup showed in figure 4.12 was built, where a Germaninun crystal should diffract the K_α line of Cu target. However, placing a spectrometer in the diffraction direction of the crystal, we did not observe an increment in the K_α line respect to the background. We attribute this to the bad quality of the Bragg crystal and so to its low efficiency. In the future, experiments with different targets and crystals with better quality should be performed. Not only a clear diffraction must be obtained, but also the polarization of this X-rays must be confirmed. For that, a second crystal should be used after the first diffraction. This crystal will be placed so the incoming radiation is s-polarized respect to the diffraction plane. Thus, if it is totally polarized, the radiation will not be diffracted.

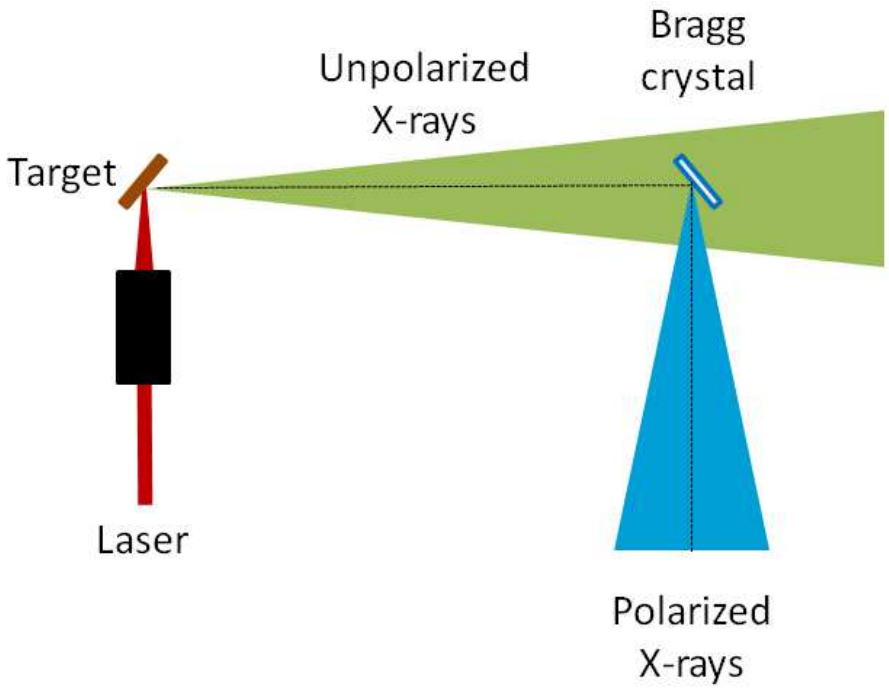

Figure 4.12: Schematic setup to develop a laser-driven polarized X-ray sourced. At 45°, a Bragg crystal only diffracts the p-polarized X-ray radiation of certain wavelength.

4.4 Radiation effects studies

As we have discussed, the outcoming radiation of laser-driven x-ray source inherits the temporal characteristics of the laser pulse, so its duration is in the range of picosecond/femtosecond regime. In consequence, dose rates produced by this source can exceed 10^9 Gy/s where the gray (symbol Gy) is defined as the absorption of one joule of radiation energy per kilogram of matter. These values contrast with the characteristics of conventional radiation beams used for medical purposes, whose dose rates are in the the order of 10 Gy/s in pulses of microseconds time duration. With our laser driven X-ray source, we have at our disposal the tool to explore the nature of the interaction between matter and ionizing radiation in conditions never met before. This kind of new interaction is specially interesting in the field of radiotherapy.

When tumoral tissue is irradiated, cell death is mostly produced by the energy deposition pattern of the radiation through the cell, rather than by a direct interaction with the DNA. The ionization radiation can eventually produce directly single and double strand breaks (SSB/DSB) on the DNA –direct damage-, but these lesions are very localized and the repair cellular mechanisms rejoin them efficiently increasing the survival rate of the cells [117–122]. However, the interaction of ionizing radiation induces different phenomena, being the most

relevant the creation of free radicals via water radiolysis. Free radicals are highly unstable molecules capable to induce indirect damage in the DNA. In contrast to direct damage, for indirect damage the initial ionizing track through the cellular medium defines the spatial distribution of defects induced in the DNA. That means, a cluster of SSB and DDB lesions is produced [4,12,123,124]. For such DNA clustered damage the repair rate is low (see figure 4.13).

The unique characteristics of laser-based ionizing radiation beams may open a new door for new radiotherapy treatments. On one hand, it is not known if delivering the same dose but with an enormous instantaneous dose-rates, i.e., in a much shorter time, may induce a different biological response. They may induce nonlinear or collective effects that cannot be described by the sum of the effect of independent particles [3,4]. Thus, the nonlinear effects could have advantages over the conventional radiotherapy treatments.

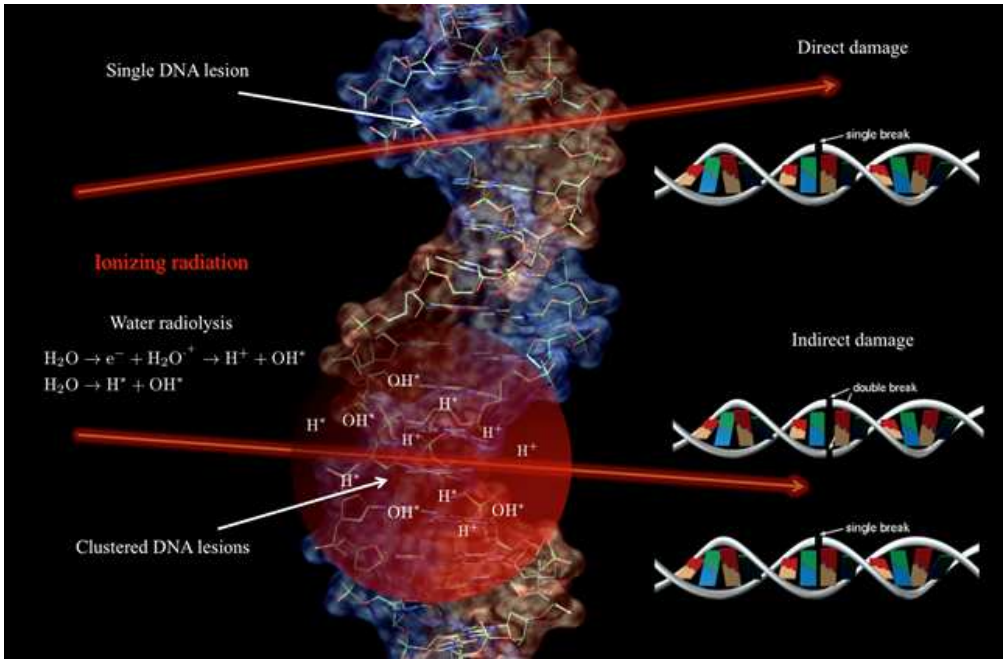

Figure 4.13: Schematic example of DNA direct and indirect damage. It is well documented that the indirect damage induced by water radiolysis far exceeds direct damage produced by the direct deposition of energy at the DNA [124].

On the other hand, nowadays, with the current radiotherapy treatments the energy deposition takes place in the microsecond time regime, which temporally overlaps the creation of radicals, the biomolecular damage (membranes and DNA lesions) and the cell repair mechanisms (see Fig. 4.14). Although this temporal overlapping does not affect in principle the efficiency of tumor regression, it may complicate the biological processes involved in the DNA repair [3, 4, 125]. Apart of being a new source of radiotherapy, the use of ultrashort pulses

would allow us to study the early dynamics of primary ionization, deepening our knowledge in the treatment of tumours with radiotherapy [126]. For example, it is known that the oxygen concentration of a cell is a critical factor for the radiosensitivity of a cell due to of its influence in the creation of free radicals, but very little is known about the early dynamics of these processes [4]

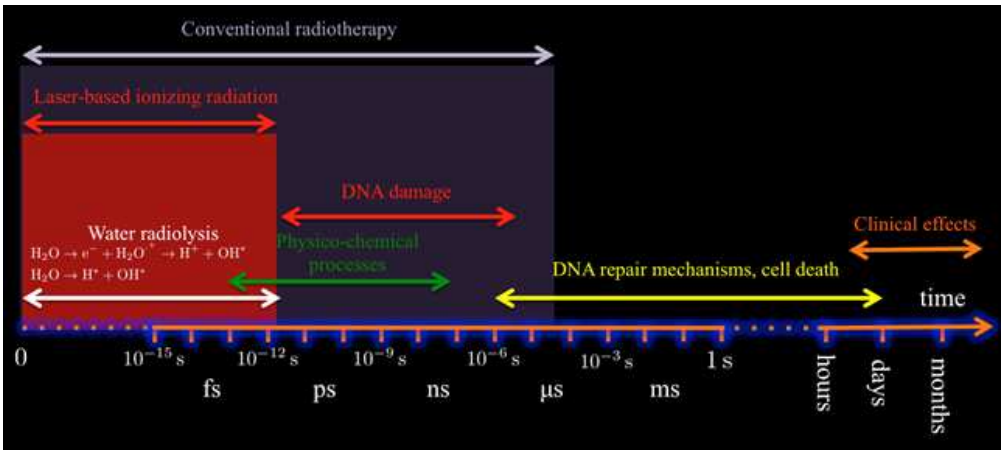

Figure 4.14: Schematic diagram for the relevant processes in radiotherapy as a function of time.

In literature one can find only few preliminary studies about the effect of ultrashort radiation. Besides, these studies took place with different cellular lines and mostly in vitro, showing inconclusive results (see for example [6–8, 13, 14]). This technology is so novel that so far there have been no systematic studies to probe the hypothetical advantages of ultrashort ultraintense ionizing radiation. Due to the importance of this application, further investigation is strongly required. To make a contribution to this field and achieve one day the answer to all these questions, we have established a collaboration with the Biomedicine Institute of Sevilla (IBIS). The idea is to use drosophila melanogaster to perform this research. We considered the drosophila as the best scenario for several reasons: the drosophila is the last biological sample that does not implies ethical problems, it is cheap, its genome is known and tumours can be controllably induced. At this moment, CLPU and IBIS are looking for financial support to carry on a project in which the effects of conventional radiotherapy and laser-driven X-ray radiotherapy in drosophila melanogaster will be compared.

4.5 Intraoperative Radiation Therapy (IORT)

The Intraoperative Radiation Therapy (IORT) consists in the deposition of a single dose of radiation directly in the tumour while the area is exposed during surgery. This technique let

to focus the radiation only in the cancerous tissue, avoiding damage in healthy organs and allowing the application of a higher dose that conventional radiotherapy techniques. In this sense, IORT competes with protontherapy, where the Bragg peak of heavy particles is used to localize the main damage of the radiation source (Fig. 4.15). As the tumour is exposed, in IORT X-rays or electrons, which have low penetration depth, can be used to irradiate the tumour up to high dose rates.

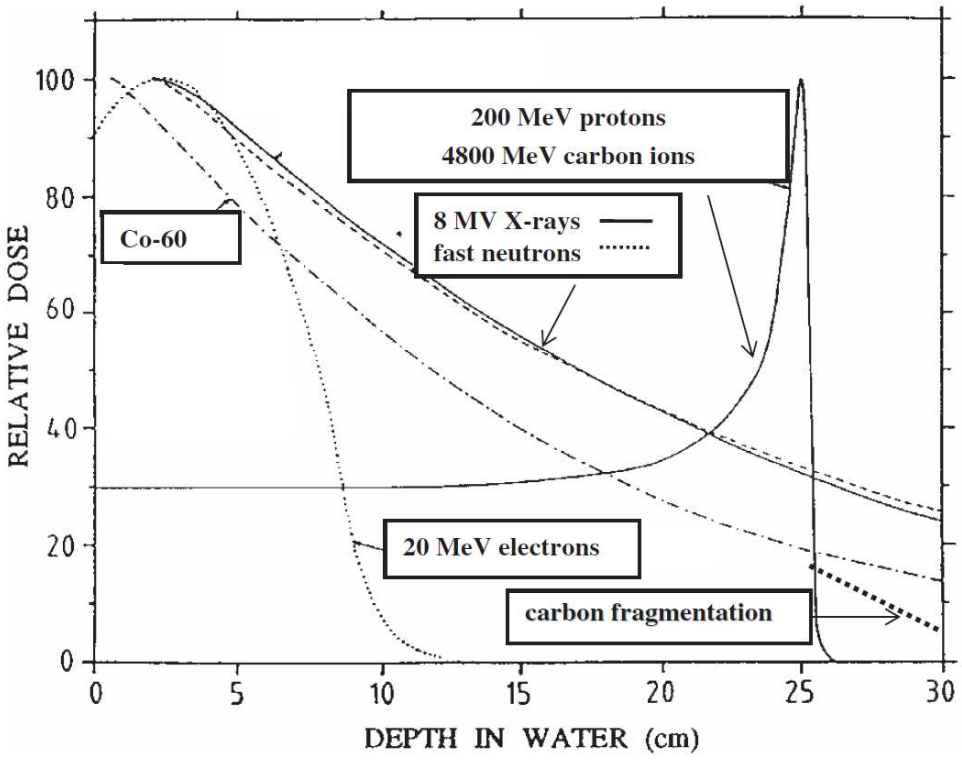

Figure 4.15: Energy deposition of different radiation sources. Image from [127]

Despite the advantages of this kind of radiotherapy, IORT is not broadly use. The current results do not allow to make statistics to prove the efficacy of this technique, but the main reason in the delay of its implementation is the huge accelerator systems that it requires, usually a linear accelerator. Although the use of portable accelerator are rising, there are still difficulties in their transport and in the construction of the required infrastructure. We have to take into account that the patient must be moved from the surgery table to the accelerator in an aseptic environment. Besides, the current accelerators do not allow to treat tumours with complex localizations, as they do not have versatility in the transport of the radiation beam.

All these problems could be overcome with the use of ultraintense lasers. The laser beam can be easily transported to the surgery room (figure 4.16). Also, a robotic arm could be directed toward the tumour, where the laser would be focalized and the radiation generated

(Fig. 4.17a and Fig. 4.17b).

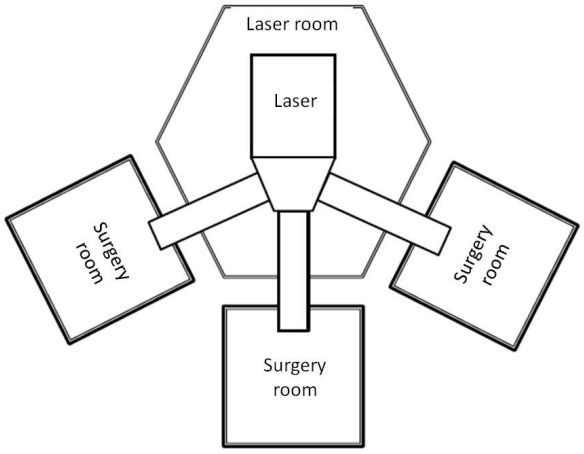

Figure 4.16: Distribution of the infrastrusture for IORT. One laser can give service for several end stations. Image from [128].

FLUKA simulations have showed that the required laser power needed for an effective treatment are in the order of 4-20 TW [128]. However, these studies were done assuming the ulstrashort radiation has the same behaviour as conventional radiotherapy, which is, as we said, a question that has still to be answered.

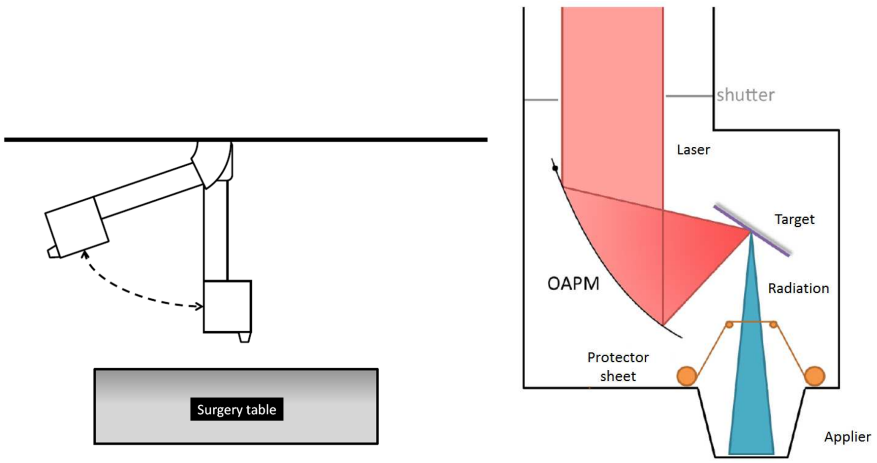

(a) (b)

Figure 4.17: IORT arm. The laser is guided toward the patient. In the applier, an off-axis parabolic mirror focalizes the laser in the target, generating the desired radiation. A sheet of a proper material is placed to protect the patient from the debris.Image from [128].

4.6 Studies for a new generation of radiation detectors

Ultraintense lasers have introduced a new paradigm in the physics of particle accelerator. Lasers can produce ultrashort particle beams with high brilliance, low emittance and broad energy spectrum, a kind of radiation for which the conventional detectors are not prepared. Although passive detector seem to give a reliable measurement, the reliability of active detectors has still to be proved.

Our X-ray source is a good scenario to research new radiation detectors for Ultraintense Laser Facilities. In particular, the Radioprotection Department of CLPU has used the X-ray source presented here to study the response of commercial EPDs (Electronic Personal Dosimeters) to the laser driven ultrashort radiation and has made a preliminary study for the development of a new generation of EPDs that could address with the nature of this kind of radiation [129].

4.6.1 TLDs test

One of the detector that seems to be reliable with the laser driven radiation source is the ThermoLuminiscence dosimeters (TLDs). They consist in a crystal chip where impurities has been introduced to create trap states. When a ionizing particle hits the crystal, an electron is trapped in one of these states. After irradiation, the TLD is heated, resulting in the relaxation of the trapped electrons by a thermoluminescence process. Thus, the light emitted by the TLD can be related with the dose that has received.

The CLPU has calibrated TLDs for the experiments that will take place in VEGA laser. This calibration is prepared for the high energies that are expected in experiments in VEGA laser (hundred of keV). On the other hand, previous works [51] used TLDs prepared for low energies ($< 100\,\text{keV}$) to estimate the dose in a EBT2 Gafchromic film irradiated by a laser driven X-ray source, resulting in the following calibration:

$$Dose(cGy) = 27.76OD + 68.96OD^{3.078} \tag{4.2}$$

where OD is the optical density of the Gafchromic film (see Chap. 2). This calibration was done with the same set of films that we used, but Gafchromics get deteriorated with time due to background radiation and we cannot ensure this calibration is still valid. However, it allowed us to analyse the response of the TLDs.

To compare the calibration of the available TLDs and the Gafchromic film, the TLDs where placed in a support matrix covered by a film of mylar to avoid them to fall (see Fig. 4.18). The detectors were exposed during 20 min at a distance of 2.5 cm from the source in the laser reflection direction. The same exposure conditions were applied to the Gafchromic film. The Gafchromic film was scanned with the same EPSON-V750 PRO scanner that

was used to calibrate them. An average in the area where each TLD is supposed to be positioned was done to compare the dose. The measurement of the TLDs was carried out by the Radioprotection Department of CLPU. This measurement took placed several days after irradiation to minimize reading errors and to smooth the spurious peaks that appears in their measurement. The detectors were read with a TLD model 4500 with WinRes, having the approximation of ROI-1 curve and with the relation 105 nC = 3.7 mSv. Two set of expositions, with parameters summarized in Tab. 4.2, were performed.

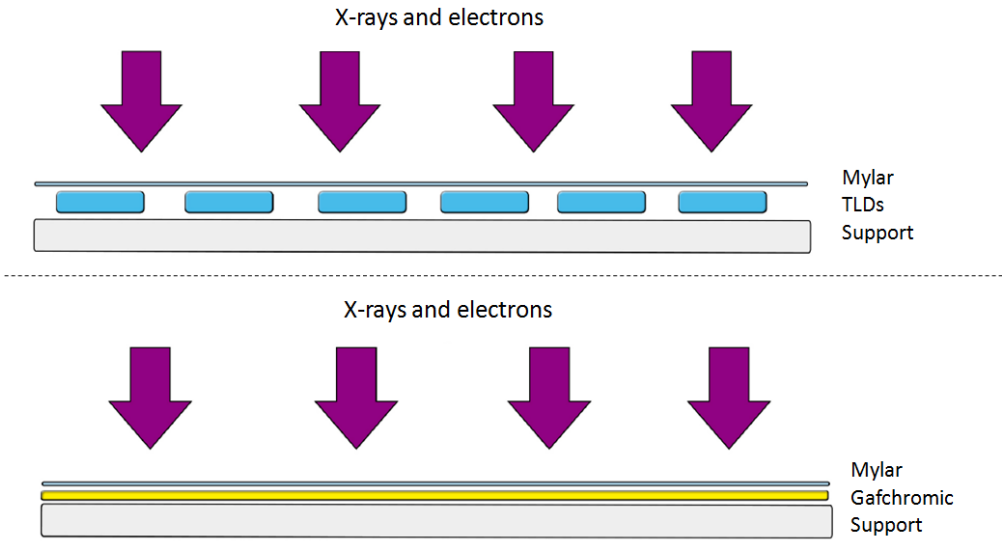

Figure 4.18: Setup for the comparative of TLD and gafchormic film calibration.

Figure 4.19 and 4.20 show the results of the dose registered by the TLDs and the Gafchromic film in both expositions. First of all, we can observe that the TLDs measurement is strongly dependent of the waiting time until they are read. In consequence, a protocol for their reading must be established, ensuring that they will be processed in the same condition. On the other hand, we observe a strong variation in the TLDs measurement for low energies, meaning that their calibration for high energy cannot be extrapolated to low energies; they need a more precise calibration with a known source in the range of the energies produced by our laser driven X-ray source.

	Experiment 1	Experiment 2
Laser Energy	2.23 mJ	2.23 mJ
Number of TLDs	24	32
Gafcromic film	EBT2	EBT2
Cover film	Mylar	Mylar
Film thickness	250 μm	125 μm
Exposure time	20 min	20 min
Distance to the target	2.5 cm	2.5 cm
Time for postprocessing after irradiation (TLD)	5 days	4 days
Time for postprocessing after irradiation (Gafchromic)	30 min	30 min

Table 4.2: Parameters for the comparative of TLD and Gafchromic film calibration.

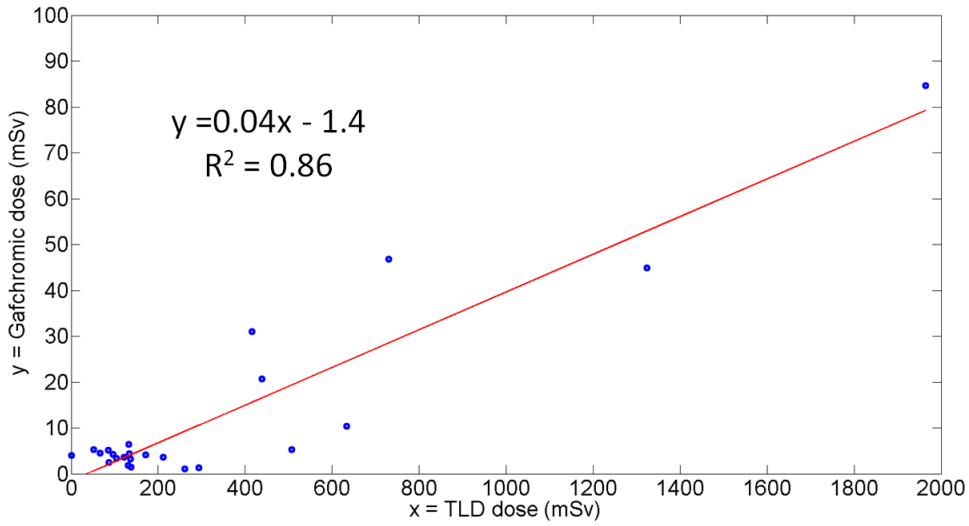

Figure 4.19: Comparative of TLD and Gafchromic dose in the first exposition.

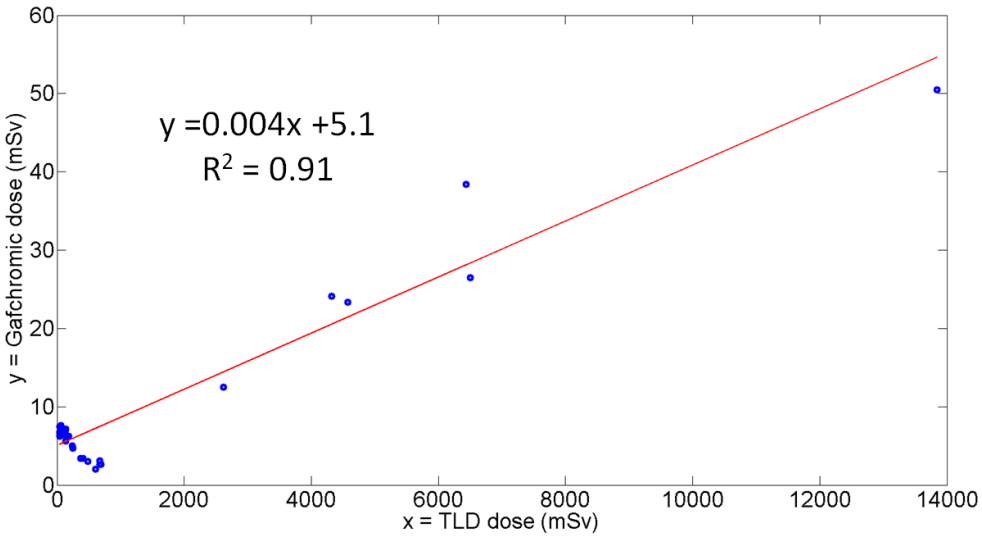

Figure 4.20: Comparative of TLD and Gafchromic dose in the second exposition.

Chapter 5

Laser optimizations for a laser-driven radiation source

Nowadays, the scientific community is making an effort to develop a laser-driven radiation source (particles or X-ray) that can achieve the maximum laser-radiation conversion efficiency. For this purpose, more and more complex systems are being proposed. For particle acceleration, for example, new kind of targets are being tested [1]. However, these kind of targets, although allow to obtain high energetic particles, have a problem with the repetition rate, being necessary to change the target in every shot. In this thesis we wanted to make an effort in not finding the most efficiency laser-radiation source, but in finding a reliable system that can compete with the well-established radiation sources that we have nowadays, like X-ray tubes or other particle accelerators. In this sense, in chapter 2 we have presented a vacuum free laser-driven X-ray source. Also we tested a liquid target, which allowed us to have a high repetition radiation source. We checked that the conversion efficiency was high enough for this source to have practical applications, as we have seen in Chap. 4.

However, if we want to compete with the current radiation systems, not only an effort in the improvement in the laser radiation production must be done. There is margin to introduce modifications in the laser itself to achieve a cheap radiation system. In consequence, in this chapter, we will present two modifications for the laser. One is a efficient pump system that allows to obtain a uniform pump profile, which is necessary to obtain a good focus and thus the high intensity needed to produce radiation. The other is a proposal for a modification in PW compressors which would reduce the price in lasers systems dedicated purely to laser particle acceleration.

5.1 Simulations of the gain profile of a diode side-pumped QCW Nd:YAG laser

Until now, the Nd-doped solide-state lasers used as pump for Ti:Sapphire lasers were pumped by flash lamps, using high voltage to excite the gas and obtaining huge amounts of power. Despite the energy provide by these systems is extremely high, the use of flash lamps limits the repetition rate of the final system due to the broad spectrum of the flash lamps and the consequently undesired excitations that leads to heating of the Nd crystal. In contrast, laser diodes emit a much narrower spectra, just of few nanometers, and can be tuned to match the excitation lines of the Nd crystal, avoiding thermal effects [130].

However, to obtain a uniform pump pattern is difficult when working with diodes. In principle, diode emission pattern can be corrected with microlenses or can be coupled into a fiber [131]. For high power lasers, a transverse pumping with the diodes in a stack is usually chosen. Besides, this scheme can be scaled by increasing the number of diodes around the rod. The issue addressed by the laser community is to find the best configuration of diodes to achieve a uniform pump distribution [132].

In this section, we analyse a proposal for diode side-pumped Nd:YAG pumping chamber. This module has been developed by Monocrom S.L. and is planned to be used as part of a high-power nanonsecond Nd:YAG laser in MOPA configuration. To analyse the absorbed pump energy distribution inside the Nd:YAG rod, a code based on a ray-tracing Monte Carlo method has been developed. Additionally, measurements of the distribution of fluorescence has been carried out by Roberto Lera and the Proton Laser Applications S.L. team. In the following, we present our simulations and we compare them with the real measurements.

5.1.1 The diode side-pumped Nd:YAG pumping chamber

The pumping chamber consists in a set of diode stacks, a flowtube and a Nd:YAG immersed in cooling water (see Fig. 5.1). Six QCW diode bars, with 100 W of power each are assembled in six stacks that symmetrically surround the active medium, resulting in a total optical power of 3600 W. The diodes are cooled conductively and tuned to emit in the vicinity of 808 nm with a spread of 2 nm of FWHM, matching thus the maximum absorption of Nd:YAG. The diodes are powered by 100 A, 200 μs square pulses. The active medium is a Nd:YAG cylindrical crystal rod, with 6 mm of diameter, 90 mm length and 0.6 at. % doping concentration.

The rod has a fine ground finish in order to avoid parasitic oscillation and is cooled by a sleeve of flowing water. In particular, the Nd:YAG rod is surrounded by a layer of circulating water confined by the flowtube, which is made of fused silica due to its high transmittance in

the near-infrared. The outer surface of the flowtube is coated with a thin foil of aluminium, reflecting approximately 87 % of the unabsorbed pump light back into the rod, minimizing optical loses. A 2 mm wide transparent slit is imprinted on the aluminium coating, in front of each laser diode stack, to leave a free path for the light of the diodes to reach the active medium. The laser diode stacks are situated at a distance from the active medium such that most of the light emitted is refracted and traverses the Nd:YAG rod (see Fig. 5.1).

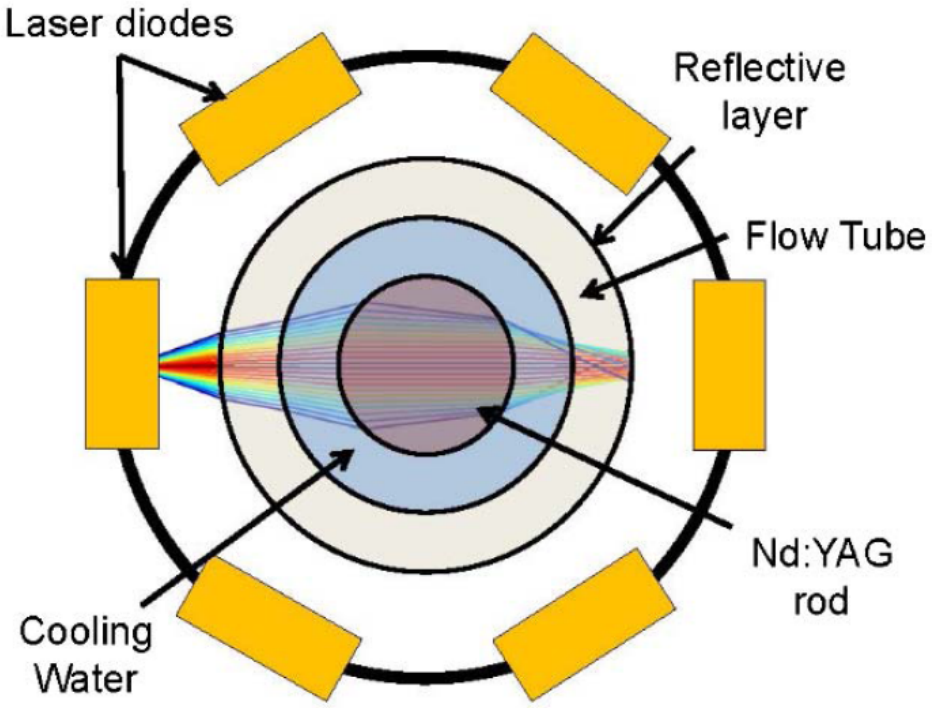

Figure 5.1: Transverse section of the diode pumping scheme. The Nd:YAG cylindrical rod is placed at the center surrounded by cooling water and by the flowtube. An example of ray tracing of the light from one of the diodes propagating through the setup is included.

5.1.2 Ray-Tracing formalism

The simulations are based on a ray-tracing Monte Carlo code: the light radiated by the laser diodes is treated geometrically as rays generated with random angles and intensity weighted according to the emission pattern. Laser diodes exhibit different propagation properties along the two normal axes known as fast and slow. The fast axis pattern can be approximated by a Gaussian profile, as in Eq. (1). However, the pattern of the slow axis is more complex, as the modelling requires an extended source:

$$I(\theta) = I_0 \exp\left(-\left(\theta_f^2/\phi_f^2 + \theta_s^2/\phi_s^2\right)\right) \tag{5.1}$$

where θ_f and θ_s are related to the fast and slow axis FWHM divergence, as $\phi = \frac{\phi_{FWHM}}{\sqrt{2\ln(2)}}$. For these diodes, the values of divergence are 30º and 5º, respectively. Also each ray has a random wavelength associated within the emission spectrum.

Each ray i is defined by its initial position $\mathbf{r_0}$, the virtual source of the ray, angle, defined by the unitary vector $\mathbf{k}$, and a real parameter p, as in Eq. 5.2. These rays propagate freely until the intersection with each of the three interfaces, as shown in Fig. 5.1. These interfaces are cylindrical surfaces, so they can be expressed as Eq. 5.3, R_j being their respective radius:

$$\mathbf{r_i} = \mathbf{r_{i0}} + p\mathbf{k_i} \tag{5.2}$$

$$x^2 + y^2 = R_j^2 \tag{5.3}$$

The intersection between each ray i and surface j is the solution to the system of Eqs. 5.2 and 5.3, which can be solved by numerical methods or reduced to a quadratic equation for p (choosing the positive solution, as the ray is going forward) and solved analytically.

On the point of the intersection between the ray and the surface, the normal vector to the surface n has to be calculated in order to compute the change of direction suffered by the ray when refracted, according to Eq. 5.4, Snell's law:

$$n_j|\mathbf{k} \times \mathbf{n}| = n_{j+1}|\mathbf{k}' \times \mathbf{n}| \tag{5.4}$$

Solving this vectorial equation will lead to several possibilities for the refracted ray; the solution must maximize the scalar product between the incident and the refracted $\mathbf{k}$ vector and the scalar product between the refracted and the normal vector must be negative [133]. An easier way to obtain a solution is to define a vector perpendicular to the plane of incidence (defined by $\mathbf{n}$ and $\mathbf{k}$) and rotate $\mathbf{k}$ around this vector by the angle $\Delta\theta$, defined as the difference between the refracted ray (solution of Snell's law in scalar form) and the incident ray, again choosing wisely between the possible solutions.

The same procedure is done for the ray i every time it encounters a surface boundary. Once it has traversed the active medium and reaches the outer surface, where a layer of reflecting material is located, as in Fig. 5.1, the ray experiences specular reflection and now travels backward. The process ends when the energy associated with each ray falls below a threshold.

For the calculation of absorption, the active medium is divided into elements of volume. Each of these elements is associated to a scalar, representing energy, which grows whenever a ray travels through the volume and is absorbed. In the nonsaturated regime, the energy

deposited by the ray within each volume is calculated according to Beer–Lambert law of absorption:

$$\Delta E = E_0(1 - \exp(-\alpha \cdot \mathbf{\Delta r})) \tag{5.5}$$

where ΔE is the energy absorbed within the element of volume, E_0 is the energy of the incoming ray, Δr is the space travelled by the ray inside each volume, and α is the absorption coefficient of the active medium, which depends on its dopant concentration and wavelength of the pump source. When the ray travels to the next element of volume, its initial energy E_0 is diminished by ΔE.

Once all the rays have been launched, the position of the source of the rays is rotated by 60º around the longitudinal axis to simulate the adjacent diode stack. The total distribution of absorbed energy within the active medium is calculated by adding the contributions of all individual rays of all diode sources.

5.1.3 Simulations

Although the formalism presented in last section was developed to perform 3D simulation, a 2D representation of the fluorescence profile can be accurate enough if we assume that the distribution along the longitudinal axis is homogeneous. This is not the case at both ends of the pumped volume, but their contribution to the fluorescence profile is small enough to be ignored. This approximation reduces drastically the computing time and analysis of data. These simulations where double checked with CLPU Chirper, a ray-tracing and the laser amplifier simulator that I developed for my bachelor degree thesis.

The simulations were made with a mesh of 150 nodes representing the active medium, which corresponds to divisions of about $40 \times 40\,\mu m$, in the case of a 6 mm diameter rod, which is enough resolution for this kind of simulation. The laser diode stacks were represented with 105 rays each.

Figures 5.2 and 5.3 shows the result of the simulation. We observe the presence of higher gain zones located in the outer zones of the crystal due to the overlapping of the light emitted by the pumping diodes. The total absorption of the pumping light was estimated to be 89%.

To test the validity of the simulations, the fluorescence pattern of the Nd:YAG rod was imaged with a 4-f system comprised of two positive lenses of 100 mm focal length separated 200 and 100 mm away from the CCD. An aperture in the Fourier plane of the first lens was placed to work as a filter. The lens closest to the camera was placed over a translation mount in order to achieve the best possible quality of the fluorescence image. To avoid noise coming from the diode's nonabsorbed light, a line filter for 1064 nm was used. This measurements, as it was mentioned, were performed by the Proton Laser Applications S.L. team.

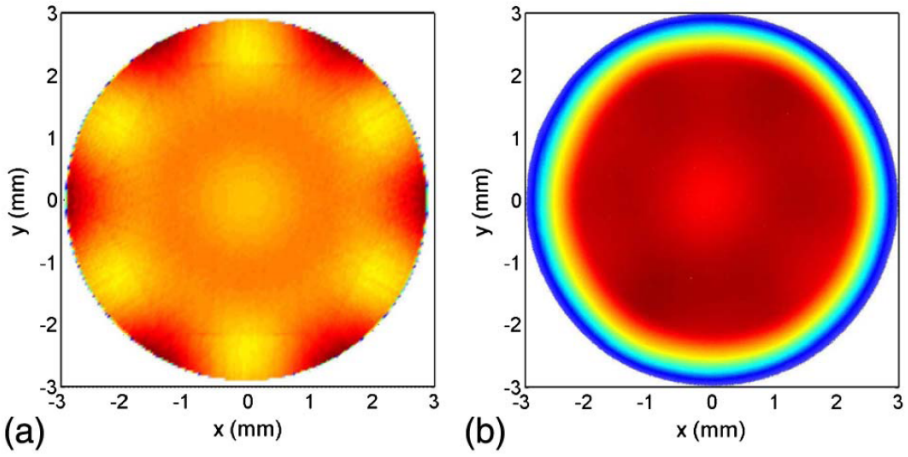

Figure 5.2: (a) Simulation of the distribution of absorbed power inside an Nd:YAG active medium. (b) Measured distribution of fluorescence in a transversal plane of a Nd:YAG crystal of 6 mm diameter.

Figure 5.2 shows the experimental fluorescence profile and Fig. 5.3 shows the 1D cuts compared with the simulations. The outer regions of the Nd:YAG rod could not be imaged properly because of diffraction. We observe that simulations are in agreement with the measured fluorescence. We observe higher gain in the outer zones of the crystal due to the superposition of the light coming from the diodes, and lower gain in the central zone. Despite all the light coming from the diodes overlaps in the center of the rod, the gain here is lower since the light has been absorbed in the outer region. This can be fixed by lowering the doping concentration of the active medium or decreasing the Nd:YAG rod diameter, at the expense of absorption efficiency.

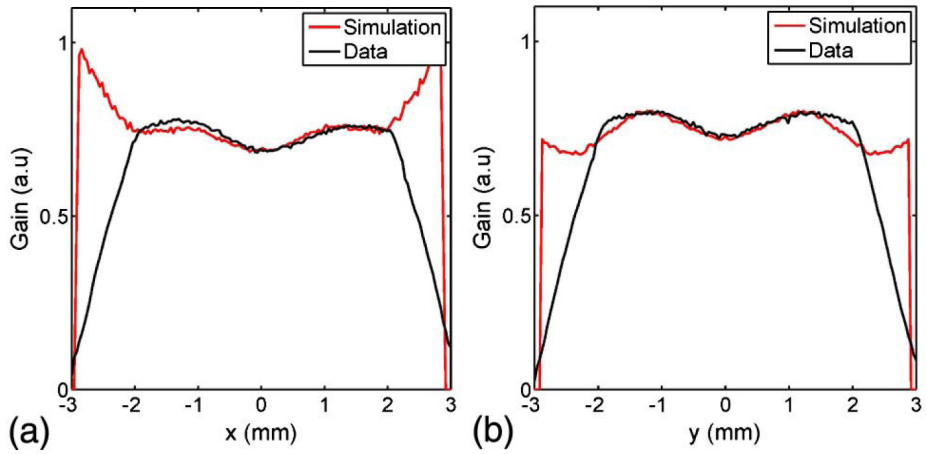

Figure 5.3: Comparison of the simulated absorbed power and the measured fluorescence of the Nd:YAG rod. (a) horizontal cut and (b) vertical cut

5.1.4 Performance

The performance of the laser module was also studied by the Proton Laser Applications S.L. team. For that purpose, a basic resonator of 51 cm length, with pumping chamber placed 5 cm from the rear mirror was constructed. The output coupler had a reflectivity of 85% and was plane-parallel, while the rear mirror had a 99.9% reflectivity and was plane-parallel as well. This cavity was found to be stable because of the thermal lensing provided by the Nd:YAG.

Figure 5.4 shows the dependence of energy per pulse with respect to the central wavelength of the laser diodes used for pumping the Nd:YAG rod. The temperature of the cooling water was adjusted in order to optimize the laser power. The central wavelength and power of the diodes were measured simultaneously; the wavelength was recorded through a special window that overlooked the laser diodes, while the laser was operating at full power.

The maximum power was measured at two different repetition rates (500 and 700 Hz). It can be seen that the maximum is located close to 807 nm. However, it shifts slightly between the two curves, probably due to the less efficiency of the cooling produced by the water as the average power increases and, hence, the heat dissipation produced by the active medium and the diodes. This implies that to scale the power, the cooling capacity of the unit must be increased to maintain the maximum located at 807 nm.

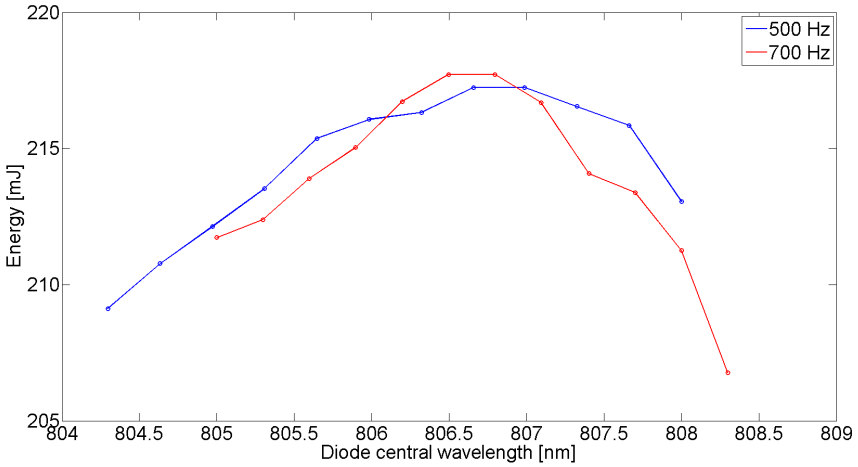

Figure 5.4: Dependence of energy per pulse with as a function of the central wavelength of the laser diodes used for pumping the Nd:YAG rod. It was measured at 500 and 700 Hz.

A maximum power of 220 W was achieved at a repetition rate of 1 kHz with 200 μs pumping pulses. Taking into account the pump power, this corresponds to an efficiency of 30.5%. The output was stable with no decrease or drift in the average power during several hours of operation. Figure 5.5 shows the output power as a function of the repetition rate.

We can also observe in this picture that the energy per pulse was fairly constant for the whole range of repetition rates, meaning that the change in the thermal lensing with respect to the average power was not steep. Otherwise the stability condition of the cavity would have modified the output characteristics of the laser. The transverse profile was a multimode top-hat beam due to the fact that high input power leads to many modes excited in the rod.

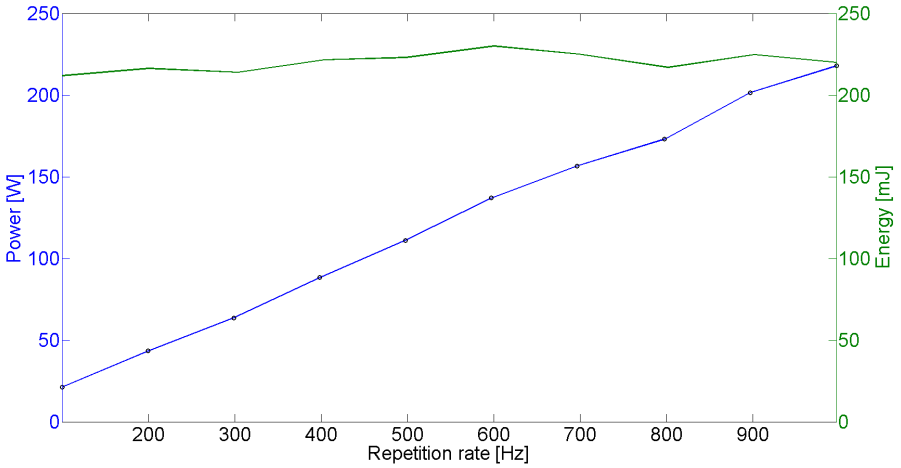

Figure 5.5: Power of the QCW laser with respect to the repetition rate (blue). In the same figure, the dependence of the energy per pulse as a function of the repetition rate is also shown (green).

5.1.5 Conclusions

We have devoleped a simple code by means of basic ray optics equations on a Monte Carlo method to simulate the pump energy distribution in a Nd:YAG rod surrounded by diodes. The Proton Laser Applications team has verified he simulation by measuring the distribution of fluorescence inside the active medium with a 4-f optical system and a CCD camera, finding remarkable accordance. The profiles both simulated and measured showed similar features, mainly a little dip in the center of the active medium, for a 6 mm diameter, 0.6 at. % doping concentration Nd:YAG crystal rod, which can be corrected by changing the dope concentration or decreasing the diameter of the rod

The Proton Laser Applications team has also proved that inserting the pumping chamber in a plane-parallel cavity and operated in QCW pulsed mode, a maximum power of 220 W was obtained when pumping with 200 μs pulses at 1 kHz repetition rate, which corresponds to an optical-to-optical efficiency of 30.5 %. The control of the temperature of the cooling water allowed to optimize the energy per pulse. During operation of the laser, the optical cavity arrangement was left unchanged, suggesting that thermal lensing varies smoothly with

repetition rate. The beam profile was highly multimode, so operation at the fundamental mode would require substantial losses to be introduced in the cavity.

Thus, our simulations have been proved to be a powerful tool in the design of diode side-pumped lasers. Changing the parameters either concerning the pumping geometry or the characteristics of the active medium allows for the optimization of the gain profile. Furthermore, the simulations can be used to estimate the temperature profile inside the rod and therefore predict thermal lensing and mechanical stresses.

5.2 Single pass compressor

As we exposed in Chap. 1, the aim of the compressor is to give back the pulse its original duration. For that, the pulse is diffracted in a grating to spread its frequencies and to let them go through different paths. A compressor is usually composed of two gratings and a reflector. The second grating collimates the beam, while the reflector makes the pulse to go back, resulting in a double-pass configuration. The distance between grating is set-up so when the pulse reaches again the first grating, all the frequencies are synchronized.

However, there are other possible configurations for a compressor. One option is to make a single pass compressor by doubling the distance between the grating (see Fig. 5.6). In that case, after the diffraction in the second grating, all the frequencies are synchronized and there is no need of using a reflector. However, we must notice that in this case, there is a frequency spread across the transversal profile of the pulse. This implies that the pulse is not spatially compressed. While all the frequencies overlap in the center of the pulse, and the duration there is ultrashort, there are only few frequencies in the edges of the beam, so the time duration there is longer. Although a profile like this could arise some concerns for its use in laser particle acceleration, we must take into account that when the laser is focused, all the frequencies overlap in the focus, and then the intensity that the laser reaches is comparable with the intensity of a conventional compressed pulse. In consequence, a single pass compressor configuration offers several advantages compared with the double-pass configuration.

First of all, in a conventional compressor, the size of the beam, which determines the size of the gratings, is limited by the femtosecond damage threshold of the last grating, which is of the order of $100\,\mathrm{mJ/cm^2}$. However, in our modified compressor, the size is limited by the picosecond damage threshold of the entrance grating, which is the one that supports more fluence. In this case, the damage threshold is of the order of $1\,\mathrm{J/cm^2}$ [132]. In consequence, the beam size can be reduced, and so the size of the grating and the cost of the total system.

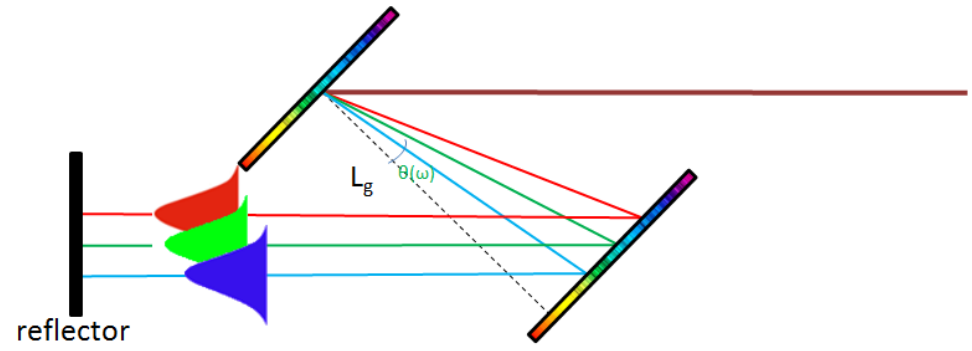

(a)

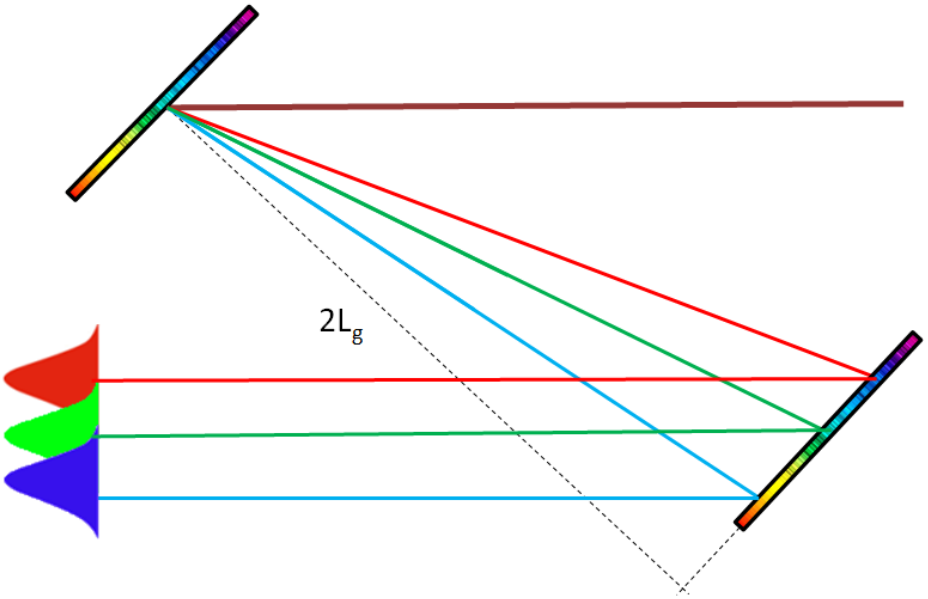

(b)

Figure 5.6: Double (a) and Single (b) pass compressor.

In the worst case, where the incidence in the grating would be perpendicular, the diameter of the beam d_T in order not to overcome the damage threshold fluence F would be:

$$d_T > \sqrt{\frac{4E}{\pi F}} \tag{5.6}$$

For a conventional beam of 24 cm, like VEGA III, the beam could be reduced up to 7,4 cm.

Moreover, this reduction of the beam allows new geometries that could not be possible with the conventional compressors. The smaller sized of the beam allows to work near de

Littrow angle of the gratings, where the efficiency is higher. Figure 5.7 shows the possible compressor for a set of angle of incidence, distance between gratings and separation between beams (distance between the edge frequencies after the diffraction in the second grating. The coloured part of the surface represents the compressors that are possible since the beam does not hit the first grating after the diffraction in the second one. We can observe how the number of possible compressor increases with the distance between gratings. The red point corresponds to a compressor similar to the VEGA III compressor but with an incidence angle of 42º, which is close to the Littrow. The green points represent a single pass and a double pass compressor for VEGA III with an angle of incidence of 56º and distance between gratings of 90 and 180 cm respectively.

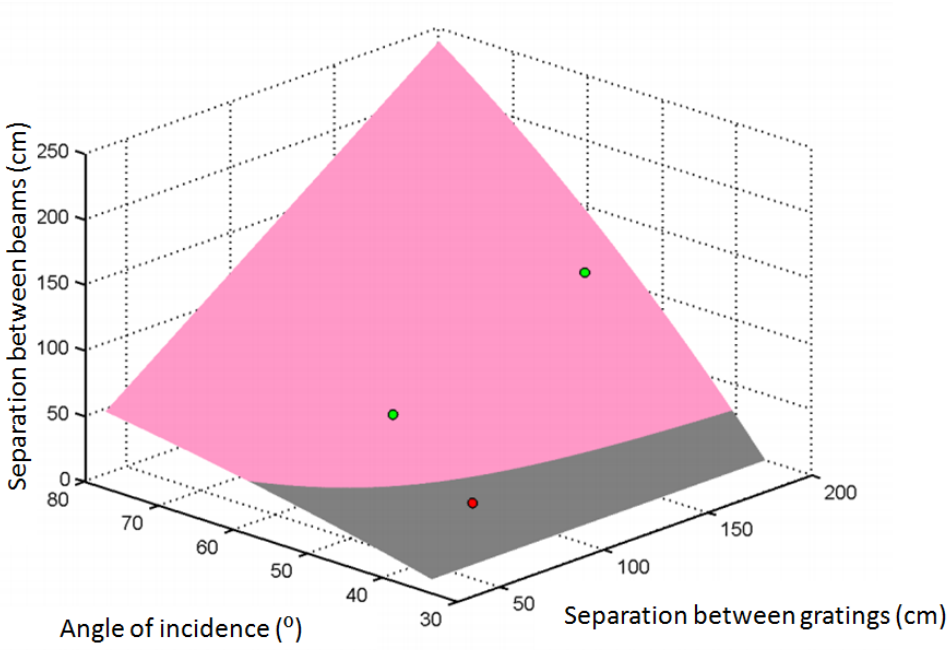

Figure 5.7: Possible compressor for a set of angle of incidence and distance between gratings and distance between the edge frequencies after the diffraction in the second grating. The parameters of the system are similar to VEGA III: gratings of 1480 lines/mm and and initial beam diameter of 24 cm.

As we have said, the proposed compressor presents the same focalization capabilities as a conventional one [134, 135]. To prove that, we can make an estimation of the focus by considering each frequency as an independent Gaussian beam (Fig. 5.8)

Let's $\mathbf{r} = (x, y, 0)$ be the vector that goes from the center of the focus to the observation point in the plane where we want to calculate the focus. If ρ is the projection of $\mathbf{r}$ in a perpendicular plane to the propagation direction of the beam, then the electric field for the frequency ω in the observation point will be:

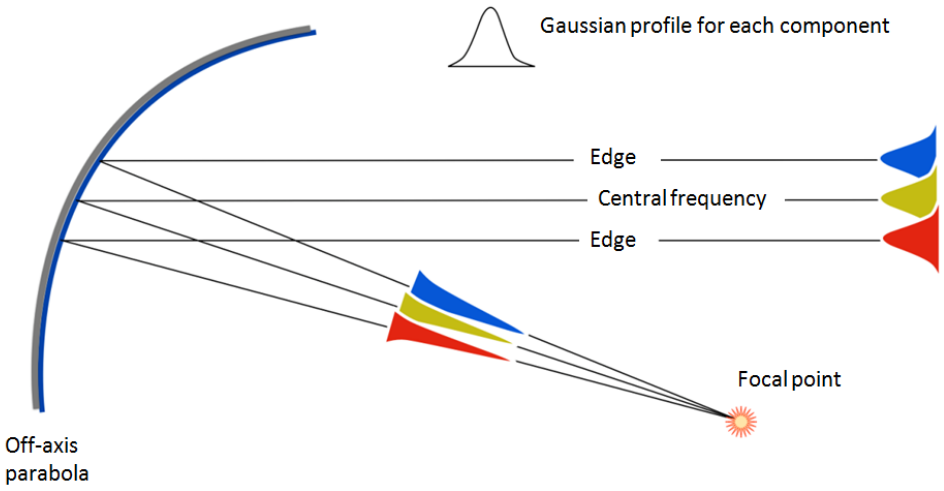

Figure 5.8: Focalization in a two pass compressor.

$$E_\omega = \frac{E_{0,\omega}}{\sqrt{\pi \mathrm{w}^2/2}} e^{ik(s_x x + s_y y)} e^{-\frac{\rho^2}{\mathrm{w}^2}} \tag{5.7}$$

where $\mathbf{s} = (s_x, s_y, s_z)$ is a unitary vector in the propagation direction and $E_{0,\omega}$ is the electric field amplitude for each frequency. In a first approximation, we can give arbitrary units to the electric field, but the amplitude of each frequency will be proportional to the spectral value of the pulse for that frequency. On the other hand, we have:

$$\mathrm{w}(x, y, \omega) = \mathrm{w}_0(\omega) \sqrt{1 + \left(\frac{z}{z_R(\omega)} \right)^2} \tag{5.8}$$

being

$$z = r \cos\theta \tag{5.9}$$

$$\rho = r \sin\theta \tag{5.10}$$

$$\theta = \text{arc cos} \left(\frac{\mathbf{s} \cdot \mathbf{r}}{|r|} \right) \tag{5.11}$$

$$z_R(\omega) = \frac{\omega \mathrm{w}_0^2}{2c} \tag{5.12}$$

The total electric field in the focus will be the sum of the field for all the frequencies:

$$E(x, y) = \sum_\omega E_\omega \tag{5.13}$$

And thus the intensity of the focus will be:

$$I(x, y) \propto |E(x, y)|^2 \tag{5.14}$$

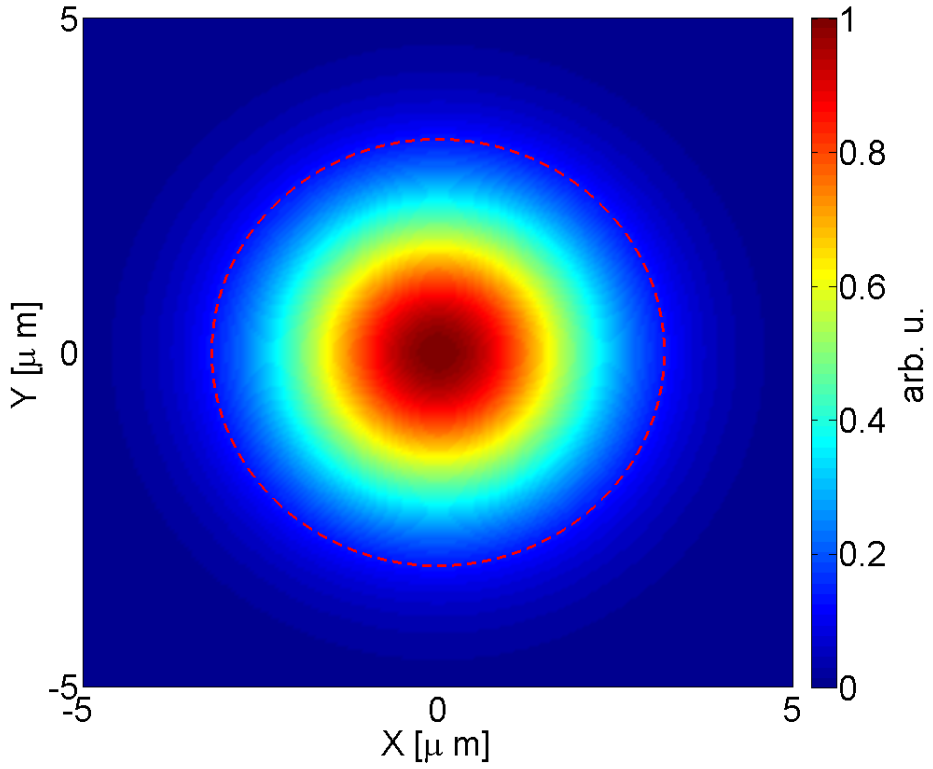

Figure 5.9: Focus produced by the proposed compressor. The waist, marked in red, is 3.8 μm, as it was expected.

Fig. 5.9 shows the focus for a compressor with 28.7° of angle of incidence with gratings of 1480 lines/mm. The initial beam has a waist of 20 cm and a Fourier limit of 30 fs. The distance between gratings is set to introduce a GDD of 3.79×10^6 fs^2 to compress the pulse from 350 ps to its Fourier limit. The focalization system is a 15° off-axis parabola with 2.5 m of effective focal length. The waist of the focus according the simulation is 3.8 μm, matching with the theoretical waist that would be obtained with a conventional compressor.

In conclusion, a single pass compressor allows to reduce the size of the beam, offers the same focalization capabilities of a double pass compressor and allows more efficiency since can work near the Littrow of the gratings and has only two diffractions in them. In addition, since the laser is not temporally compressed at the exit of the second grating, the fluence in the gratings is lower, avoiding the risk of damaging these components. Also the beam could be transported in air, reducing the cost of the system.

Conclusions

In this thesis, we have developed a laser driven X-ray source based in the ionization of a target when a ultraintense laser is focalized in it and in the consequent acceleration and deceleration of electrons and creation of inner vacants in the atoms of the target. With the aim of improving the conventional sources, we have studied a curtain liquid jet at atmospheric pressure as a target for the generation of radiation. We have found that while the efficiency in the K_α production for the 8.0 keV K_α of copper is in the order of 10^{-7}, the efficiency for the 11.9 keV K_α of a KBr dissolved in the liquid jet is in the order of 10^{-8}. Despite of this reduction in the efficiency, liquid targets offer robustness and stability. Besides, since there is no need to replace the target, it is possible to carry out systematic and/or long-live measurements. These characteristics are mandatory if we want to explore the challenging possibilities that laser-based sources of ionizing radiation may offer.

To fully characterize the source, we have built a Time of Flight detector that has allowed us to study the plasma filament dynamics. This is quite important in our source, since the interaction of a filamenting femtosecond laser beam with a target in air is a very difficult theoretical problem and asks for fully understanding of the filament dynamics. In addition, the developed Time of Flight detector could be adapted to behave as a Streak Camera which can measure the duration of the X-ray pulse.

Once the radiation source has been built and characterised, we have explored its possible applications. In particular, we have proved that our source has an important advantage in X-ray fluorescence experiments: while the X-ray radiation provides a complete picture of the substances present in a sample, the accelerated electrons can be used to analyse only the superficial layer. Applied to artworks, this technique allow to distinguish between the the visible painting and the possible images hidden beneath it.

Finally, we have proposed several modification to the laser system itself that could cheapen the total system cost, which is necessary if we want that laser driven sources competes with with the well-established particle accelerator technology.

Future work

Although we have presented a liquid target that offers robustness and stability, several modifications can be explored to improve the efficiency of the source. We have seen that the use of two pulses improved the signal, but maybe different prepulses could lead to a higher efficiency. Also, other liquids or jet geometries can be tested. There is still a lot to work to fully understand the physics happening in the interaction with the target. PICs simulation could clarify some points of the interaction. In this sense, our Time of Flight detector could be use in conjunction with a high voltage switch to obtain snapshots of the dynamics of the plasma filament. Besides, this device has still to be modified to act as an streak camera that allow us to know the time duration of the X-ray pulse.

A laser driven radiation source with extreme flux has promising applications, as we have exposed in this thesis, and thus there is a vast future yet to be explored. Maybe one of the most important applications is their use in radiotherapy. Nowadays, nobody knows the effect of a ultrashort radiation pulses in cells. At the moment, only preliminary studies in some cell line has been performed, and the results are inconclusive. In this sense, we have proposed a collaboration with the Institute of Biomedicine of Sevilla to study the effects of this kind of radiation in the drosophila melanogaster.

To conclude, in this thesis we have built a laser driven radiation source of extreme flux. We have characterised it and we have explored its applications, finding some promising uses. But the accelerator technology is growing fast, and if we want the laser driven sources become someday commercial systems spread in several areas, there is a lot of work yet to be done, both in proving its unique advantages and in cheapening the total product cost.

List of publications

Peer-Reviewed Publications directly resulting from the work presented

- F. Valle Brozas, D. Papp, L. M. Escudero, L. Roso, and A. Peralta Conde. X-ray emission from a liquid curtain jet when irradiated by femtosecond laser pulses. *Applied Physics B*, 123(6):190, 2017
- F. Valle Brozas, A. Crego, L. Roso, and A. Peralta Conde. Laser-based x-ray and electron source for x-ray fluorescence studies. *Applied Physics B*, 122(8):220, 2016
- F. Valle Brozas, C. Salgado, J. I. Apiñaniz, A. V. Carpentier, M. Sánchez Albaneda, L. Roso, C. Raposo, C. Padilla, and A. Peralta Conde. Determination of the species generated in atmospheric-pressure laser-induced plasmas by mass spectrometry techniques. *Laser Physics*, 26(5):055602, 2016
- R. Lera, F. Valle-Brozas, S. Torres-Peiró, A. Ruiz de-la Cruz, M. Galán, P. Bellido, M. Seimetz, J. M. Benlloch, and L. Roso. Simulations of the gain profile and performance of a diode side-pumped qcw nd:yag laser. *Appl. Opt.*, 55(33):9573–9576, Nov 2016
- F. Valle Brozas, A. V. Carpentier, C. Salgado, J. L. Apińaniz, M. Rico, M. Sánchez Albaneda, J. M. Álvarez, A. Peralta Conde, and L.Roso. Fuentes de rayos x mediante láseres intensos: características y aplicaciones. *Rev. Esp. Fis.*, 29:17–21, 2015

Patents

- R. Lera, F. Valle Brozas, L. Roso, and J. M. Benlloch. Optical pulse generator. *Pulsed Lasers Centre (CLPU), Proton Laser Applications S. L., Consejo Superior de Investigaciones Científicas (CSIC), Universidad Politécnica de Valencia, US14243096*, 2014

Bibliography

[1] H. Daido, M. Nishiuchi, and A. S. Pirozhkov. Review of laser-driven ion sources and their applications. *Reports on Progress in Physics*, 75(5):056401, 2012.

[2] A. Macchi, M. Borghesi, and M. Passoni. Ion acceleration by superintense laser-plasma interaction. *Rev. Mod. Phys.*, 85:751–793, May 2013.

[3] A. Giulietti. *Laser-Driven Particle Acceleration Towards Radiobiology and Medicine*. 2016.

[4] P Mayles and J.C Rosenwald Nahum, A. *Handbook of Radiotherapy Physics: Theory and Practice*. 2007.

[5] M. Durante and JS. Loeffler. Charged particles in radiation oncology. *Nat. Rev. Clin. Oncol.*, 7:37–43, 2010.

[6] R. Meesat, H. Belmouaddine, J.F. Allard, C. Tanguay-Renaud, R. Lemay, T. Brastaviceanu, L. Trembla, B. Paquette, J. R. Wagner, J. P. Jay-Gerin, M. Lepage, M. A. Huels, and D. Houde. Cancer radiotherapy based on femtosecond ir laser-beam filamentation yielding ultra-high dose rates and zero entrance dose. *Proc Natl Acad Sci USA*, 109(38):E2508–E2513, 2012.

[7] O. Rigaud, N. O. Fortunel, P. Vaigo, E. Cadio, M. T. Martin, O. Lundh, J. Faure, C. Rechatin, V. Malka, and A. Gaudel. Exploring ultrashort high-energy electron-induced damage in human carcinoma cells. *Cell Death and Disease*, 1:e73, 2010.

[8] C. Tillman, G. Grafström, A.-C. Jonsson, B.-A. Jönsson, I. Mercer, S. Mattsson, S.-E. Strand, and S. Svanberg. Survival of mammalian cells exposed to ultrahigh dose rates from a laser-produced plasma x-ray source. *Radiology*, 213(3):860–865, 1999.

[9] K. Zeil, M. Baumann, E. Beyreuther, T. Burris-Mog, T. E. Cowan, W. Enghardt, L. Karsch, S. D. Kraft, L. Laschinsky, J. Metzkes, D. Naumburger, M. Oppelt, C. Richter, R. Sauerbrey, M. Schürer, U. Schramm, and J. Pawelke. Dose-controlled

irradiation of cancer cells with laser-accelerated proton pulses. *Applied Physics B*, 110(4):437–444, 2013.

[10] S. D. Kraft, C. Richter, K. Zeil, M. Baumann, E. Beyreuther, S. Bock, M. Bussmann, T. E. Cowan, Y. Dammene, W. Enghardt, U. Helbig, L. Karsch, T. Kluge, L. Laschinsky, E. Lessmann, J. Metzkes, D. Naumburger, R. Sauerbrey, M. Schürer, M. Sobiella, J. Woithe, U. Schramm, and J. Pawelke. Dose-dependent biological damage of tumour cells by laser-accelerated proton beams. *New Journal of Physics*, 12(8):085003, 2010.

[11] V. Malka, J. Faure, and Y. A. Gauduel. Ultra-short electron beams based spatio-temporal radiation biology and radiotherapy. *Mutation Research/Reviews in Mutation Research*, 704(1–3):142 – 151, 2010. ESF-EMBO Conference: Spatio-Temporal Radiation Biology: Transdisciplinary Advances for Biomedical Applications.

[12] J. Nguyen, Y. Ma, T. Luo, R. G. Bristow, D. A. Jaffray, and Q. B. Lu. Direct observation of ultrafast-electron-transfer reactions unravels high effectiveness of reductive dna damage. *roc. Natl. Acad. Sci. U. S. A.*, 108(11778), 2011.

[13] X. Kong, S. K. Mohanty, J. Stephens, J. T. Heale, V. Gomez-Godinez, L. Z. Shi, J.-S. Kim, K. Yokomori, and M. W. Berns. Comparative analysis of different laser systems to study cellular responses to dna damage in mammalian cells. *Nucleic Acids Research*, 37(9):e68, 2009.

[14] A. Yogo, T. Maeda, T. Hori, H. Sakaki, K. Ogura, M. Nishiuchi, A. Sagisaka, H. Kiriyama, H. Okada, S. Kanazawa, T. Shimomura, Y. Nakai, M. Tanoue, F. Sasao, P. R. Bolton, M. Murakami, T. Nomura, S. Kawanishi, and K. Kondo. Measurement of relative biological effectiveness of protons in human cancer cells using a laser-driven quasimonoenergetic proton beamline. *Applied Physics Letters*, 98(5):053701, 2011.

[15] D. Strickland and G. Mourou. Compression of amplified chirped optical pulses. *Optics Communications*, 56(3):219 – 221, 1985.

[16] S. Corde, K. Ta Phuoc, G. Lambert, R. Fitour, V. Malka, A. Rousse, A. Beck, and E. Lefebvre. Femtosecond x rays from laser-plasma accelerators. *Rev. Mod. Phys.*, 85:1–48, Jan 2013.

[17] G. D. Tsakiris, K. Eidmann, J. Meyer ter Vehn, and F. Krausz. Route to intense single attosecond pulses. *New Journal of Physics*, 8(1):19, 2006.

[18] T. Baeva, S. Gordienko, and A. Pukhov. Theory of high-order harmonic generation in relativistic laser interaction with overdense plasma. *Phys. Rev. E*, 74:046404, Oct 2006.

[19] F. Valle Brozas, A. V. Carpentier, C. Salgado, J. L. Apińaniz, M. Rico, M. Sánchez Albaneda, J. M. Álvarez, A. Peralta Conde, and L.Roso. Fuentes de rayos x mediante láseres intensos: características y aplicaciones. *Rev. Esp. Fis.*, 29:17–21, 2015.

[20] F. Valle Brozas, A. Crego, L. Roso, and A. Peralta Conde. Laser-based x-ray and electron source for x-ray fluorescence studies. *Applied Physics B*, 122(8):220, 2016.

[21] Ultrashort laser pulse phenomena. In J. C. Diels and W. Rudolph, editors, *Ultrashort Laser Pulse Phenomena (Second Edition)*. Academic Press, Burlington, second edition edition, 2006.

[22] L. M. Frantz and J. S. Nodvik. Theory of pulse propagation in a laser amplifier. *Journal of Applied Physics*, 34(8):2346–2349, 1963.

[23] L. V. Keldysh. Diagram technique for nonequilibrium processes. *JETP*, 3447(4):1515, 1964.

[24] A. A. Andreev, J. Limpouch, and A. N. Semankhin. Absoprtion of the energy of a short laser pulse obliquely incident of a highly inhomogeneous plasma. *Bull. Russ. Acad. Sci.*, 58:1056–1063, 1994.

[25] D. W. Forslund, J. M. Kindel, and K. Lee. Theory of hot-electron spectra at high laser intensity. *Phys. Rev. Lett.*, 39:284–288, Aug 1977.

[26] S. C. Wilks, W. L. Kruer, M. Tabak, and A. B. Langdon. Absorption of ultra-intense laser pulses. *Phys. Rev. Lett.*, 69:1383–1386, Aug 1992.

[27] M. Lezius, S. Dobosz, D. Normand, and M. Schmidt. Explosion dynamics of rare gas clusters in strong laser fields. *Phys. Rev. Lett.*, 80:261–264, Jan 1998.

[28] S. P. Hatchett, C. G. Brown, T. E. Cowan, E. A. Henry, J. S. Johnson, M. H. Key, J. A. Koch, A. Bruce Langdon, B. F. Lasinski, R. W. Lee, A. J. Mackinnon, D. M. Pennington, M. D. Perry, T. W. Phillips, M. Roth, T. Craig Sangster, M. S. Singh, R. A. Snavely, M. A. Stoyer, S. C. Wilks, and K. Yasuike. Electron, photon, and ion beams from the relativistic interaction of petawatt laser pulses with solid targets. *Physics of Plasmas*, 7(5):2076–2082, 2000.

[29] S. A. Gaillard, T. Kluge, K. A. Flippo, M. Bussmann, B. Gall, T. Lockard, M. Geissel, D. T. Offermann, M. Schollmeier, Y. Sentoku, and T. E. Cowan. Increased laser-accelerated proton energies via direct laser-light-pressure acceleration of electrons in microcone targets. *Physics of Plasmas*, 18(5):056710, 2011.

[30] S. M. Pfotenhauer, O. Jäckel, A. Sachtleben, J. Polz, W. Ziegler, H.-P. Schlenvoigt, K.-U. Amthor, M. C. Kaluza, K. W. D. Ledingham, R. Sauerbrey, P. Gibbon, A. P. L. Robinson, and H. Schwoerer. Spectral shaping of laser generated proton beams. *New Journal of Physics*, 10(3):033034, 2008.

[31] E. d'Humières. Ion acceleration by high intensity short pulse lasers. 2012.

[32] T. Esirkepov, M. Borghesi, S. V. Bulanov, G. Mourou, and T. Tajima. Highly efficient relativistic-ion generation in the laser-piston regime. *Phys. Rev. Lett.*, 92:175003, Apr 2004.

[33] R. Kodama, K. Takahashi, K. A. Tanaka, M. Tsukamoto, H. Hashimoto, Y. Kato, and K. Mima. Study of laser-hole boring into overdense plasmas. *Phys. Rev. Lett.*, 77:4906–4909, Dec 1996.

[34] A. Macchi, S. Veghini, T. V Liseykina, and F. Pegoraro. Radiation pressure acceleration of ultrathin foils. *New Journal of Physics*, 12(4):045013, 2010.

[35] L. YIN, B. J. ALBRIGHT, B. M. HEGELICH, and J. C. FERNáNDEZ. Gev laser ion acceleration from ultrathin targets: The laser break-out afterburner. *Laser and Particle Beams*, 24(2):291–298, 2006.

[36] L. Yin, B. J. Albright, B. M. Hegelich, K. J. Bowers, K. A. Flippo, T. J. T. Kwan, and J. C. Fernández. Monoenergetic and gev ion acceleration from the laser breakout afterburner using ultrathin targets. *Physics of Plasmas*, 14(5):056706, 2007.

[37] P. A. Norreys, A. P. Fews, F. N. Beg, A. R. Bell, A. E. Dangor, P. Lee, M. B. Nelson, H. Schmidt, M. Tatarakis, and M. D. Cable. Neutron production from picosecond laser irradiation of deuterated targets at intensities of $10^19 w/cm^2$. *Plasma Physics and Controlled Fusion*, 40(2):175, 1998.

[38] C. L. Ellison and J. Fuchs. Optimizing laser-accelerated ion beams for a collimated neutron source. *Physics of Plasmas*, 17(11):113105, 2010.

[39] I. Pomerantz, E. McCary, A. R. Meadows, A. Arefiev, A. C. Bernstein, C. Chester, J. Cortez, M. E. Donovan, G. Dyer, E. W. Gaul, D. Hamilton, D. Kuk, A. C. Lestrade, C. Wang, T. Ditmire, and B. M. Hegelich. Ultrashort pulsed neutron source. *Phys. Rev. Lett.*, 113:184801, Oct 2014.

[40] G. S. Bauer. Physics and technology of spallation neutron sources. *Nuclear Instruments and Methods in Physics Research A*, 463:505–543, May 2001.

[41] W. P. Leemans, B. Nagler, A. J. Gonsalves, Cs. Tóth, K. Nakamura, C. G. R. Geddes, E. Esarey, C. B. Schroeder, and S. M. Hooker. Gev electron beams from a centimetre-scale accelerator. *Nature Physics*, 2, 2006.

[42] L. Gray and J. Read. Treatment of cancer with fast neutrons. *Nature*, 152(53), 1943.

[43] Rowland Ll. Morgan. Fast neutron therapy. *AIP Conference Proceedings*, 9(1):562–577, 1972.

[44] R. Loveman, J. Bendahan, T. Gozani, and J. Stevenson. Time of flight fast neutron radiography. *Nuclear Instruments and Methods in Physics Research B*, 99:765–768, May 1995.

[45] D. P. Higginson, J. M. McNaney, D. C. Swift, T. Bartal, D. S. Hey, R. Kodama, S. Le Pape, A. Mackinnon, D. Mariscal, H. Nakamura, N. Nakanii, K. A. Tanaka, and F. N. Beg. Laser generated neutron source for neutron resonance spectroscopy. *Physics of Plasmas*, 17(10):100701, 2010.

[46] L.J. Perkins, B.G. Logan, M.D. Rosen, M.D. Perry, T. Diaz de la Rubia, N.M. Ghoniem, T. Ditmire, P.T. Springer, and S.C. Wilks. The investigation of high intensity laser driven micro neutron sources for fusion materials research at high fluence. *Nuclear Fusion*, 40(1):1, 2000.

[47] U. Linz and J. Alonso. Laser-driven ion accelerators for tumor therapy revisited. *Phys. Rev. Accel. Beams*, 19:124802, Dec 2016.

[48] F. Fernández and G. Hernández. Comment on fuentes de rayos x mediante láseres intensos: características y aplicaciones. *Rev. Esp. Fis.*, 30, 2016.

[49] S. L. Chin. *Femtosecond Laser Filamentation, Monography.* 2010.

[50] F. M. Khan. *The Physics of Radiation Therapy.* 2003.

[51] C. Fonseca Cuenca. Generación de electrones y rayos x a partir de pulsos láser de gw y alta tasa de repetición, y su protección radiológica. *thesis, University of Salamanca*, 2011.

[52] B. B. Zhang, S. S. Sun, D. R. Sun, and Y. Tao. Note: A novel normalization scheme for laser-based plasma x-ray sources. *Review of Scientific Instruments*, 85(9):096110, 2014.

[53] K.A. Ivanov, D.S. Uryupina, R.V. Volkov, A.P. Shkurinov, I.A. Ozheredov, A.A. Paskhalov, N.V. Eremin, and A.B. Savel'ev. High repetition rate laser-driven k_α x-ray source utilizing melted metal target. *Nuclear Instruments and Methods in Physics Research Section A: Accelerators, Spectrometers, Detectors and Associated Equipment*, 653(1):58 – 61, 2011. Superstrong 2010.

[54] B. Hou, J. Nees, A. Mordovanakis, M. Wilcox, G. Mourou, L.M. Chen, J.-C. Kieffer, C.C. Chamberlain, and A. Krol. Hard x-ray generation from solids driven by relativistic intensity in the lambda-cubed regime. *Applied Physics B*, 83(1):81–85, 2006.

[55] H. Witte, M. Silies, T. Haarlammert, J. Hüve, J. Kutzner, and H. Zacharias. Multi-kilohertz, ultrafast hard x-ray k α source. *Applied Physics B*, 90(1):11–14, 2008.

[56] M. Li, K. Huang, L. Chen, W. Yan, M. Tao, J. Zhao, Y. Ma, Y. Li, and J. Zhang. Laser-driven powerful khz hard x-ray source. *Radiation Physics and Chemistry*, pages – , 2016.

[57] L. Miaja-Avila, G.C. O'Neil, J. Uhling, C. L. Cromer, M. L. Dowell, R. Jimenez, A. S. Hoover, K. L. Silverman, and J. N. Ullom. Laser plasma x-ray source for ultrafast time-resolved x-ray absorption spectroscopy. *Struct Dyn.*, 2(2), 2015.

[58] G. Korn, A. Thoss, H. Stiel, U. Vogt, M. Richardson, T. Elsaesser, and M. Faubel. Ultrashort 1-khz laser plasma hard x-ray source. *Opt. Lett.*, 27(10):866–868, May 2002.

[59] N. Zhavoronkov, Y. Gritsai, G. Korn, and T. Elsaesser. Ultra-short efficient laser-driven hard x-ray source operated at a khz repetition rate. *Applied Physics B*, 79(6):663–667, 2004.

[60] R. J. Tompkins, I. P. Mercer, M. Fettweis, C. J. Barnett, D. R. Klug, Lord G. Porter, I. Clark, S. Jackson, P. Matousek, A. W. Parker, and M. Towrie. 5–20 kev laser-induced x-ray generation at 1 khz from a liquid-jet target. *Review of Scientific Instruments*, 69(9):3113–3117, 1998.

[61] D. Papp, R. Polanek, Z. Lecz, L. Volpe, A. Peralta Conde, and A. A. Andreev. A proposed 100-khz fs laser plasma hard x-ray source at the eli-alps facility. *IEEE Transactions on Plasma Science*, 44(10):2382–2392, Oct 2016.

[62] E. J. Lam, M. N. Álvarez, M. Gálvez, and E. B. Álvarez. A model for calculating the density of aqueous multicomponent electrolyte solutions. *J. Chil. Chem. Soc.*, 53(1), 2008.

[63] X-ray mass attenuation coefficients, https://www.nist.gov/pml/x-ray-mass-attenuation-coefficients.

[64] N. Zhavoronkov, Y. Gritsai, M. Bargheer, M. Woerner, and T. Elsaesser. Generation of ultrashort k_α radiation from quasipoint interaction area of femtosecond pulses with thin foils. *Applied Physics Letters*, 86(24):244107, 2005.

[65] Y. Jiang, T. Lee, and C. G. Rose-Petruck. Generation of ultrashort hard-x-ray pulses with tabletop laser systems at a 2-khz repetition rate. *J. Opt. Soc. Am. B*, 20(1):229–237, Jan 2003.

[66] T. Guo, C. Rose-Petruck, R. Jimenez, F. Raksi, J. A. Squier, B. C. Walker, K. R. Wilson, and C. P. J. CBarty. *Proc. SPIE*, (84):3157, 1997.

[67] Y. Jiang, T. Lee, W. Li, G. Ketwaroo, and C. G. Rose-Petruck. High-average-power 2-khz laser for generation of ultrashort x-ray pulses. *Opt. Lett.*, 27(11):963–965, Jun 2002.

[68] F. Brunel. *Phys. Rev. Lett.*, 59(52), 1987.

[69] J. F. Pelletier, M. Chaker, and J. C. Kieffer. Soft x-ray emission produced by a sub-picosecond laser in a single- and double-pulse scheme. *Journal of Applied Physics*, 81(9):5980–5983, 1997.

[70] R. Lokasani, G. Arai, Y. Kondo, H. Hara, T.-H. Dinh, T. Ejima, T. Hatano, W. Jiang, T. Makimura, B. Li, P. Dunne, G. O'Sullivan, T. Higashiguchi, and J. Limpouch. Soft x-ray emission from molybdenum plasmas generated by dual laser pulses. *Applied Physics Letters*, 109(19):194103, 2016.

[71] R. Fazeli and M. H. Mahdieh. Comparison of line x-ray emission from solid and porous nano-layer coated targets irradiated by double laser pulses. *Physics of Plasmas*, 22(11):113303, 2015.

[72] A. A. Andreev, J. Limpouch, A. B. Iskakov, and H. Nakano. Enhancement of x-ray line emission from plasmas produced by short high-intensity laser double pulses. *Phys. Rev. E*, 65:026403, Jan 2002.

[73] K. Hatanaka, H. Ono, and H. Fukumura. X-ray pulse emission from cesium chloride aqueous solutions when irradiated by double-pulsed femtosecond laser pulses. *Applied Physics Letters*, 93(6):064103, 2008.

[74] P. F. Zhu, Z. C. Zhang, L. Chen, R. Z. Li, J. J. Li, X. Wang, J. M. Cao, Z. M. Sheng, and J. Zhang. Ultrashort electron pulses as a four-dimensional diagnosis of plasma dynamics. *Review of Scientific Instruments*, 81(10):103505, 2010.

[75] U. Teubner, G. Kühnle, and F. P. Schäfer. Detailed study of the effect of a short prepulse on soft x-ray spectra generated by a high-intensity krf* laser pulse. *Applied Physics B*, 54(6):493–499, 1992.

[76] J. R. Freeman, S. S. Harilal, and A. Hassanein. Enhancements of extreme ultraviolet emission using prepulsed sn laser-produced plasmas for advanced lithography applications. *Journal of Applied Physics*, 110(8):083303, 2011.

[77] S. Fujioka, M. Shimomura, Y. Shimada, S. Maeda, H. Sakaguchi, Y. Nakai, T. Aota, H. Nishimura, N. Ozaki, A. Sunahara, K. Nishihara, N. Miyanaga, Y. Izawa, and K. Mima. Pure-tin microdroplets irradiated with double laser pulses for efficient and minimum-mass extreme-ultraviolet light source production. *Applied Physics Letters*, 92(24):241502, 2008.

[78] M. Yoshida, Y. Fujimoto, Y. Hironaka, K. G. Nakamura, K. Kondo, M. Ohtani, and H. Tsunemi. Generation of picosecond hard x rays by tera watt laser focusing on a copper target. *Applied Physics Letters*, 73(17):2393–2395, 1998.

[79] Hamamatsu x-ray streak cameras, http://www.hamamatsu.com/us/en/product/category/5001/5011/5042/index.html.

[80] P. R. Bolton, M. Borghesi, C. Brenner, D. C. Carrol, C. De Martinis, F. Fiorini, A. Flacco, V. Floquet, J. Fuchs, P. Gallegos, D. Giove, J. S. Green, S. Green, B. Jones, D. Kirby, P. McKenna, D. Neely, F. Nuesslin, R. Prasad, S. Reinhardt, M. Roth, U. Schramm, G. G. Scott, S. Ter-Avetisyan, M. Tolley, G. Turchetti, and J. J. Wilkens. Instrumentation for diagnostics and control of laser-accelerated proton (ion) beams. *Physica Medica: European Journal of Medical Physics*, 30:255–270.

[81] A. Couairon and A. Mysyrowicz. Femtosecond filamentation in transparent media. *Physics Reports*, 441(2–4):47 – 189, 2007.

[82] J. Kasparian and J. Wolf. Physics and applications of atmospheric nonlinear optics and filamentation. *Opt. Express*, 16(1):466–493, Jan 2008.

[83] S. L. Chin, T. J. Wang, C. Marceau, J. Wu, J. S. Liu, O. Kosareva, N. Panov, Y. P. Chen, J. F. Daigle, S. Yuan, A. Azarm, W. W. Liu, T. Seideman, H. P. Zeng, M. Richardson, R. Li, and Z. Z. Xu. Advances in intense femtosecond laser filamentation in air. *Laser Physics*, 22(1):1–53, 2012.

[84] A. Couairon, E. Gaižauskas, D. Faccio, A. Dubietis, and P. Di Trapani. Nonlinear x-wave formation by femtosecond filamentation in kerr media. *Phys. Rev. E*, 73:016608, Jan 2006.

[85] A. A. Ionin, L. V. Seleznev, and E. S. Sunchugasheva. Formation of plasma channels in air under filamentation of focused ultrashort laser pulses. *Laser Physics*, 25(3):033001, 2015.

[86] J. Kasparian, R. Ackermann, Y.-B. André, G. Méchain, G. Méjean, B. Prade, P. Rohwetter, E. Salmon, K. Stelmaszczyk, J. Yu, A. Mysyrowicz, R. Sauerbrey, L. Woeste, and J.-P. Wolf. Progress towards lightning control using lasers. *Journal of the European Optical Society - Rapid publications*, 3(0), 2008.

[87] S. L. Chin, S. A. Hosseini, W. Liu, Q. Luo, F. Théberge, N. Aközbek, A. Becker, V. P. Kandidov, O. G. Kosareva, and H. Schroeder. The propagation of powerful femtosecond laser pulses in opticalmedia: physics, applications, and new challenges. *Canadian Journal of Physics*, 83(9):863–905, 2005.

[88] J. Kasparian, R. Ackermann, Y. André, G. Méchain, G. Méjean, B. Prade, P. Rohwetter, E. Salmon, K. Stelmaszczyk, J. Yu, A. Mysyrowicz, R. Sauerbrey, L. Wöste, and J.-P. Wolf. Electric events synchronized with laser filaments in thunderclouds. *Opt. Express*, 16(8):5757–5763, Apr 2008.

[89] S.L. Chin and K. Miyazaki. A comment on lightning control using a femtosecond laser. *Japanese Journal of Applied Physics*, 38(4R):2011, 1999.

[90] J. Kasparian, L. Woeste, and J. P. Wolf. *OPN Opti. Photon. News*, 21(22 July/Aug.), 2010.

[91] P. Rohwetter, Kasparian, K. Stelmaszczyk, Z. Hao, S. Henin, N. Lascoux, W. M. Nakaema, Y. Petit, M. Queiér, R. Salamé, E. Salmon, L. Woestel, and J. P. Wolf. *Nature Photon.*, 4(451), 2010.

[92] M. Chateauneuf, S. Payeur, J. Dubois, and J.-C. Kieffer. Microwave guiding in air by a cylindrical filament array waveguide. *Applied Physics Letters*, 92(9), 2008.

[93] A. E. Dormidonov, V. V. Valuev, V. L. Dmitriev, S. A. Shlenov, and V. P. Kandidov. Laser filament induced microwave waveguide in air. *Proc. SPIE*, 6733:67332S–67332S–6, 2007.

[94] S. L. Chin, H. L. Xu, Q. Luo, F. Théberge, W. Liu, J. F. Daigle, Y. Kamali, P. T. Simard, J. Bernhardt, S. A. Hosseini, M. Sharifi, G. Méjean, A. Azarm, C. Marceau,

O. Kosareva, V. P. Kandidov, N. Aközbek, A. Becker, G. Roy, P. Mathieu, J. R. Simard, M. Châteauneuf, and J. Dubois. Filamentation "remote" sensing of chemical and biological agents/pollutants using only one femtosecond laser source. *Applied Physics B*, 95(1):1–12, 2009.

[95] P. W. Milonni. Lidar. range-resolved optical remote sensing of the atmosphere, in the springer series in optical sciences, vol. 102, edited by claus weitkamp. *Contemporary Physics*, 50(5):601–602, 2009.

[96] M. Plewicki and R. Levis. Femtosecond stimulated raman spectroscopy of methanol and acetone in a noncollinear geometry using a supercontinuum probe. *J. Opt. Soc. Am. B*, 25(10):1714–1719, Oct 2008.

[97] J. H. Odhner, D. A. Romanov, and R. J. Levis. Rovibrational wave-packet dispersion during femtosecond laser filamentation in air. *Phys. Rev. Lett.*, 103:075005, Aug 2009.

[98] A. Talebpour, M. Abdel-Fattah, A. D. Bandrauk, and S. L. Chin. *Laser Phys.*, 11:68–76, 2001.

[99] J. Ju, H. Sun, A. Sridharan, T.-J. Wang, C. Wang, J. Liu, Z. Li, R.and Xu, and S. L. Chin. Laser-filament-induced snow formation in a subsaturated zone in a cloud chamber: Experimental and theoretical study. *Phys. Rev. E*, 88:062803, Dec 2013.

[100] C. K. Birdsall and B. Langdon. *McGraw-Hill, New York*, 1985.

[101] Z. Sun, J. Chen, and W. Rudolph. Determination of the transient electron temperature in a femtosecond-laser-induced air plasma filament. *Phys. Rev. E*, 83:046408, Apr 2011.

[102] Uladzimir Shymanovich. *Direct observation of ultrafast atomic motion using time-resolved X-ray diffraction.* PhD thesis, 2007.

[103] P. Kirkpatrick and A. V. Baez. Formation of optical images by x-rays. *J. Opt. Soc. Am.*, 38(9):766–774, Sep 1948.

[104] *Handheld XRF for Art and Archaeology. Studies and Archeological.* 2013.

[105] *Handbook of practical fluorescence analysis, XXIV.* 2006.

[106] *Handbook of X-Ray Spectrometry, Second Edition.* 2001.

[107] National institute of standards and technology. estar stopping power and range tables for electrons, http://physics.nist.gov/physrefdata/star/text/estar.html.

[108] http://www.webexhibits.org/pigments/.

[109] National institute of standards and technology x-ray transition energies database, http://physics.nist.gov/physrefdata/xraytrans/html/search.html.

[110] Pigments through the ages, institute for dynamic educational advancement, http://www.webexhibits.org/pigments/.

[111] R. Toth, J. C. Kieffer, S. Fourmaux, T. Ozaki, and A. Krol. In-line phase-contrast imaging with a laser-based hard x-ray source. *Review of Scientific Instruments*, 76(8):083701, 2005.

[112] W. H. T. Vlemmings. A review of maser polarization and magnetic fields. *Astrophysical Masers and their Environments Proceedings IAU Symposium*, 242, 2007.

[113] H. Karttunen, P. Kröger, and H. Oja. *Fundamental Astronomy*. 2007.

[114] E. Costa, P. Soffitta, R. Bellazzini, A. Brez, N. Lumb, and G. Spandre. An efficient photoelectric x-ray polarimeter for the study of black holes and neutron stars. *Nature*, 411:662–665, 2001.

[115] F. Muleria, P. Soffitta, R. Bellazzinic, A. Brezc, E. Costa, S. Fabiania, M. Fruttia, M. Minutic, M. Barbara Negrid, P. Pascalea, A. Rubinia, G. Sindonia, and G. Spandrec. A very compact polarizer for an x-ray polarimeter calibration. 6686(668610-1), 2007.

[116] B.L. Henke, E.M. Gullikson, and J.C. Davis. X-ray interactions: Photoabsorption, scattering, transmission, and reflection at e = 50-30,000 ev, z = 1-92. *Atomic Data and Nuclear Data Tables*, 54(2):181 – 342, 1993.

[117] T. E. Schmid, G. Dollinger, W. Beisker, V. Hable, C. Greubel, S. Auer, A. Mittag, . Tarnok, A. A. Friedl, M. Molls, and B. Röper. Differences in the kinetics of γ-h2ax fluorescence decay after exposure to low and high let radiation. *International Journal of Radiation Biology*, 86(8):682–691, 2010.

[118] A. Asaithamby, N. Uematsu, A. Chatterjee, M. D. Story, S. Burma, and D. J. Chen. Repair of hze-particle-induced dna double-strand breaks in normal human fibroblasts. *Radiation Research*, 169(4):437–446, 2008.

[119] P. A. Jeggo and M. Lobrich. Artemis links atm to double strand break rejoining. *Cell Cycle*, 4(3):359–362, 2005. PMID: 15684609.

[120] B. Jakob, J. Splinter, S. Conrad, K. O. Voss, D. Zink, M. Durante, M. Löbrich, and G. Taucher-Scholz. Dna double-strand breaks in heterochromatin elicit fast repair protein recruitment, histone h2ax phosphorylation and relocation to euchromatin. *Nucleic Acids Research*, 39(15):6489, 2011.

[121] P. Reynolds, J. A. Anderson, J. V. Harper, M. A. Hill, S. W. Botchway, A. W. Parker, and P. O'Neill. The dynamics of ku70/80 and dna-pkcs at dsbs induced by ionizing radiation is dependent on the complexity of damage. *Nucleic Acids Research*, 40(21):10821, 2012.

[122] T. Helleda, E. Petermann, C. Lundin, B. Hodgson, and R. A. Sharma. Dna repair pathways as targets for cancer therapy. *Nat. Rev. Cancer*, 8:193, 2008.

[123] M. E. Lomax, L. K. Fokes, and P. O'Neil. Biological consequences of radiation-induced dna damage: Relevance to radiotherapy. *Clin. Oncol.*, 25:578–585, 2013.

[124] F. M. Khan. *The Basic Science of Oncology*. 1992.

[125] D. Caldwell. *Int. J. Quantum Chem.*, 9(755), 1975.

[126] K. M. Prise. New advances in radiation biology. *Occupational Medicine*, 56(3):156, 2006.

[127] U. Amaldi and G. Kraft. Radiotherapy with beams of carbon ions. *Reports on Progress in Physics*, 68(8):1861, 2005.

[128] A. Alejo. Development of laser based devices for intraoperative radiation therapy. *Master Thesis, University of Salamanca*, 2013.

[129] J. M. Álvarez, J. Lozano, F. Valle Brozas, O. Varela, E. García, and L. Roso. Response of epds to the radiation field generated form laser-solid interaction at high repetition rate. *18th Interantional Conference on Solid State Dosimetry, poster contribution*, 2016.

[130] F. Bachmann, P. Loosen, and R. Poprawe. *High Power Diode Lasers: Technology and Applications*. 2007.

[131] V. Sturm, H. G. Treusch, and P. Loosen. Cylindrical microlenses for collimating high-power diode lasers. *Proc. SPIE*, 3097:717–726, 1997.

[132] W. Koechner. *Solid-State Laser Engineering*. 2006.

[133] J. Arasa and J. Alda. Real ray tracing. *Mark Dekker*, 2004.

[134] D. N. Vitek, E. Block, Y. Bellouard, D. E. Adams, S. Backus, D. Kleinfeld, C. G. Durfee, and J. A. Squier. Spatio-temporally focused femtosecond laser pulses for nonreciprocal writing in optically transparent materials. *Opt. Express*, 18(24):24673–24678, Nov 2010.

[135] Guanghao Zhu, James van Howe, Michael Durst, Warren Zipfel, and Chris Xu. Simultaneous spatial and temporal focusing of femtosecond pulses. *Opt. Express*, 13(6):2153–2159, Mar 2005.

[136] F. Valle Brozas, D. Papp, L. M. Escudero, L. Roso, and A. Peralta Conde. X-ray emission from a liquid curtain jet when irradiated by femtosecond laser pulses. *Applied Physics B*, 123(6):190, 2017.

[137] F. Valle Brozas, C. Salgado, J. I. Apiñaniz, A. V. Carpentier, M. Sánchez Albaneda, L. Roso, C. Raposo, C. Padilla, and A. Peralta Conde. Determination of the species generated in atmospheric-pressure laser-induced plasmas by mass spectrometry techniques. *Laser Physics*, 26(5):055602, 2016.

[138] R. Lera, F. Valle-Brozas, S. Torres-Peiró, A. Ruiz de-la Cruz, M. Galán, P. Bellido, M. Seimetz, J. M. Benlloch, and L. Roso. Simulations of the gain profile and performance of a diode side-pumped qcw nd:yag laser. *Appl. Opt.*, 55(33):9573–9576, Nov 2016.

[139] R. Lera, F. Valle Brozas, L. Roso, and J. M. Benlloch. Optical pulse generator. *Pulsed Lasers Centre (CLPU), Proton Laser Applications S. L., Consejo Superior de Investigaciones Científicas (CSIC), Universidad Politécnica de Valencia, US14243096*, 2014.